THE UNIVERSITY *of* LIVERPOOL

Advances of Mathematical Morphology and Its Applications in Signal Processing

Thesis submitted in accordance with the
requirements of the University of Liverpool
for the degree of Doctor of Philosophy

in

Electrical Engineering and Electronics

by

Jinfei Zhang, BEng.

May, 2007

Advances of Mathematical Morphology and Its Applications in Signal Processing

by

Jinfei Zhang

To my parents, my wife and my son

Acknowledgements

First and foremost, I would like to thank my supervisor, Prof. Q.H. Wu, not only for his invaluable support, stimulating discussions and intellectual guidance, but also for providing such a great opportunity to enrich me on both academic and personal level. For this research project, he has made a great deal of contributions, of which I am truly appreciation.

I am deeply grateful to Dr. Dongjiang Zhang, Dr. Pu Sun and Miss Tianyao Ji for the cooperations, many helpful discussions and much valuable advice along the way.

I would like to show my deepest appreciation to the University of Liverpool for financial support throughout this research project. Thanks is also offered to the Department of Electrical Engineering and Electronics, for providing the research facilities that make it possible for me to conduct this research.

Finally, there is no way to express my respect and gratitude to my parents, for their encouragement, guidance and love, and to my wife, Lili Lin, for her patience, understanding and support during the whole period of my postgraduate life. I am really indebted to my son Jingxiu Zhang, a lovely boy, who is our best resource of happiness and inspiration. I only regret that I have not spent more time with him.

Abstract

This thesis describes some advances of Mathematical Morphology (MM), in order to improve the performance of MM filters in 1-D signal processing, especially in the application to power system protection.

MM methodologies are founded on set-theoretic concepts and nonlinear superpositions of signals and images. The morphological operations possess outstanding geometrical properties which make it undoubted that they are efficient image processing methods. However in 1-D signal processing, MM filters are not widely employed. To explore the applications of MM for 1-D signal processing, our contributions in this area can be summarized in the following two aspects.

Firstly, the framework of the traditional signal processing methods is based on the frequency domain representation of the signal and the analysis of the operators' transfer function in the frequency domain. But to the morphological operations, their representations in the frequency domain are uncertain. In order to tackle this problem, this thesis presents our attempt to describe the weighted morphological dilation in the frequency domain. Under certain restrictions to the signal and the structuring element, weighted dilation is transformed to a mathematical expression in the frequency domain.

Secondly, although the frequency domain analysis plays an important role in signal processing, the geometrical properties of a signal such as the shape of the signal cannot be ignored. MM is an effective method in dealing with such problems. In this thesis, based on the theory of Morphological Wavelet (MW), three multi-resolution signal decomposition schemes are presented. They are Multi-resolution Morphological Top-Hat scheme (MMTH), Multi-resolution Morpho-

logical Gradient scheme (MMG) and Multi-resolution Noise Tolerant Morphological Gradient scheme (MNTMG).

The MMTH scheme shows its significant effect in distinguishing symmetrical features from asymmetrical features on the waveform, which owes to its signal analysis operator: morphological Top-Hat transformation, an effective morphological technique. In this thesis, the MMTH scheme is employed in the identification of transformer magnetizing inrush current from internal fault. Decomposing the signal by MMTH, the asymmetrical features of the inrush waveform are exposed, and the other irrelevant components are attenuated.

The MMG scheme adopts morphological gradient, a commonly used operator for edge detection in image and signal processing, as its signal analysis operator. The MMG scheme bears significant property in characterizing and recognizing the sudden changes with sharp peaks and valleys on the waveform. Furthermore, to the MMG scheme, by decomposing the signal into different levels, the higher the level is processed, the more details of the sudden changes are revealed. In this thesis, the MMG scheme is applied for the design of fault locator of power transmission lines, by extracting the transient features directly from fault-generated transient signals.

The MNTMG decomposition scheme can effectively reduce the noise and extract transient features at the same time. In this thesis, the MNTMG scheme is applied to extract the fault generated transient wavefronts from noise imposed signals in the application of fault location of power transmission lines.

The proposed contributions focus on the effect of weighted dilation in the frequency domain, constructions of morphological multi-resolution decomposition schemes and their applications in power systems.

Contents

List of Figures

List of Tables

List of symbols and abbreviations

Mathematical Morphology

MM	mathematical morphology
DFT	Discrete Fourier transform
GS	grey-scale
GSMF	grey-scale morphological filter
n-D	n dimensional, $n = 1, 2, \ldots$
$\mathbb{E}^d$	d dimensional Euclidean space
id	identity operator
SE	structuring element
ED	Erosion-Dilation filter
MG	Morphological gradient
TH	Top-Hat
WM	Weighted morphology
WMO	Weighted morphological operator
WER	Weighted erosion
WDI	Weighted dilation
WMF	Weighted morphological filter
MP	Morphological pyramid
MW	morphological wavelet
MMTH	Multi-resolution morphological Top-Hat scheme
MMG	Multi-resolution morphological gradient
MNTMG	Multi-resolution noise tolerant morphological gradient

BSE	Base structuring element
MMGLP	Combination of low-pass filter and MMG
$\varnothing$	empty set
$A \oplus B$	dilation of A by B
$A \ominus B$	erosion of A by B
$A \circ B$	opening of A by B
$A \bullet B$	closing of A by B
$\delta_A(X)$	dilation by SE A
$\varepsilon_A(X)$	erosion by SE A
$\gamma_A(X)$	opening by SE A
$\varphi_A(X)$	closing by SE A
$\rho_A(X)$	morphological gradient by SE A
$f \odot_{m,k} g$	ED filter of f and g
$\forall$	for all
$a \ll b$	value a much less than value b
$\bigvee$	supremum
$\bigwedge$	infimum
$\cup$	union
$\cap$	intersection

Transformer inrush current detection

EHV	extra high voltage
SVC	Side Voltage Control
CT	current transformer
EMTDC/PSCAD	power system simulation softwares
LabVIEW	a programming language for control and automation
Matlab	a programming language for scientific research
SNR	signal to noise ratio

Chapter 1

Introduction

1.1 Historical Background of Mathematical Morphology

The word morphology stems from the Greek meaning "study of form" [1], which implies the goal of Mathematical Morphology (MM) is to investigate the geometrical structure of sets. "It is mathematical in the sense that the analysis is based on the set theory, topology, lattice algebra, random functions, etc., and it is called morphology since it aims at analyzing the shape and form of the objects" [2] [3]. The development of MM can be divided into three periods:

1960s and 1970s: Birth and forming the core of the MM operations

Mathematical Morphology was introduced in 1964 by Matheron [4] and Serra [5] [6] at the Paris School of Mines in Fontainebleau, from their research on petrography and mineralogy, including investigation of the relationship between the geometry of porous media and their permeabilities, and quantification of the petrography of iron ores in order to predict their milling properties. During the 1960s and the 1970s, the core of the morphological operations was discovered which includes four basic transformations: erosion, dilation, opening and closing. The dilation was originally proposed by Minkovski in order to characterize integral measures of certain ill-behaved sets, and is sometimes referred to as the "Minkovski set addition" [7]. The erosion, however, was not proposed until much later by Hadwiger [8], and is sometimes referred to as the "Minkovski set subtraction". The opening and closing, formed by compositions of erosion and dilation, were proposed by Matheron [4] [9]. They are called the core of morphological operations because the class of morphological transformations is defined to be the collection of all set transformations generated by unions, compositions, and complementations of erosions and dilations [10], such as morphological gradient and top hat transform which were both developed in this period of time. However the morphological operations in the 1960s and 1970s were all limited to binary erosion and dilation.

1980s: Development and maturation

With the significant development of automated visual inspection, substantial developments in morphology were stimulated in the 1980s. In this period of time, the most important development of MM is the setting of the method (at least of its deterministic aspect) in the mathematical framework of complete lattices [11] . "Although the initial operators were set oriented and translation invariant, they were now transposed to other situations and to other objects such as graphs, numerical or multi-valued functions, where translation might influence the process (geodesy, edge conditions) or even not exist (graphs). Finally, the core of essential axioms could be reduced to the complete lattice structure [12]." The theory of complete lattice provides a more compact theoretical foundation for grey-scale morphological operations.

In the 1980s, the theory of morphological filtering was also presented [6]. Haralick [13] addressed some real-time applications of morphological filtering, and other real-time applications were also presented such as Diff3 [14] and the Delft image processor (DIP) in this period of time [15].

1990s to now: The theoretical frame became more complete and extended the application domain

Following the development in the 1980s, during the decade, MM has been applied in many fields especially its predominant role devoted to video and multimedia analysis, which concerns compression, scene description, image indexing, motion modelling and etc. [16]. The theoretical works on the concept of a connection, in combination with the connected filters and in particular with Meyer's Levelings [17] and Beucher's interplolation techniques [18] have made MM a remarkably powerful tool for segmentation. There were also some researchers devoted to build another transform named slope transform, by which morphological operators are endowed with eigenfunctions and related transfer functions in a slope domain [19] [20]. Furthermore, morphological multi-resolution decomposition scheme [21] also developed rapidly in this period of time, which inherits the multi-dimension and multi-level analysis of the traditional multi-resolution methods, whilst it extends the original methods from the linear domain [22] [23] [24] [25] [26] [27]. A cellular neural network (CNN) based morphological system was also proposed at the end of 1990's [28].

With over three decades of development, MM has become a powerful tool for geometrical shape analysis [29]. With many more researchers starting to devote themselves to its applications in 1-D signal processing [30] [31] [32] [33] [34] [35], MM will demonstrate its outstanding abilities in signal processing as well as its performances in image processing.

1.2 The concepts of Mathematical Morphology

Mathematical Morphology (MM) is a branch of digital signal processing and analysis which uses concepts from algebra (set theory, complete lattices) and geometry (translation, distance, convexity). Appropriate MM operations, as nonlinear transformations, tend to simplify signal data by modifying geometrical features of signal locally, to eliminate irrelevancies while preserving the essential shape characteristics [36] [37].

Mathematical morphology is based on set theory [38]. Sets in MM represent the shapes manifested on binary or grey scale signals/images [13]. The main notion in MM is the interaction between the signal under analysis and a structuring element (SE), where signal and SEs are considered as sets of points and the operations come from set theory [39] [40]. Information pertaining to the size, spatial distribution, shape, connectivity, convexity, smoothness, and orientation can be obtained, by means of applying various SEs to the original object with operations derived from set theory [41].

Like any theory, MM has a perspective which allows it to focus on certain phenomena within signal. It describes signal based on set theory and geometry, thus, distinguishes itself from other signal processing theories, e.g., syntactic theories that are based upon generative grammars and signal processing theories that are based on Fourier analysis. MM provides an algebraic formulation to apply neighbourhood operations on signal or images. The SE, as a probe, slides through the signal/image as a moving window, inspects its interaction with the signal/image, and detects specific features in the neighbourhood of every point of the signal/image [29] [42]. MM operations are predominantly used for the following purposes [43]:

- signal/image pre-processing (noise filtering. shape simplification)
- enhancing object structure (skeletonising, thinning, thickening, convex hull, object marking)
- quantitative description of objects (area, perimeter, projection).

1.3 Comparison between Mathematical Morphology and Linear Signal Processing Methods

The difference between the traditional linear signal processing methods and morphological operations was summarized by Boomgaard [29], which is: "In linear image processing the basic underlying assumption is the superposition of visual stimuli. The visual signal is thought of as the weighted addition of basic signals. This assumption of linearity is questionable in case the image is formed by projection, where one object completely hides another object behind it. Due to using non-linear transformations, it is impossible to reconstruct the original image."

Compared with the traditional non-morphological methods which is based on linear transformations, e.g., convolution and its frequency domain representation, Mathematical Morphology (MM) cares more about the shape of the signal. What the algebra of convolution does for linear systems, the algebra of MM does for shape. Therefore, the algorithm of MM only involves comparisons for finding maxima/minima, or addition/subtraction in some specific case for grey-scale signals/images, and Boolean operations for binary ones which makes it significantly faster in calculation than the multiplication and addition used in convolution for linear transformation.

Table 1.1: Morphological filtering versus convolution

Features	MM	Convolution
Reversibility	No	Yes
Unique algebraic structure	No	Yes
Idempotence and loss of information	Yes	No
Defined in complete lattice	Yes	No
Iteration	Yes	No
Flatness $\psi(\log(f)) = \log(\psi(f))$	Yes	No

On the other hand, the algorithm of MM is not fundamentally different from that of the convolution, which applies addition and subtraction in place of multiplication in the convolution and maxima/minima in place of addition in the convolution. Thus, by analyzing the relationship between these two, morphological operations, a kind of geometrical methods, can be endowed frequency domain analysis and quantitively analytical methods, which will be discussed in this thesis.

Some comparisons between the two approaches are given briefly in Table 1.1 [44].

1.4 Motivations

MM is widely used in the area of image processing and machine vision due to its robustness in preserving the main shape while suppressing the noise. When acting upon complex shapes, morphological operations are able to decompose them into meaningful parts and separate them from the background, as well as preserve the main shape characteristics. Furthermore, the mathematical calculations involved in MM include only addition, subtraction and maximum and minimum operations without any multiplication and division. Although MM bears these advantages, compared with Fourier transform widely applied in the area of both 1-D signal processing and image processing, the morphological operations are seldom applied in 1-D signal processing. Based on our research, there are two reasons.

First, to the traditional methods for signal processing, the time and frequency domains, which are related to each other, are the most common ways of viewing, manipulating and analyzing any signal of interest. So most of these methods are based on convolution and integral transformations such as Fourier transform, Laplacian transform, wavelet analysis, etc.. The frequency response of the operation has been an important characteristic to analyze the efficiency of the operation. In contrast with the traditional methods, the Mathematical Morphology (MM) filtering technique handles a signal in completely different perspective, which describes signal/images based on set theory and geometry [45]. How to build a bridge between the morphological operations and the traditional frequency domain based methods is the interest in our study. In Chapter 3, the effect of weighted morphological dilation in the frequency domain is introduced. Under the particular preconditions, weighted dilation is transform to a mathematical expression in the frequency domain.

Second, when the frequency properties of the signal were emphasized, the geometrical properties of the signal were easily ignored. In modern signal processing, different techniques are applied depending on the type of information carried by the signal. A widespread attitude, adopted by researchers, is empiricism: try something (or even anything), and see what happens [46]. However, the important point is that the analysis technique must be matched by the way in which information is being carried in the signal [47]. In fact, the shape of the signals contains much valuable information which plays important roles in many aspects. Undoubtedly, MM is an effective method to obtain these information. Since the multi-resolution signal decomposition schemes provide convenient and effective ways to process information, several morphological multi-resolution decomposition schemes are proposed based on the theory of Morphological Wavelet (MW), which was presented first by Goutsias and Heijmans [21] [25]. They are Multi-resolution Morphological Top-Hat scheme (MMTH), Multi-resolution Morphological Gradient scheme (MMG) and Multi-resolution Noise Tolerant Morphological Gradient scheme (MNTMG). The applications of them in the power system protection prove that morphological operations can extract the geometrical information implicitly buried in a raw signal and fetch up the insufficiency of the traditional signal processing methods in this aspect.

1.5 Contributions of Research

The major contributions arising from this research can be summarized in the following aspects:

- For the first time, a morphological operator: weighted dilation was endowed a mathematical expression in the frequency domain. The proposed ideas and the deductions builds a bridge between the mathematical morphology and the traditional frequency domain based signal processing methods. It provides a more familiar perspective for traditional signal processing researchers to understand the algorithms of morphological operations.

- Based on the theory of morphological wavelet, three morphological undecimated analogical wavelet decomposition schemes are constructed, which are the Multi-resolution Morphological Top-Hat scheme (MMTH), the Multi-resolution Morphological Gradient scheme (MMG) and the Multi-resolution Noise Tolerant Morphological Gradient scheme (MNTMG). These schemes inherit the multi-dimension and multi-level analysis of wavelet and pyramid, whilst they ignore the time-frequency domain analysis of wavelet and extends the original wavelet and pyramid from the linear domain to the nonlinear domain.

- Apply the MMTH scheme to the power system protection relays [33] [48]. It is focused on the identification of transformer inrush current. The proposed technique is fundamentally different from conventional methods, as it decomposes the signal based on time domain features instead of in the frequency domain. Since it works directly upon the geometric characteristics of the input, there is no need for abstract transform techniques such as Fourier, Laplace, and Hilbert transforms, nor is there a requirement for transform-world concepts such as frequency, convolution, effective bandwidth and ripple. The results obtained confirm that the proposed method provides reliable identification of inrush, in both cases when the current transformer is saturated or there are only low levels of the second harmonic content [33].

- Apply the MMG scheme for design of an ultra-high-speed directional protection relay [34], [49], [50]. The simulation results show that the

MMG scheme is capable of accurately extracting the transient features of fault voltage and current, as a promising means for ultra-high-speed protection relaying. By using the quadratic MMG, the relaying signals are able to provide correct directional response to a transmission line fault under different fault types, positions, path resistances and inception angles.

- Apply the MNTMG scheme to detect fault locations with noise disturbance for transmission line systems. The MNTMG decomposition scheme is constructed in order to improve the MMG scheme to be noise tolerant. It is shown that although the performance of MMG is satisfactory under various fault conditions, it will inevitably deteriorate when various noises are imposed on the transient current signal. The results show that the MNTMG decomposition scheme can effectively reduce the noise and extract transient features.

1.6 Publications

- P. Sun, **J. F. Zhang**, D. J. Zhang, and Q. H. Wu, "Morphological identification of transformer magnetising inrush current", *IEE Electronics Letters*, vol. 38, pp. 437-438, 2002 [33].
- Q. H. Wu, P. Sun, D. J. Zhang, and **J. F. Zhang**, "Identification of transformer inrush current using morphological signal decomposition", *Automation of Electric Power Systems*, pp. 67-78, 2002 [48].
- D. J. Zhang, Q. H. Wu, **J. F. Zhang**, and K. I. Nuttall, "Accurate fault location based on transients extraction using mathematical morphology", *Electronics Letters*, vol. 38, no. 24, pp. 1583-1585, 2002 [49].
- D. J. Zhang, Q. Li, **J. F. Zhang**, Q. H. Wu, and D. R. Turner, "Improving the accuracy of single-ended transient fault locators using mathematical morphology", *IEEE/CSEE International Conference on Power*

System Technology, Kunming, China, October 13-17 2002, vol. 2, pp. 788-792 [50].

- Q. H. Wu, **J. F. Zhang**, and D. J. Zhang, "Ultra-high-speed directional protection of transmission lines using mathematical morphology", *IEEE Transactions on Power Delivery*, vol. 18, no. 4, pp. 1127-1133, 2003 [34].
- **J. F. Zhang**, J. S. Smith, and Q. H. Wu, "Morphological undercimated wavelet decomposition for fault location on power transmission lines", *IEEE Transactions on Circuits and Systems I: Regular Paper*, vol. 53, pp. 1395-1402, 2006 [35].

1.7 Outline of This Thesis

This thesis is structured as follows:

Chapter 2 This chapter introduces the theoretical background of MM. It starts with a review of a number of basic morphological operators such as dilation, erosion, opening and closing, and a brief discussion about the importance of the origin of the structuring element. The theory of grey-scale morphological operators is also covered.

Chapter 3 This chapter firstly introduces the theory of ED filter and that of the weighted morphological filter. Then under the two preconditions, a mathematical relationship is built between weighted dilation of $f(n)$, $g(m)$ and the convolution of them. Finally, weighted dilation is transformed to a mathematical expression in the frequency domain..

Chapter 4 This chapter introduces three morphological undecimated analogical wavelet decomposition schemes. They are the Multi-resolution Morphological Top-Hat scheme (MMTH), the Multi-resolution Morphological Gradient scheme (MMG) and the Multi-resolution Noise Tolerant Morphological Gradient scheme (MNTMG) which are based on the theory of morphological wavelet. These schemes inherit the multi-dimension and multi-level analysis of wavelet and pyramid, whilst it ignores the time-frequency domain analysis of wavelet and extends the original wavelet and pyramid from the linear domain which is based on convolution and the time-frequency domain transformation to the nonlinear domain. The characteristics of these schemes are analyzed respectively in this chapter.

Chapter 5 This chapter presents the application of the MMTH in designing power transformer protection relay. A brief introduction to the inrush current is given first, followed by the descriptions of existing detection methods and the difficulties associated with them. The proposed MMTH technique is then applied to extract the singularity associated with the asymmetric inrush waveform, while attenuating other irrelevant features, which is to discriminate the inrush current from internal fault conditions. By quantifying the extracted features, the inrush current is then identified with simple criteria. The results of applying the MMTH approach to simulated signals and waveforms recorded from physical transformers are given, which indicate that the proposed algorithm is fast and reliable, and may be considered as an alternative method in designing and implementing a digital relay.

Chapter 6 This chapter presents the application of the MMG filtering technique in developing ultra-high-speed directional transmission line protection scheme. Firstly, a process of deriving the direction discriminants of a fault taking place on transmission lines as well as a fast scheme of fault phase selection, is analyzed and some details are discussed theoretically. Then by applying the MMG filtering technique to extract the features directly from fault-generated transient signals, the proposed ultra-high-speed directional protection scheme is verified by a 400kV transmission line model under various fault scenarios.

Chapter 7 This chapter presents the application of MMG scheme and MNTMG scheme in the transmission line protection. The proposed MNTMG scheme is used to extract transient features from noise imposed fault-generated voltage and current wave signals in transmission line protection. The efficiency of the MNTMG scheme used for noise reduction is evaluated in simulation studies. The performance of the fault location is improved.

Chapter 8 This chapter concludes this thesis and discusses the limitation of the proposed morphological techniques. Suggestions for possible future work are also given.

Chapter 2

An Introduction to Mathematical Morphology

2.1 Introduction

This chapter focuses on the definitions of the morphological operators which will be used in later chapters. The definitions for a series of morphological operators including dilation, erosion, opening, closing, morphological gradient and Top-Hat are introduced in this chapter. The effect of the reflection of SE in dilation to the morphological operators especially to opening and closing is also analyzed. It is found that in the application, the reflection of SE is absolutely necessary.

2.2 Notions of complete lattice

Mathematical morphology is the application of the lattice theory to the spatial structures [51]. In lattice theory a basic relation is partial order relation which is denoted as $\leq$. This relation is assumed to have certain properties, the most basic of which leads to the following concept of a "*partly ordered set*" or "*poset*". A poset is a set in which a binary relation $x \leq y$ is defined, which satisfies for all x, y, z the following conditions [51] [52]:

1. Reflexive: for all x, $x \leq x$;
2. Antisymmetry: if $x \leq y$ and $y \leq x$, then $x = y$;
3. Transitivity: $x \leq y$ and $y \leq z$, then $x \leq z$.

A lattice $\mathcal{T}$ is a poset $\mathcal{P}$ if any two elements of it (x and y) have a greatest lower bound (infimum) denoted by $x \vee y$, and a least upper bound (supremum) denoted $x \wedge y$.

A lattice $\mathcal{T}$ is a *complete lattice* when each of its subsets $\mathcal{H}$ has an infimum and a supremum in $\mathcal{T}$. In other words, a complete lattice (either on the Euclidean space $\mathbb{R}^n$ or on digital space $\mathbb{Z}^n$) is a partially ordered set $(\mathcal{T}; \leq)$ in which every subset $\mathcal{H} \subseteq \mathcal{T}$ has a supremum and infimum denoted as $\vee\mathcal{H}$ and $\wedge\mathcal{H}$ respectively [6]. Any finite lattice or lattice of finite length is complete. Not every lattice is complete: thus the rational numbers are not complete, and the real numbers (in their natural order) are not complete unless $\pm\infty$ are adjoined as universal bounds. By definition, every complete lattice $\mathcal{L}$ must possess a least element O and a greatest element I, called universal bounds of $\mathcal{L}$ [11]. For complete lattice there are [53]:

1. Commutativity:

$$X \vee Y = Y \vee X, X \wedge Y = Y \wedge X.$$

2. Associativity:

$$(X \vee Y) \vee Z = X \vee (Y \vee Z), (X \wedge Y) \wedge Z = X \wedge (Y \wedge Z).$$

3. The law of absorption:

$$X \wedge (X \vee Y) = X, X \vee (X \wedge Y) = X.$$

2.3 Functions and Umbra

Before complete lattice is employed to define the morphological operators, the set of grey scale morphological operators are generalized with the help of umbras [52]. The umbra approach is based on the simple observation that the points on and below the graph of a function yield a set to which morphological set operations can be applied [11].

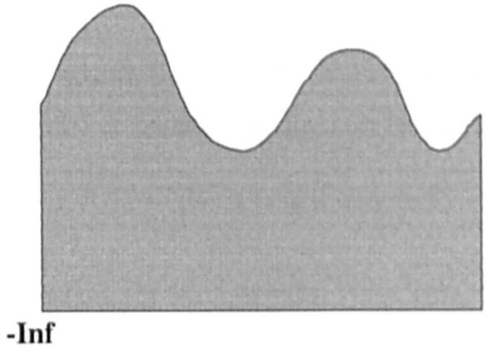

Fig. 2.1: Umbra of $f(x)$

The umbra of a function $f(x)$ is the set of points below the surface represented by $f(x)$, which can be represented as:

$$U(f) = \{(x, a) : a \leq f(x)\}. \tag{2.3.1}$$

In Fig. 2.1, $f(x)$ is an 1-D function and its umbra is the shaded region. After getting the umbra, the binary morphological operators can be applied. In general, the umbra set extends to $a = -\infty$, the function f can be reconstructed from its umbra as:

$$f(x) = \max\{a : (x, a) \in U(f)\}, \forall x. \tag{2.3.2}$$

2.4 Definitions of Binary Morphological Operations

The structure of a Boolean algebra provides the general framework on which the binary morphological operations can be performed. The sets in binary images are members of the 2-D integer space $\mathbb{Z}^2$, where each element of a set is a 2-D vector with (x, y) as coordinates and 0 or 1 as value of each pixel. Let two sets S, $G \subset \mathbb{Z}^2$. Assume S and G represent the binary input set and the binary structuring element respectively. As a structuring element, the size of G is smaller than the size of S. Then:

1. *Translation*: The translation of S by a 2-D vector $x \in \mathbb{Z}^2$ with (x_1, x_2) as coordinates, which is denoted as S_x, can be defined as:

$$S_x = \{s : s = a + x; a \in S\}.$$

2. *Reflection*: The reflection of G around its origin, denoted $\check{G}$, is defined as:

$$\check{G} = \{-g : g \in G\}.$$

Assuming the coordinates of the element g is (g_1, g_2), then the co-ordinates of $-g$ is $(-g_1, -g_2)$.

3. *Complement*: The complement of the set G, denoted G^c, is defined as:

$$G^c = \{x : x \notin G\}.$$

These operations form the basic ingredients of MM.

2.4.1 Binary erosion and dilation

Choose a fixed set $\mathbb{Z}^2$ as Structuring Element (SE). The dilation of S by G, which can also be denoted by δ_G, is defined as:

$$\delta_G = S \oplus G = \{s + g : s \in S, g \in \check{G}\} = \bigcup_{g \in \check{G}} S_g. \qquad (2.4.1)$$

In the definition of dilation (2.4.1), the reflection of G is utilized. In fact, there exists a confusion in the literature about the definitions of binary dilation and erosion [54]. Mohammad has listed some different definitions of the dilation in [54]. Some of them employ the original SE and some of them apply the reflection of SE to define dilation. In our works, the reflection is utilized. The reason will be discussed in section 2.8 in this chapter.

Erosion is the morphological dual to dilation, which can also be denoted by ε_G. It is defined as:

$$\varepsilon_G = S \ominus G = \{x : G_x \subseteq S\} = \bigcap_{g \in G} S_g. \tag{2.4.2}$$

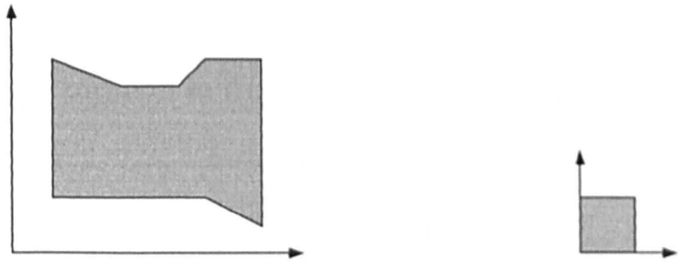

(a) Original image (b) SE

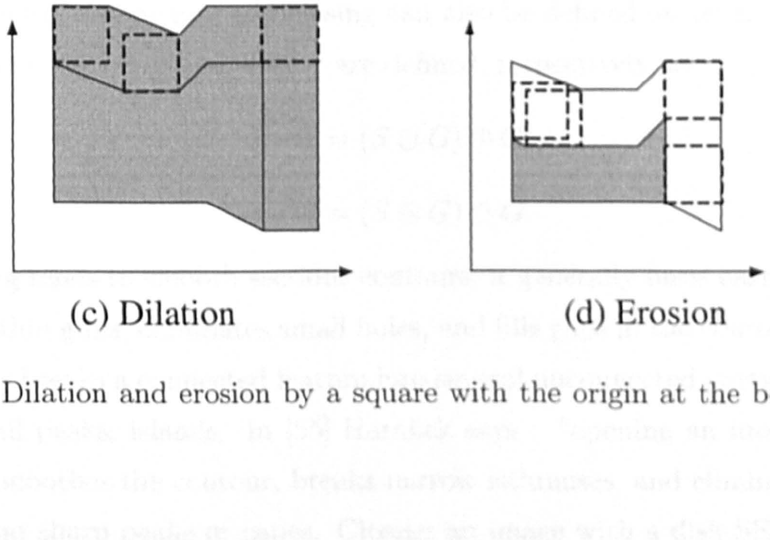

(c) Dilation (d) Erosion

Fig. 2.2: Dilation and erosion by a square with the origin at the bottom-left corner

To visualize the geometrical behavior of both operators, it is helpful to consider 2-D sets depicted in Fig. 2.2. A square SE $G \subset \mathbb{Z}^2$ slides as a probe across the image $S \subset \mathbb{Z}^2$, testing the spatial nature of the image at every point.

Erosion ε and dilation δ with the same structuring element G holds the following relations [11]:

$$\varepsilon\delta\varepsilon = \varepsilon, \tag{2.4.3}$$

$$\delta\varepsilon\delta = \delta. \tag{2.4.4}$$

Other operators in MM, such as opening, closing, skeletons, gradient, etc. are built using the combination of dilations and erosions.

2.4.2 Binary opening and closing

To arbitrary sets S_1 and S_2, S_1, $S_2 \subset \mathbb{Z}^2$, any set transform γ in algebra satisfying the following three conditions is called opening:

1. *Anti extensivity*: $\gamma(S) \subset S$.
2. *Increasing*: $S_1 \subset S_2 \Rightarrow \gamma(S_1) \subset \gamma(S_2)$.
3. *Idempotency*: $\gamma(\gamma(S)) = \gamma(S)$.

Morphological opening and closing can also be defined on terms of erosion and dilation. Opening and closing are defined, respectively, as:

$$S \circ G = (S \ominus G) \oplus G. \tag{2.4.5}$$

$$S \bullet G = (S \oplus G) \ominus G. \tag{2.4.6}$$

Closing tends to smooth sections contours, it generally fuses narrow breaks and long thin gulfs, eliminates small holes, and fills gaps in the contour. Opening always breaks a connected feature into several unconnected parts and eliminate small peaks, islands. In [55] Haralick says : "opening an image with a disk SE smoothes the contour, breaks narrow isthmuses, and eliminates small islands and sharp peaks or capes. Closing an image with a disk SE smoothes the contour, fuses narrow breaks and long thin gulfs, eliminates small holes, and fills gaps on the contours".

2.5 Grey-scale Morphological Filter

Grey-scale (GS) digital signal can be represented as sets whose components are in $\mathbb{Z}^2$, the discrete Euclidean space. In this case, one element refers to the co-ordinates of a sample, and the other refers to its discrete intensity value.

Let $f(n)$ and $g(n)$ denote respectively 1-D input signal and 1-D structuring element (SE), $D_f \subseteq \mathbb{E}$ and $D_g \subseteq \mathbb{E}$ denote their domains. Then 1-D GS erosion and dilation are defined as follows:

$$(f \ominus g)(n) = \min_{m}\{f(n+m) - g(m)\}, \tag{2.5.1}$$

$$(f \oplus g)(n) = \max_{m}\{f(n-m) + g(m)\}, \tag{2.5.2}$$

where $n, m \in D_g$ and $f(\alpha), \alpha \in D_f$. If the structuring element is flat (i.e., $g(m) = 0, \forall m \in D_g$), then the above equations can be simplified to:

$$(f \ominus g)(n) = \min_{m}\{f(n+m)\}, \tag{2.5.3}$$

$$(f \oplus g)(n) = \max_{m}\{f(n-m)\}, \tag{2.5.4}$$

2.6 Morphological Gradient

The basic Morphological Gradient (MG), also called *Beucher gradient*, is defined as the arithmetic difference between the dilation and the erosion by the structuring element B. This morphological gradient is denoted by ρ:

$$\rho_B = \delta_B - \varepsilon_B. \tag{2.6.1}$$

Here δ denotes dilation and ε denotes erosion. There are also two kinds of *half − gradient*. One is *half − gradient by erosion* or *internal gradient* ρ^-. It is defined as the difference between the original image and the eroded image:

$$\rho_B^- = I - \varepsilon_B. \tag{2.6.2}$$

The other is *half − gradient by dilation* or *external gradient* ρ^+ is defined as the difference between the dilated image and the original image[56]:

$$\rho_B^+ = \delta_B - I. \tag{2.6.3}$$

In the field of signal processing, morphological gradient is a effective transformation to extract the sudden changes. In this thesis, MG is applied to detect sudden undulations which is caused by fault current.

2.7 Top-Hat Operation

Top-Hat is defined as:

$$HAT(f) = f - (f \circ g), \tag{2.7.1}$$

as g is structuring element. The equation above is also named White Top Hat (WTH), while $(f \circ g) - f$ is named Black Top Hat (BTH). The Top-Hat operation is always used to extract the boundary of image parts. It is also used to determine the gray gradient of an image.

2.8 The importance of the reflection of the origin of the SE

In the rest of this section, the issue which is raised at the end of section 2.2.2 will be discussed. Firstly, if there is no reflection of the SE in the calculation of dilation, equations (2.4.1) and (2.4.2) can be rewritten as:

$$\begin{aligned} S \oplus G &= \{s+g : s \in S, g \in G\} = \bigcup_{g \in G} S_g, \\ S \ominus G &= \{x : G_x \subseteq S\} = \bigcap_{g \in G} S_g. \end{aligned}$$

The geometrical behavior of dilation by a structuring element without reflection is shown in Fig. 2.3 (c). Compared with the result of the standard dilation depicted in Fig. 2.2 (c), the dilation by a non-reflection SE expends the original image to the same size and same shape as the standard one, but the expanding direction of them are opposite. Such a difference causes translations to opening and closing depicted in Fig. 2.3 (d) and (e) respectively, which do not appear in the standard opening and closing. Furthermore, based on the definitions of the opening and the closing, both of them are idempotent, but from Fig. 2.3 (f), it is shown that if the non-reflection SE is adopted in dilation, the closing and the opening lose their idempotent property.

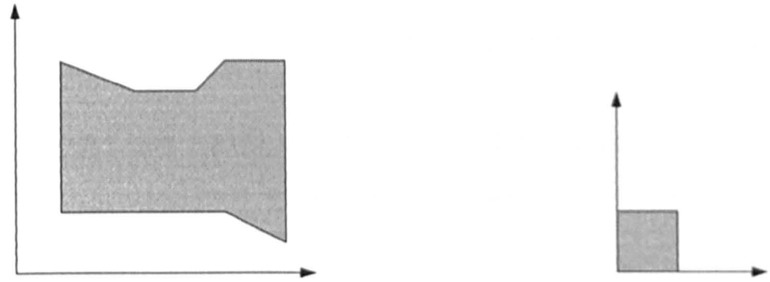

(a) Original image (b) Structuring element G

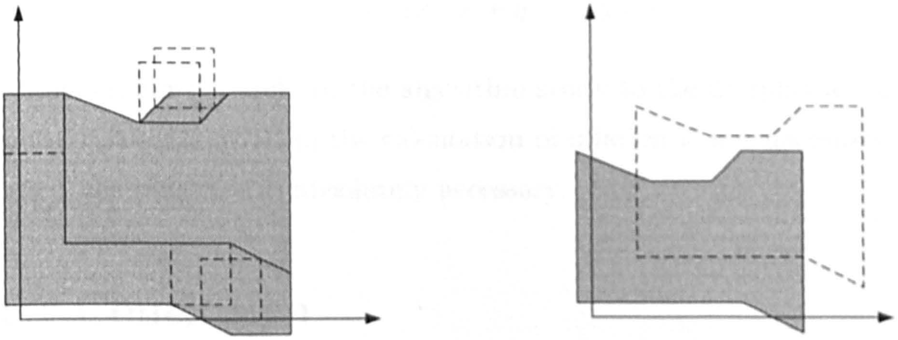

(c) δ_G (d) φ_G

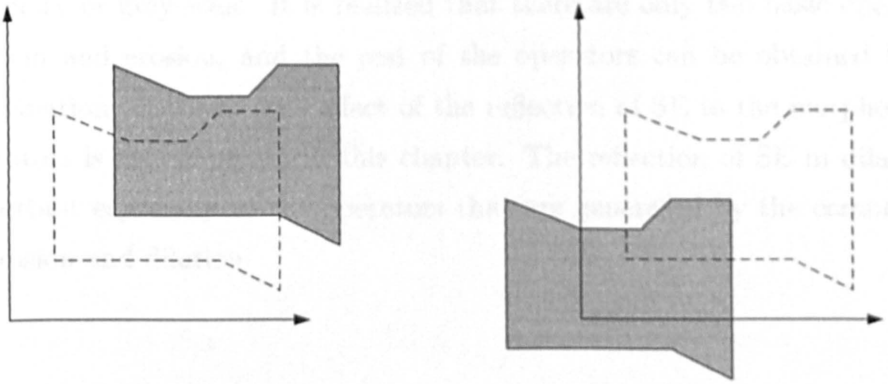

(e) γ_G (f) $\varphi_G(\varphi_G)$

Fig. 2.3: The effect of the reflection of SE in dilation to opening and closing. The origin of SE is at the bottom-left corner.

In practice, the non-reflection SE causes the result of Top-Hat incorrect: only the edges of the image can be extracted instead of the expected features. One obvious phenomenon is that the larger the SE is, the more the translation is.

On the other hands, the reflection of SE is not absolutely necessary. In Sternberg's definitions of erosion and dilation, the reflection is not adopted, which can be expressed as [57]:

$$\begin{aligned} S \oplus G &= \{s+g : s \in S; g \in G\}, \\ S \ominus G &= \{x : x+g \in S, g \in G\}. \end{aligned}$$

Based on our research, to the algorithm study to the morphological operators, the reflection of SE in the calculation of dilation is not necessary, but in practice, the reflection is absolutely necessary.

2.9 Conclusion

In this chapter the basic operators involved in MM were defined, mainly as binary or grey-scale. It is realized that there are only two basic operators: dilation and erosion, and the rest of the operators can be obtained by the combinations of them. The effect of the reflection of SE to the morphological operators is also analyzed in this chapter. The reflection of SE in dilation is important especially to the operators that are generated by the combination of erosion and dilation.

Chapter 3

Analyzing Weighted Dilation in the Frequency Domain

3.1 Introduction

Most of morphological analysis has been done in the time (or spatial) domain because of lack of transforms which make it possible to also describe them in a transform domain [19] [42] [58]. Heijmans and Maragos have built a transform named slope transform, by which morphological operators are endowed with eigenfunctions and related transfer functions in a transform domain [19] [20]. But a general 1-D signal does not bear significant characteristics and physical meanings in it. On the contrary, to 1-D signal, methods based on the frequency domain analysis have been the main methodology. Therefore, in this chapter, our attempt is to build a relationship between weighted morphological dilation and the traditional frequency domain analysis under the following conditions:

1. The input signal $f(n)$ is a mono ascending function and n are integers.
2. The structuring element $g(m)$ is a flat line segment, satisfies $g(m) = A > 0$; $m = 0, \cdots, M-1$, where M is the length of $g(m)$, A is a constant;

The derivations are based on two theories: weighted morphological filter and ED filter. ED filter employs parameter M and k, to sort the input signal in ascending order and extracts the kth element. Thus k sequences are generated and when $k = 1$, the sequence is erosion; when $k = M$, the sequence is dilation.

Based on this definition, weighted dilation is redefined in this chapter. Under the two preconditions, the relationship between the dilation and the other $k-1$ sequences is built. Furthermore, a mathematical relationship is also found between weighted dilation of $f(n)$, $g(m)$ and the convolution of them. Since the convolution of two signals in the time domain can be transformed to the multiplication of these two signals in the frequency domain, a weighted dilation of the function $f(n)$ with the structuring element $g(m)$ is transformed to a mathematical expression in the frequency domain.

Although the two preconditions are still very strict and only one morphological operator is analyzed in this chapter, the proposed derivations and algorithms provide some novel ideas in analyzing morphological operators in the frequency domain.

3.2 Weighted Morphological Filters

The definition of weighted morphological operators are firstly raised by Mohammand in his paper [31] [59]. The weighted morphological operators employ multiplication and division in place of addition and subtraction in classical morphological operations. The weighted morphological operators' performance dominate over classical ones for signals/images buried in salt and pepper, speckle and Gaussian noises.

Classical grey-scale (GS) erosion and dilation are defined as (2.5.1) and (2.5.2). The weighted erosion (WER) and dilation (WDI) are defined as:

$$\begin{aligned} \mathrm{WDI}[f(n), g(m)] &= \max_{m}\{f(n-m)g(m)\}, && (3.2.1)\\ \mathrm{WER}[f(n), g(m)] &= \min_{m}\{f(n+m)/g(m)\}; && (3.2.2)\end{aligned}$$

where $n, m \in D_g$ and to $f(\alpha)$, α satisfies $\alpha \in D_f$, $D_f \subseteq \mathbb{E}$ and $D_g \subseteq \mathbb{E}$ denote the domains of $f(n)$ and $g(n)$.

In Fig. 3.1 (a) the comparison between weighted dilation and traditional dilation is shown and the comparison between weighted erosion and classical erosion is illustrated in Fig. 3.1 (b). It is assumed that a voltage signal $s(t)$ is processed by WDI, WER, erosion and dilation respectively. The structuring element is a flat line $\{2, 2, 2, 2, 2\}$.

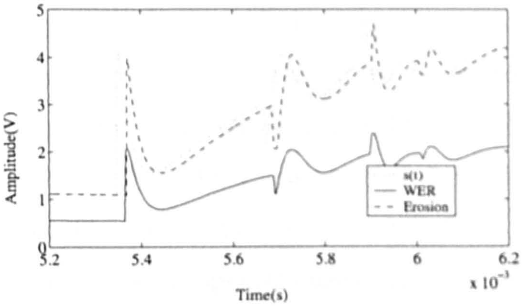

(a) Comparison between WER and erosion

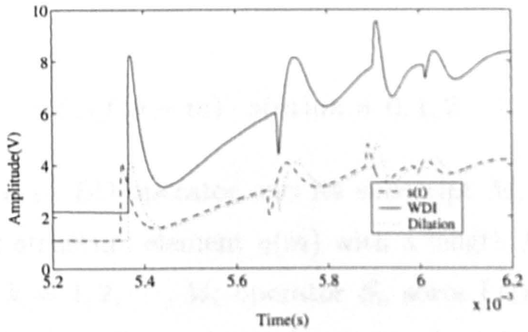

(b) Comparison between WDI and dilation

Fig. 3.1: Comparison between weighted MM operators and MM operators

It is apparent that in signal processing with the same structuring element, weighted MM operators and MM operators perform the same translations along the X-axis. But along the Y-axis, the traditional MM operators cause translation only. However, the weighted morphological operators achieve dilation or compression to the waveform as well as translation.

3.3 ED Filter

Erosion and Dilation (ED) filter is firstly introduced by Qi Li and Zheng Ji in [32]. ED filter applies an ED operator with two parameters M and k in place of the operator of max and min in traditional gray-scale dilation and erosion. The ED operator extracts the kth element from an input signal sequence in which its elements are sorted in an ascending order according to the structure element with the length of M. As k varies from 1 to M, M sequences are generated. When k is selected to be M or 1, ED filter can be regarded as Erosion or Dilation filter in these special cases [32].

In our works, ED filter is re-defined based on the theory of weighted morphological filter as follow:

$$f(n) \odot_{M,k} g(m) = S_k\{f(n-m)\cdot g(m)|m = 0,1,2,\cdots,M-1\}, \qquad (3.3.1)$$

where $\odot_{M,k}$ denotes an ED operator and its subscript M,k denotes that the ED filter has a flat structure element $g(m)$ with a length M and the order of ED filter is k and $k = 1,2,\cdots,M$; operator S_k sorts $\{f(n-m)\cdot g(m)|m = 0,1,2,\cdots,M-1\}$ in ascending order and extracts the kth value; n is integers, $f(n)$ is a real number sequence.

When $k = M$:

$$\begin{aligned} f(n) \odot_{M,M} g(m) &= S_M\{f(n-m)\cdot g(m)|m = 0,1,2,\cdots,M-1\} \\ &= \max_{m=0}^{M-1}\{f(n-m)\cdot g(m)\} \\ &= \mathrm{WDI}[f(n), g(m)]. \qquad (3.3.2) \end{aligned}$$

3.4 Analyzing Weighted Dilation in the Frequency Domain

Firstly, the conditions mentioned in the introduction of this chapter has to be re-emphasized.

1. the input signal $f(n)$ is a mono ascending function and n are integers.
2. The structuring element $g(m)$ is a flat line segment, satisfies $g(m) = A > 0$; $m = 0, \cdots, M-1$, M is the length of $g(m)$, A is a constant;

Based on our research, the following deductions and analysis are tenable under these conditions.

Based on (3.3.1) in the previous section, the following equation can be found:

Lemma:

$$\sum_{k=1}^{M} f(n) \odot_{M,k} g(m) = \sum_{m=0}^{M-1} f(n-m)g(m). \tag{3.4.1}$$

Proof: Based on (3.3.1), it is apparent that,

$$\begin{aligned}
& f(n) \odot_{M,1} g(m) \\
= \;& \mathcal{S}_1\{f(n-m)\cdot g(m) | m = 0, 1, 2, \cdots, M-1\} \\
= \;& \mathcal{S}_1\{f(n-0)g(0), f(n-1)g(1), \cdots, f(n-(M-1))g(M-1)\} \\
= \;& \min\{f(n-0)g(0), f(n-1)g(1), \cdots, f(n-(M-1))g(M-1)\}.
\end{aligned}$$

Since $f(n)$ is a mono ascending function and $g(m) = A > 0$, Then:

$$f(n-0)g(0) > f(n-1)g(1) > \cdots > f(n-(M-1))g(M-1). \tag{3.4.2}$$

Thus:

$$f(n) \odot_{M,1} g(m) = f(n-(M-1))g(M-1).$$

Based on (3.4.2), with k varied from 2 to M, it is easy to find that:

$$\begin{aligned}
f(n) \odot_{M,2} g(m) &= f(n-(M-2))g(M-2), \\
f(n) \odot_{M,3} g(m) &= f(n-(M-3))g(M-3), \\
&\;\;\vdots \\
f(n) \odot_{M,M} g(m) &= f(n-0)g(0).
\end{aligned}$$

Then:

$$\sum_{k=1}^{M} f(n) \odot_{M,k} g(m) = f(n) \odot_{M,1} g(m) + \cdots + f(n) \odot_{M,M} g(m)$$

$$\begin{aligned} &= f(n-(M-1))g(M-1)+\cdots+f(n-0)g(0) \\ &= \sum_{m=0}^{M-1} f(n-m)g(m). \end{aligned}$$

Furthermore, based on the definition of convolution:

$$f(n) * g(m) = \sum_{m=0}^{M-1} f(n-m)g(m),$$

then:

$$\sum_{k=1}^{M} f(n) \odot_{M,k} g(m) = f(n) * g(m). \tag{3.4.3}$$

Let

$$\begin{aligned} f(n) \odot_{M,M} g(m) &= r_M(n), \\ f(n) \odot_{M,M-1} g(m) &= r_{M-1}(n), \\ &\vdots \\ f(n) \odot_{M,1} g(m) &= r_1(n). \end{aligned}$$

From the deduction above, it is apparent that:

$$\begin{aligned} r_M(n) &= f(n-0)g(0), \\ r_{M-1}(n) &= f(n-1)g(1), \\ &\vdots \\ r_1(n) &= f(n-(M-1))g(M-1). \end{aligned}$$

$\because g(m) = A > 0$,

$\therefore r_{M-1}(n) = Af(n-1)$, compared with $r_M(n) = Af(n)$, it is found that:

$$r_{M-1}(n) = r_M(n-1)$$

Furthermore,

$$\begin{aligned} r_{M-2}(n) &= r_M(n-2), \\ r_{M-3}(n) &= r_M(n-3), \\ &\vdots \\ r_1(n) &= r_M(n-(M-1)). \end{aligned}$$

Then based on (3.4.3):

$$\begin{aligned}
&\sum_{k=1}^{M} f(n) \odot_{M,k} g(m) \\
= \; & f(n) \odot_{M,M} g(m) + f(n) \odot_{M,M-1} g(m) + \cdots + f(n) \odot_{M,1} g(m) \\
= \; & r_M(n) + r_{M-1}(n) + \cdots + r_1(n) \\
= \; & r_M(n) + r_M(n-1) + \cdots + r_M(n-(M-1)) \\
= \; & \sum_{m=0}^{M-1} r_M(n-m) = \sum_{m=0}^{M-1} f(n-m) g(m) = f(n) * g(m). \qquad (3.4.4)
\end{aligned}$$

Based on (3.3.2),

$$r_M(n) = f(n) \odot_{M,M} g(m) = \mathrm{WDI}[f(n), g(m)].$$

A mathematical relationship between the weighted dilation with structuring element $g(n)$ and the convolution of $f(n)$, $g(n)$ is formed.

Let $R_M(e^{j\omega})$, $F(e^{j\omega})$, $G(e^{j\omega})$ denote the discrete Fourier transform of $r_M(n)$, $f(n)$, $g(n)$ respectively. then according to (3.4.4),

$$\sum_{n=-\infty}^{+\infty} [\sum_{m=0}^{M-1} r_M(n-m)] e^{-j\omega n} = \sum_{m=0}^{M-1} [\sum_{n=-\infty}^{+\infty} r_M(n-m) e^{-j\omega n}] = F \cdot G \qquad (3.4.5)$$

According to the discrete-time Fourier time shifting property [60], the following transform is tenable:

$$\sum_{n=-\infty}^{+\infty} r_M(n-m) e^{-j\omega n} = R_M e^{-j\omega m},$$

then (3.4.5) can be transformed to:

$$\sum_{m=0}^{M-1} R_M e^{-j\omega m} = F \cdot G. \qquad (3.4.6)$$

The left portion of (3.4.6) is a geometric progression. it can be transformed to:

$$\sum_{m=0}^{M-1} R_M e^{-j\omega m} = R_M \frac{1 - e^{-j\omega M}}{1 - e^{-j\omega}},$$

then (3.4.6) can be transformed to:

$$\begin{aligned} R_M\frac{1-e^{-j\omega M}}{1-e^{-j\omega}} &= F\cdot G \\ \Rightarrow\quad R_M &= \frac{1-e^{-j\omega}}{1-e^{-j\omega M}}G\cdot F. \end{aligned}$$

Based on the preconditions mentioned at the beginning of this section, the structuring element $g(m)$ is a flat line segment which can be treated as a square waveform shown in Fig. 3.2.

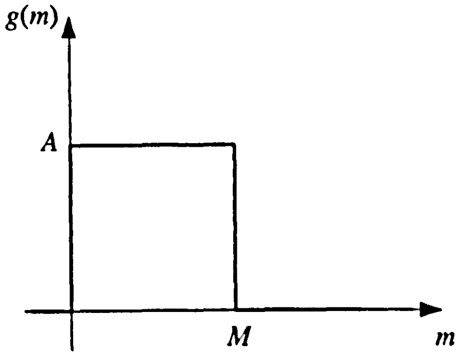

Fig. 3.2: Square waveform $g(m)$

Then the discrete Fourier transform of $g(m)$ is:

$$G = A\frac{\sin(\frac{\omega M}{2})}{\sin(\frac{\omega}{2})}e^{-j\omega(\frac{M-1}{2})},$$

then

$$R_M = [A\frac{\sin(\frac{\omega M}{2})}{\sin(\frac{\omega}{2})}\frac{1-e^{-j\omega}}{1-e^{-j\omega M}}e^{-j\omega(\frac{M-1}{2})}]\cdot F. \qquad (3.4.7)$$

In (3.4.7),

$$\begin{aligned} &\frac{1-e^{-j\omega}}{1-e^{-j\omega M}}e^{-j\omega(\frac{M-1}{2})} \\ =\ &\frac{e^{-j\omega(\frac{M-1}{2})}-e^{-j\omega(\frac{M+1}{2})}}{1-e^{-j\omega M}} \\ =\ &\frac{(e^{-j\omega(\frac{M-1}{2})}-e^{-j\omega(\frac{M+1}{2})})(1-e^{j\omega M})}{(1-e^{-j\omega M})(1-e^{j\omega M})}. \end{aligned}$$

Since:

$$\begin{aligned} & (1-e^{-j\omega M})(1-e^{j\omega M}) \\ = \; & 2-(e^{-j\omega M}+e^{j\omega M}) \\ = \; & 2-2\cos(\omega M), \end{aligned}$$

then:

$$\frac{(e^{-j\omega(\frac{M-1}{2})}-e^{-j\omega(\frac{M+1}{2})})(1-e^{j\omega M})}{(1-e^{-j\omega M})(1-e^{j\omega M})}=\frac{(e^{-j\omega(\frac{M-1}{2})}-e^{-j\omega(\frac{M+1}{2})})(1-e^{j\omega M})}{2-2\cos(\omega M)}.$$

Furthermore:

$$\begin{aligned} & (e^{-j\omega(\frac{M-1}{2})}-e^{-j\omega(\frac{M+1}{2})})(1-e^{j\omega M}) \\ = \; & e^{-j\omega(\frac{M-1}{2})}-e^{j\omega(\frac{M+1}{2})}-e^{-j\omega(\frac{M+1}{2})}+e^{j\omega(\frac{M-1}{2})} \\ = \; & 2\cos(\omega\frac{M-1}{2})-2\cos(\omega\frac{M+1}{2}), \end{aligned}$$

thus:

$$\frac{1-e^{-j\omega}}{1-e^{-j\omega M}}e^{-j\omega(\frac{M-1}{2})}=\frac{\cos(\omega\frac{M-1}{2})-\cos(\omega\frac{M+1}{2})}{1-\cos(\omega M)}.$$

Then (3.4.7) can be transformed to:

$$R_M=A\frac{\sin(\frac{\omega M}{2})[\cos(\omega\frac{M-1}{2})-\cos(\omega\frac{M+1}{2})]}{\sin(\frac{\omega}{2})[1-\cos(\omega M)]}\cdot F. \qquad (3.4.8)$$

$A\frac{\sin(\frac{\omega M}{2})[\cos(\omega\frac{M-1}{2})-\cos(\omega\frac{M+1}{2})]}{\sin(\frac{\omega}{2})[1-\cos(\omega M)]}$ is the discrete time Fourier transform of weighted dilation operator under the two preconditions and its properties are determined by two parameters: the amplitude of the structuring element A and the length of the structuring element M. In Fig. 3.3, the effects of weighted dilation in the frequency domain with the variety of M is illustrated. It is shown that with the increasing of the length of the structuring element, more noises are endued.

Thus, a weighted morphological operator is endowed a rigorous mathematical expression in the frequency domain. The proposed deductions in this chapter provides a way for the further analysis of the morphological operators' properties in the frequency domain. Especially (3.4.1), it is a bridge between the weighted dilation of $f(n)$, $g(m)$ and the convolution of them. It is believed that (3.4.1) is also correct to arbitrary $f(n)$ and $g(m)$, but a strict proof has not been found yet.

3.5 Conclusion

The exposition in this chapter is largely theoretical. The objective of the work presented in this chapter is to provide a rigorous theoretical connection between the morphological operators and the frequency domain analysis.

Under the two preconditions, weighted morphological dilation with a structuring element $g(m)$ is transformed to a mathematical expression in the frequency domain. Compared with slope transform by which the morphological dilation is transformed to addition, our contribution is very complex, but the transform of weighted dilation in the frequency domain gives us a clear vision of the effect of the morphological operators to the signal's frequency properties.

Although the proposed methods still cannot be applied to arbitrary signals, the proposed derivations, algorithms and analyzing methods provide novel ideas in applying morphological operators to 1-D signals.

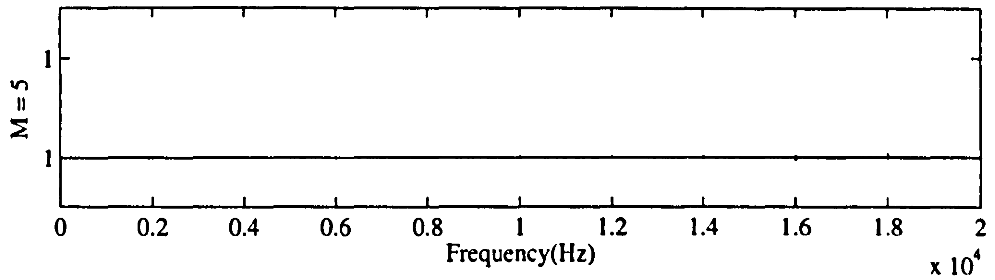

(a) When $M = 5$, the effect of weighted dilation in the frequency domain

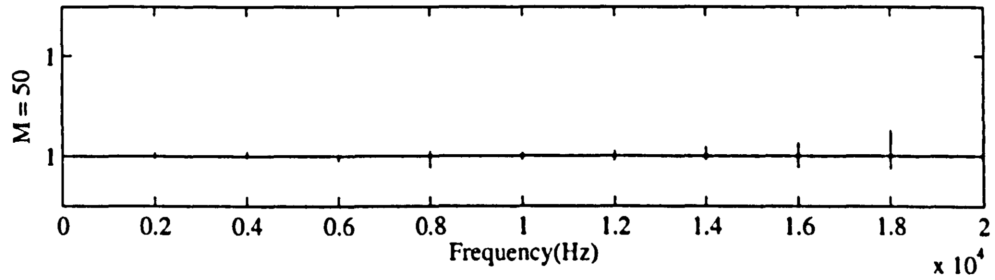

(b) When $M = 50$, the effect of weighted dilation in the frequency domain

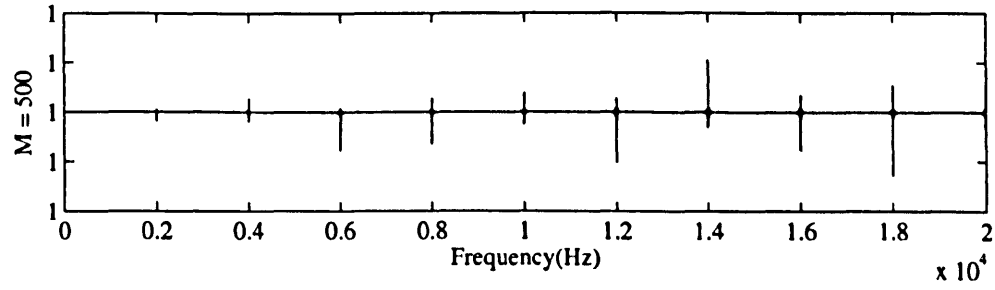

(c) When $M = 500$, the effect of weighted dilation in the frequency domain

Fig. 3.3: Comparing the effects of weighted dilation in the frequency domain with the variety of M; $A = 1$.

Chapter 4

Morphological Multi-resolution Decomposition Schemes

4.1 Introduction

It has been recognized that the multi-resolution signal decomposition schemes provide convenient and effective ways to process signals [21] [61] [62]. Most of the multi-resolution decomposition schemes are based on the theories of pyramid and wavelet, using the convolution and time-frequency domain transformation. In recent years, several researchers have proposed nonlinear multi-resolution signal decomposition schemes based on morphological operators [25] [26] [63] [64] [65]. However, until Goutsias and Heijmans presented a set of fundamental theories named Morphological Pyramid (MP) and Morphological Wavelet (MW), which are derived from traditional wavelet and pyramid theories, there was not a unified standpoint and framework for nonlinear pyramids, filter banks and wavelets, including morphological pyramids and wavelets construction [25]. MP and MW inherit the multi-dimension and multi-level analysis of wavelet and pyramid, whilst they do not require the time-frequency domain analysis. Furthermore, MP and MW extend the original wavelet and pyramid from the linear domain, which is based on the convolution and time-frequency domain transformation, to the nonlinear domain. The theories presented by Goutsias and Heijmans can be regarded as a framework for construction of the morphological wavelet and pyramid. Based on this framework, some schemes have been developed for specific applications of image processing. However the details of the operators proposed in this framework have not been investigated comprehensively.

In this chapter, three multi-resolution signal decomposition schemes– Multi-resolution Morphological Top-Hat scheme (MMTH), Multi-resolution Morphological Gradient scheme (MMG) and Multi-resolution Noise Tolerant Morphological Gradient scheme (MNTMG) are presented. All of them are based on Morphological Wavelet theories. The analysis operators and synthesis operators of the proposed schemes are constructed according to morphological coupled wavelet theories [25]. These schemes composed of morphological operators totally inherits the simple computation property of MM (Mathematical Morphology) operators. The mathematical calculation involved includes only addition, substraction, and sorting operations without any multiplication and division, which are used in other mathematical tools including Wavelet Transform. When acting upon complex shapes of signal, it is fast and easy to implement.

The idea of MMTH is first raised by Pu Sun in [33], in this chapter the operators is redefined based on morphological wavelet theory. The MMTH scheme adopts Top-Hat operator as its signal analysis operator which is an effective morphological technique for extracting locally bright objects in greyscale image processing [66]. The MMTH scheme shows its significant effect in distinguishing symmetrical features from asymmetrical features on the waveform.

The MMG scheme adopts morphological gradient as its signal analysis operator, which is frequently used for edge detection in image and signal processing. In this thesis, the MMG scheme is applied to characterize and recognize the sudden changes with sharp peaks and valleys on the waveform, and by decomposing the signal into different levels, the higher the level is processed, the more details of the sudden changes are revealed. In application, the MMG scheme is utilized to extract the fault generated transient features in power system protection. Since its operations are concerned with the shape of the signal waveform, which is the key point of analyzing the transient features superimposing upon the fundamental signal waveform, the advantages of the MMG scheme is apparent. But the simulation results show that although the performance of MMG is satisfactory under various fault conditions, it will inevitably deteriorate when various disturbances are imposed on the transient current signal. These disturbances can be considered as noise. In order to improve the accuracy of fault location, MNTMG decomposition scheme is constructed.

The analysis operators and synthesis operator of the MNTMG scheme are constructed according to morphological coupled wavelet theories. One of the analysis operators of MNTMG scheme is constructed by two parts, one is the morphological gradient operator and the other fulfills the noise reduction. Such a construction is efficient for extracting features from a transient signal with noise disturbance.

4.2 Basic Principles of Morphological Wavelet

4.2.1 Pyramid condition

To obtain a mathematical representation for a multi-resolution signal decomposition scheme, a sequence of signal domains, assigned at each level of the scheme, and analysis/synthesis operators that map information between different levels are needed [21] [25]. Each step towards a higher level is implemented by an analysis operator, whereas each step toward a lower level is implemented by a synthesis operator. This is a widely accepted approach to multi-resolution signal decomposition [67]. Moreover, Goutsias and Heijmans presented a set of theories to treat the analysis and synthesis operators from a general point of view.

Analysis and synthesis operators

Let $J \subseteq \mathbb{Z}$ be an index set indicating the levels in a multi-resolution signal decomposition scheme. J is considered to be finite or infinite. In the finite case, $J = \{0, 1, \cdots, K\}$, for $K < \infty$, whereas $J = \{0, 1, \cdots\}$ in the infinite case. A domain V_j of signals is assigned at each level j. No particular assumptions on V_j are made at this point (e.g., it is not necessarily true that V_j is a linear space). In this framework, signal analysis consists of decomposing a signal in the direction of increasing j. This task is accomplished by means of analysis operators $\psi_j^{\uparrow} : V_j \rightarrow V_{j+1}$. On the other hand, signal synthesis proceeds in the direction of decreasing j, by means of synthesis operators $\psi_j^{\downarrow} : V_{j+1} \rightarrow V_j$. Here, the upward arrow indicates that the operator $\psi^{\uparrow}$ maps a signal to a level higher in the pyramid, whereas the downward arrow indicates that the operator $\psi^{\downarrow}$ maps a signal to a level lower in the pyramid.

The signal can travel from any level in the pyramid to a higher level j by successively composing analysis operators. This gives an operator

$$\psi_{i,j}^{\uparrow} = \psi_{j-1}^{\uparrow}\psi_{j-2}^{\uparrow} \cdots \psi_i^{\uparrow}, \qquad j > i \qquad (4.2.1)$$

which maps an element in V_i to an element in V_j. On the other hand, the composed synthesis operator

$$\psi_{j,i}^{\downarrow} = \psi_i^{\downarrow}\psi_{i+1}^{\downarrow} \cdots \psi_{j-1}^{\downarrow}, \qquad j > i \qquad (4.2.2)$$

takes the signal back from level j to level i. Finally, the composition

$$\hat{\psi}_{j,i} = \psi_{j,i}^{\downarrow}\psi_{i,j}^{\uparrow}, \qquad j > i \qquad (4.2.3)$$

can be defined, which takes a signal from level i to level j and back to level i again.

Pyramid condition

In Goutsias and Heijmans' work, they distinguished between two types of multi-resolution decomposition. One is the pyramid scheme, the other is the wavelet scheme. Both of them consist of a number of levels such that the amount of information decreases towards a higher level. Each step towards a higher level is implemented by an analysis operator, whereas each step toward a lower level is implemented by a synthesis operator.

Synthesis operators and analysis operators must satisfy pyramid condition which plays an important role in constructing decomposition scheme operators. Consider a domain V_j of signal spaces and j is a finite of infinite index set. Assume that there is two families of operators, a family $\psi_j^{\uparrow}$ of analysis operators mapping V_j into V_{j+1} and a family $\psi_j^{\downarrow}$ of synthesis operators mapping V_{j+1} back into V_j. The synthesis and analysis operators must satisfy the pyramid condition which plays an important role in constructing the operators of the decomposition scheme. Consider a family V_j of signal spaces and j is a finite or an infinite index set. Here the signals consist of two families of operators, a family $\psi_j^{\uparrow}$ of analysis operators mapping V_j into V_{j+1} and a family $\psi_j^{\downarrow}$ of synthesis operators mapping V_{j+1} back into V_j. The analysis and synthesis operators $\psi_j^{\uparrow}$, $\psi_j^{\downarrow}$ are said to satisfy the pyramid condition if $\psi_j^{\uparrow}\psi_j^{\downarrow} = id$ on V_{j+1} where *id* is an identity operator.

The pyramid condition guarantees that no information is lost in two consecutive steps: synthesis and analysis. It is the fundamental principle used to construct pyramid and wavelet operators.

4.2.2 Pyramid transform

Block diagrams, illustrating the pyramid transform and its inverse, when $J = \{0, 1\}$, are depicted in Fig. 4.1. In Fig. 4.1, analysis of a signal $x \in V_j$, followed by synthesis, yields an approximation $\hat{x} = \hat{\psi}_{j,j+1}(x) = \psi_j^{\downarrow}\psi_j^{\uparrow}(x) \in \hat{V}_j$ of x, where $\hat{V}_j = V_{j+1}$. It assumed here that there exists a subtraction operator $(x, \hat{x}) \rightarrow x \dot{-} \hat{x}$ mapping $V_j \times \hat{V}_j$ into a set Y_j. Furthermore, assume that there exists an addition operator $(\hat{x}, y) \rightarrow \hat{x} \dot{+} y$ mapping $\hat{V}_j \times Y_j$ into V_j. The detail signal $y = x \dot{-} \hat{x}$ contains information about x which is not present in $\hat{x}$ and the detail signal y. Toward this goal, the assumption of perfect reconstruction is introduced below:

$$\hat{x} \dot{+} (x \dot{-} \hat{x}) = x, \text{ if } x \in V_j \text{ and } \hat{x} = \hat{\psi}_{j,j+1}(x).$$

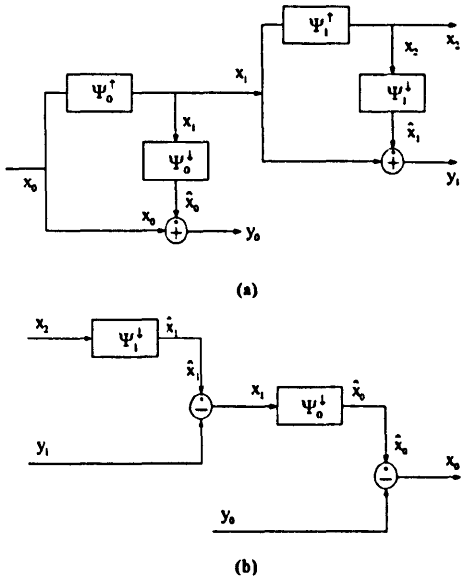

Fig. 4.1: Illustration of (a) a three-level pyramid transform and (b) its inverse.

This leads to the following recursive signal analysis scheme:

$$x \to \{y_0, x_1\} \to \{y_0, y_1, x_2\} \to \cdots \to \{y_0, y_1, \cdots, y_j, x_{j+1}\} \to \cdots \qquad (4.2.4)$$

$$\begin{cases} x_0 = x \in V_0 \\ x_{j+1} = \psi_j^\uparrow(x_j) \in V_{j+1}, \quad j \geq 0. \\ y_j = x_j \dot{-} \psi_j^\downarrow(x_{j+1}) \in Y_j \end{cases} \qquad (4.2.5)$$

Notice that, because of the perfect reconstruction condition, signal $x \in V_0$ can be exactly reconstructed from x_{j+1} and $y_0, y_1, \cdots, y_j$ by means of the backward recursion

$$x = x_0, \quad x_j = \psi_j^\downarrow(x_{x+1}) \dot{+} y_j, \quad j \geq 0. \qquad (4.2.6)$$

The process of decomposing a signal $x_0 \in V_0$ in terms of equations (4.2.4) and (4.2.5) will be referred to here as the pyramid transform of x, whereas the process of synthesizing x by means of equation (4.2.6) will be referred to as the inverse pyramid transform.

4.2.3 Coupled wavelet

Compared with the structure of morphological pyramid, morphological coupled wavelet is comprised two analysis operators: a signal analysis operator, a detail analysis operator, and one synthesis operator[25]. In Fig.(4.2) one stage of the coupled wavelet decomposition scheme is illustrated. In Fig(4.2), V_j and W_j are two sets: V_j is the signal space at level j and W_j is the detail space at level j; $\psi_j^{\uparrow} : V_j \rightarrow V_{j+1}$ is the signal analysis operator, $\omega_j^{\uparrow} : W_j \rightarrow W_{j+1}$ is the detail analysis operator and $\Psi_j^{\downarrow}$ is the synthesis operator to map the information back to the low level.

In order to guarantee that no information is lost and the decomposition is non-redundant, the analysis operators $\psi_j^{\uparrow}$, $\omega_j^{\uparrow}$ and synthesis operator $\Psi_j^{\downarrow}$ must follow the condition below:

$$\begin{aligned} &\psi_j^{\uparrow}(\Psi_j^{\downarrow}(x,y)) = x, \text{if } x \in V_{j+1},\ y \in W_{j+1}, \\ &\omega_j^{\uparrow}(\Psi_j^{\downarrow}(x,y)) = y, \text{if } x \in V_{j+1},\ y \in W_{j+1}. \end{aligned} \tag{4.2.7}$$

which is the pyramid condition when there are two analysis operators.

It is also required to yield a complete signal representation, in the sense that the mappings $(\psi_j^{\uparrow}, \omega_j^{\uparrow})$: $V_j \rightarrow V_{j+1} \times W_{j+1}$ and $\Psi_j^{\downarrow}$: $V_{j+1} \times W_{j+1} \rightarrow V_j$ are inverses of each other. This leads to the following condition:

$$\Psi_j^{\downarrow}(\psi_j^{\uparrow}(x), \omega_j^{\uparrow}(x)) = x, \text{if } x \in V_j. \tag{4.2.8}$$

Furthermore, given an input signal $x_o \in V_0$, consider the following recursive analysis scheme:

$$\begin{aligned} x_0 \rightarrow \{x_1, y_1\} &\rightarrow \{x_2, y_2, y_1\} \rightarrow \cdots \\ &\rightarrow \{x_k, y_k, y_{k-1}, \cdots, y_1\} \rightarrow \cdots \end{aligned} \tag{4.2.9}$$

where

$$\begin{aligned} x_{j+1} &= \psi_j^{\uparrow}(x_j) \in V_{j+1} \\ y_{j+1} &= \omega_j^{\uparrow}(x_j) \in W_{j+1},\ j \geq 0. \end{aligned} \tag{4.2.10}$$

The original signal x_0 can be exactly reconstructed from x_k and y_1, y_2, $\cdots$, y_k by means of the following recursive synthesis scheme:

$$x_j = \Psi_j^{\downarrow}(x_{j+1}, y_{j+1}),\ j = k-1,\ k-2,\ \cdots,\ 0 \qquad (4.2.11)$$

which show that the decomposition (4.2.9) and (4.2.10) is invertible. the signal representation scheme governed by (4.2.7)-(4.2.11) is referred to as the coupled wavelet decomposition scheme[25].

In this thesis, the following decomposition schemes adopt not only the structure of coupled wavelet which is demonstrated in Fig(4.2), but also the undecimated algorithm.

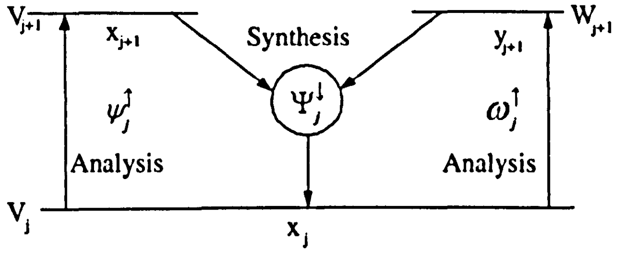

Fig. 4.2: One stage of the couple wavelet decomposition scheme.

The undecimated algorithm is based on the idea of no decimation. It applies the wavelet transform and omits both down-sampling in the forward and up-sampling in the inverse transform. More precisely, it applies the transform at each point of the signal and saves the detail coefficients and uses the low-frequency coefficients for the next level. In image processing, this algorithm gives the best results in terms of visual quality – less blurring for larger noise removal [63].

In the following sections, by selecting different analysis and synthesis operators, three different morphological undecimated wavelet decomposition schemes are presented. Furthermore, based on their respective properties, they are employed to fulfill the inrush current identification in transformer protection and fault transient extraction in transmission line protection in the following chapters respectively.

4.3 Morphological Multi-resolution Top-Hat Decomposition Scheme

The underlying basis of morphology filtering technique is to process signals by a function, known as the structuring element (SE) in general or structuring function for a 1-D signal. With various sequences of fundamental morphological operators, dilation and erosion, the technique is able to preserve or suppress the feature represented by SE and obtain a signal with only components of interest. Therefore, such an algebraic system with its operators and their combinations allows the underlying shapes to be identified, reconstructed and enhanced from their noisy, distorted forms. The Morphological Multi-resolution Top-Hat Decomposition Scheme (MMTH) is constructed under this strategy. The aim of MMTH is to separate the waveform into various level of details.

4.3.1 Proving the MMTH scheme satisfied the requirement of the coupled wavelet

The MMTH scheme adopts the construct of the coupled wavelet scheme which is denoted in Fig. 4.2. The signal analysis operator of MMTH decomposition scheme $\psi_j^{\uparrow}$ equals $\mathrm{id} - \gamma_{A_j}$; detail analysis operator $\omega_j^{\uparrow}$ equals γ_{A_j} and synthesis operator $\Psi_j^{\downarrow}$ equals $\mathrm{V}_{j+1} + \mathrm{W}_{j+1}$. It is shown that:

$$\begin{aligned} x_{j+1} = \psi_j^{\uparrow}(x_j) &= (\mathrm{id} - \gamma_{A_j})(x_j); \\ y_{j+1} = \omega_j^{\uparrow}(x_j) &= \gamma_{A_j}(x_j); \\ \psi_j^{\uparrow}(\Psi_j^{\downarrow}(x_{j+1}, y_{j+1})) &= \psi_j^{\uparrow}(\mathrm{id}(x_j)) = x_{j+1}. \end{aligned} \tag{4.3.1}$$

And it is easy to obtain $\omega_j^{\uparrow}(\Psi_j^{\downarrow}(x_{j+1}, y_{j+1})) = y_{j+1}$, while $x_j \in \mathrm{V}_j$, $x_{j+1} \in \mathrm{V}_{j+1}$ and $y_{j+1} \in \mathrm{W}_{j+1}$. So the analysis operators and synthesis operator of MMTH decomposition scheme are satisfied equation (4.2.7).

Furthermore,

$$\Psi_j^{\downarrow}(\psi_j^{\uparrow}(x_j), \omega_j^{\uparrow}(x_j)) = (\mathrm{id} - \gamma_{A_j})(x_j) + \gamma_{A_j}(x_j),$$

$$= x_j,$$

which shows that equation(4.2.8) is proved to be satisfied. It is not difficult to be proved that equations (4.2.9)-(4.2.11) are also satisfied. Therefore the MMTH decomposition scheme composed of $(\mathrm{id} - \gamma_{A_j})(x_j)$ as the analysis operator, $\gamma_{A_j}(x_j)$ as the detail analysis operator and $x_{j+1} + y_{j+1}$ as the synthesis operator is a coupled wavelet scheme, where $x_j \in \mathrm{V}_j$, $x_{j+1} \in \mathrm{V}_{j+1}$ and $y_{j+1} \in \mathrm{W}_{j+1}$.

The structuring element of the MMTH scheme G_j decreases as the increasing of j which can be expressed as:

$$G_{j+1} = \frac{1}{2}G_j, \qquad j = 0, 1, 2, \cdots, M. \tag{4.3.2}$$

G_M is 2 units in 1-D signal processing or a 2×2 units square in image processing, the structuring element G_0 is named Base SE (BSE).

4.3.2 The performance of MMTH scheme in image processing

The performance of the MMTH scheme in image processing is illustrated in Fig. 4.3. A 20 × 20 pixels square is chosen as the BSE A_1, and with the increasing of the index j of the structuring element A_j, the structuring element reduces to a 2 × 2 square according to equation (4.3.2). The results of the last two levels are obtained by the same SE: a 2 × 2 square; and since $\gamma_{A_5}(r_5)$ is null, the MMTH scheme decomposed the input image into 5 levels. Fig. 4.3, (a) is the input image; the results of $\psi_j^{\uparrow}$, $\omega_j^{\uparrow}$, $\Psi_j^{\downarrow}$ where $j = 1, 2, \cdots, 5$ are illustrated in Fig. 4.3 (b) to (p) respectively. In these figures, it is shown that the MMTH scheme can achieve lossless reconstruction to the lower level which are demonstrated in Fig. 4.3 (d), (g), (j), (m), (p).

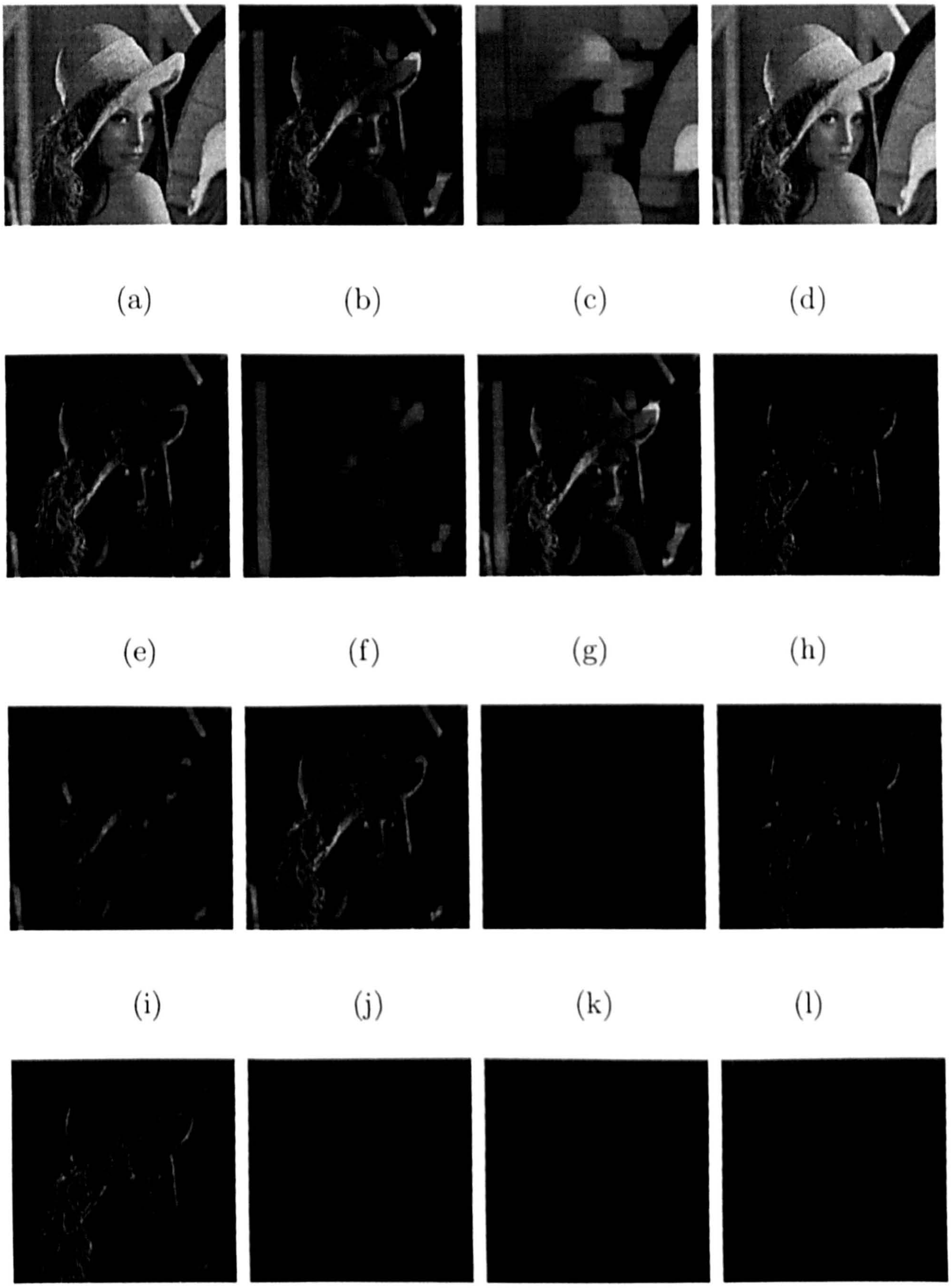

(a) (b) (c) (d)

(e) (f) (g) (h)

(i) (j) (k) (l)

(m) (n) (o) (p)

Fig. 4.3: The performance of the MMTH decomposition scheme in image processing. (a) is the input image; (b), (c), (d) are the results of $\psi_1^\uparrow$, $\omega_1^\uparrow$, $\Psi_1^\downarrow$ respectively; (e), (f), (g) are the results of $\psi_2^\uparrow$, $\omega_2^\uparrow$, $\Psi_2^\downarrow$ respectively; (h), (i), (j) are the results of $\psi_3^\uparrow$, $\omega_3^\uparrow$, $\Psi_3^\downarrow$ respectively; (k), (l), (m) are the results of $\psi_4^\uparrow$, $\omega_4^\uparrow$, $\Psi_4^\downarrow$ respectively; (n), (o), (p) are the results of $\psi_5^\uparrow$, $\omega_5^\uparrow$, $\Psi_5^\downarrow$ respectively.

4.3.3 The performance of MMTH scheme in distinguishing asymmetrical signal from symmetrical signal

In this thesis, the MMTH decomposition scheme in an attempt to apply morphological signal processing technique to the identification of inrush current, is utilized to characterize and recognize any unique feature in the inrush current, to distinguish it from internal fault conditions. Such features are the asymmetries of the inrush current in both amplitude and duration which is introduced in detail in the next chapter. To extract the asymmetrical features associated with the inrush current, MMTH is employed to separate the waveform into various level of details.

In Fig. 4.4, the performances of MMTH to a symmetrical signal and an asymmetrical signal are shown respectively. The BSE A_0 equals 8ms. According to equation (4.3.2), A_1=4ms, A_2=2ms. Compared Fig. 4.4 (a) and Fig. 4.4 (b), the difference between the symmetrical signal and the asymmetrical signal is apparent. To a symmetrical signal, the differences of the peak value of the adjacent levels equal that of the valley value of the adjacent levels. However, to an asymmetrical signal, the differences of the peak values between the adjacent levels are different with that of the corresponding valley values. For example, in Fig. 4.4 (b) the difference between the peak values of Level 1 (generated by $\psi_0^\uparrow$) and that of Level 2 (generated by $\psi_1^\uparrow$) is 0.25, while the difference of the corresponding valley values is only 0.05. However, in Fig. 4.4 (a), to a classical sine signal which is a symmetrical signal, the difference of the peak values between Level 1 and that of Level 2 equals the difference of the corresponding valley values which is 0.45.

Furthermore, if the input signal is not a standard sine signal but a sine signal with an exponential decreasing component $d(t)$, which is shown in Fig. 4.5 (a), the results are not affected, which is still 0.45 shown in Fig. 4.5 (b); and the difference of the corresponding peak and valley values are equivalent.

In order to describe the asymmetry of the signal shown in Fig. 4.4 (b) and the symmetry of the signal shown in Fig. 4.5 (a) more accurately, some

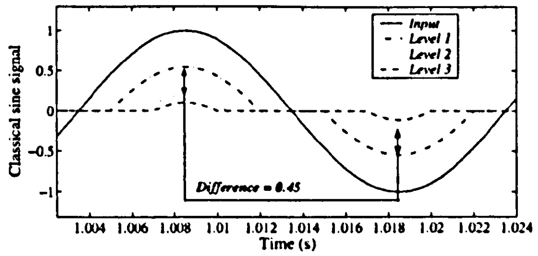

(a)The performance of MMTH to a symmetrical signal

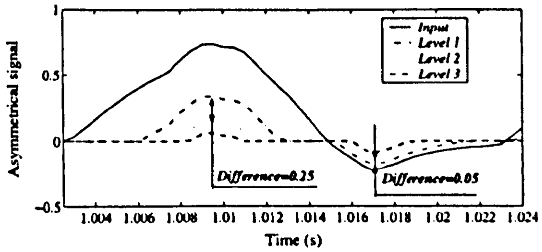

(b)The performance of MMTH to an asymmetrical signal

Fig. 4.4: The performance of MMTH scheme to a symmetrical signal and an asymmetrical signal

modifications are employed to equation (4.3.2):

$$G_{j+1} = G_j - a, \qquad j = 0, 1, 2, \cdots, M, \tag{4.3.3}$$

where the length of G_M is two units, a is a constant, in this thesis a =1ms.

Furthermore, a parameter δ_l is utilized to described the degree of the asymmetry of the signal. The definition of δ_l is presented as:

$$\delta_l = \frac{|A_{\max} - |A_{\min}||}{A_{\max} + |A_{\min}|}, \tag{4.3.4}$$

where $A_{\max}$ and $A_{\min}$ shown in Fig. 4.6 (a) are the maximum and minimum in one period of the signal respectively. In Fig. 4.6 (b), the variety of δ_l of the symmetrical signal and the asymmetrical signal with the increasing of the level of MMTH are illustrated. the BSE G_0 equals 10ms. It is shown that except the result of the 13th level, the difference between the asymmetrical signal and the symmetrical signal is apparent. Especially in the 4th Level, the difference reaches its maximum, and in this level a SE of 6ms is utilized.

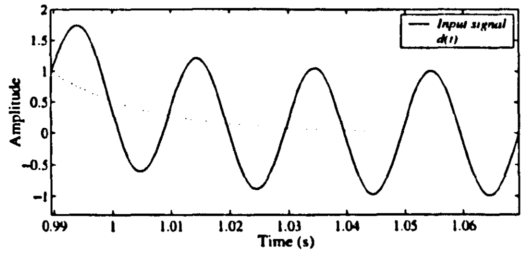

(a)A sine signal with an exponential decreasing component $d(t)$.

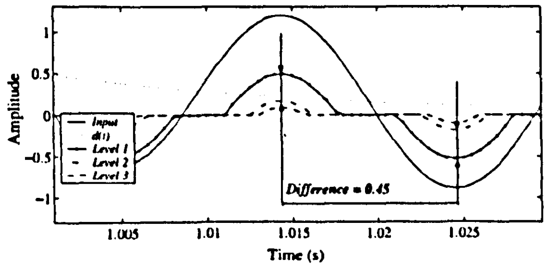

(b)The performance of MMTH

Fig. 4.5: The performance of MMTH scheme to a sine signal with an exponential decreasing component $d(t)$.

In practice, selecting a proper level as output and an optimal BSE are important in applying MMTH. A proper level with an optimal length of BSE should allow the asymmetry in the amplitude be accurately extracted, with a reasonable length of BSE to avoid excessive calculation, since the longer the structuring element is, the more computation effort expose to the morphology operation. Based on the analysis above and the experimental compressions, 9ms is chosen as the length of BSE, equation (4.3.3) is employed as the mechanism of the changing of the SE and the second level is selected as the output. The performance of MMTH with a BSE of 9ms length is illustrated in Fig. 4.7.

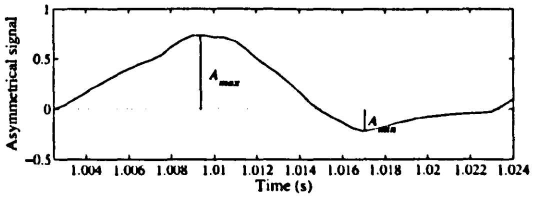

(a)The definitions of $A_{\max}$ and $A_{\min}$.

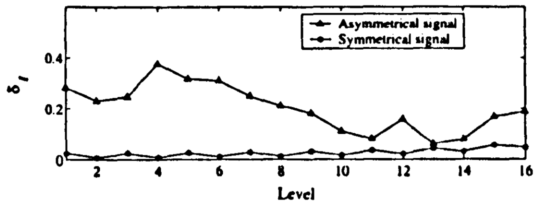

(b)The variety of δ_I of symmetrical signal and asymmetrical signal with the increasing of the level.

Fig. 4.6: The variety of δ_I of symmetrical signal and asymmetrical signal with the increasing of the level.

4.4 Multi-resolution Morphological Gradient

4.4.1 Multi-resolution morphological gradient

When the analysis operator $\psi_j^\uparrow = \rho_{g_j^+} - \rho_{g_j^-}$, detail analysis operator $\omega_j^\uparrow = \mathrm{id} - (\rho_{g_j^+} - \rho_{g_j^-})$ and the synthesis operator $\Psi_j^\downarrow = V_{j+1} + W_{j+1}$, the scheme, which is constructed by these operators and adopts the construction of coupled wavelet is named Multi-resolution Morphological Gradient (MMG). In the MMG scheme, morphological gradient ρ_A is employed as a part of the analysis operator and detail analysis operator. It is not difficult to prove that the MMG scheme satisfies equations (4.2.7)-(4.2.11), which are the necessary conditions of coupled wavelet scheme.

Morphological Gradient (MG) ρ_A is frequently used for edge detection in image and signal processing. The geometric illustration and effect of MG are depicted in Fig. 4.8, which demonstrates the process of MG computation for a ramped-step signal $f(x)$ by a flat SE g, where the symbol Δ indicates the

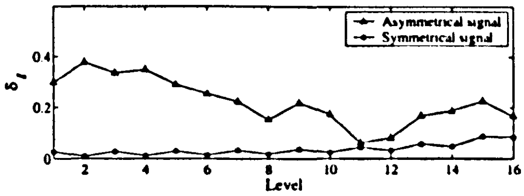

Fig. 4.7: When the length of BSE G_0 is 9ms, the performance of MMTH.

origin of the SE g. It should be noticed that there is a distinct meaning of MG, different from gradient in physics. Since the dilation and erosion using a flat SE have effects of maxima and minima morphological filtering, for every point, the MG is determined by the difference between maxima and minima obtained within the domain of the flat SE.

4.4.2 Analyzing the MMG decomposition scheme

In this thesis, MG is employed as the analysis operator of the MMG decomposition scheme with the attempt to analyze the sharp peaks and valleys on the waveform in details.

The efficiency of the MMG scheme is affected by many factors, the first factor is the length of the structuring element. In Fig. 4.9, a ramped-step signal $f(x)$ is processed by two flat SEs g_1 and g_2 respectively, where the symbol Δ indicates the origin of the SE. The only difference between g_1 and g_2 is that the lengths of these two SE l_{g_1} and l_{g_2} are different: $2l_{g_1} = l_{g_2}$. It is apparent that by SE g_2 the shape of peak on the waveform is dilated and extracted; while by SE g_1, the ascending edge and descending edge of the ramped-step are extracted. Variable SE with different length can fulfill different tasks. Based on this analysis, in the MMG decomposition scheme, a scalable flat line SE with different lengths is employed.

In the MMTH decomposition scheme two scalable SEs are also employed, which are expressed as equations (4.3.2) and (4.3.3) respectively. Compared with equation (4.3.2), although by utilized the scalable SE based on equation

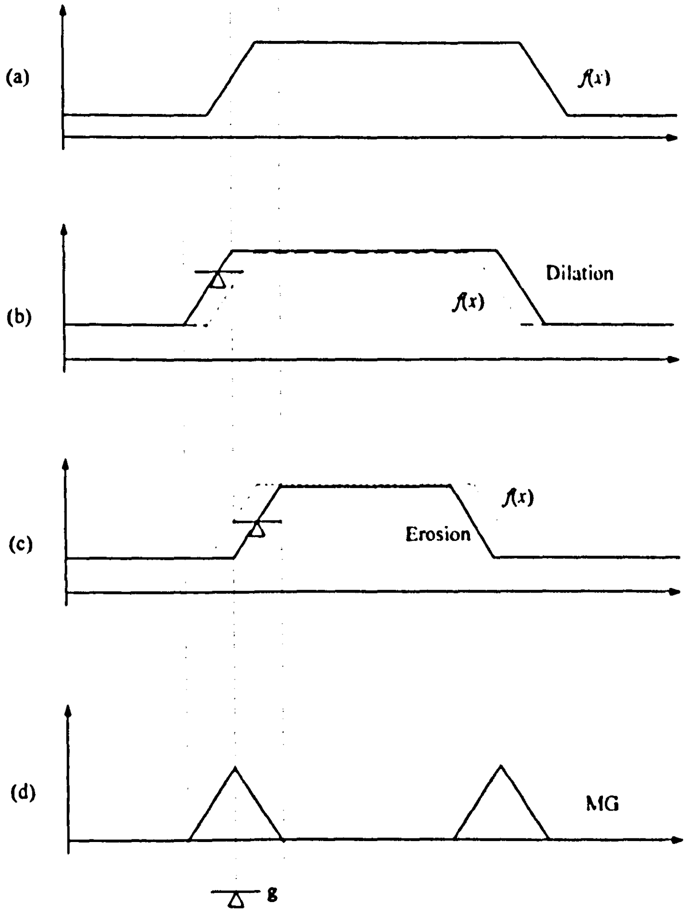

(a)signal $f(x)$ (b)dilation (c) erosion (d)gradient

Fig. 4.8: The calculation and effect of morphological gradient.

(4.3.3) more detail about the changes of the signal are revealed, the calculation takes much more time as well. Furthermore in practice it is not necessary to be so accurate. Based on these analysis, the scalable SE based on equation (4.3.2) is employed as the mechanism of the structuring element of the MMG scheme.

The second factor that affects the efficiency of the MMG scheme is the origin of the structuring element. In Fig. 4.9 (c) although by utilized SE g_1 the ascending edge and descending edge of the ramped-step are extracted, the two edges cannot be distinguished from the result of MMG. in order to solve

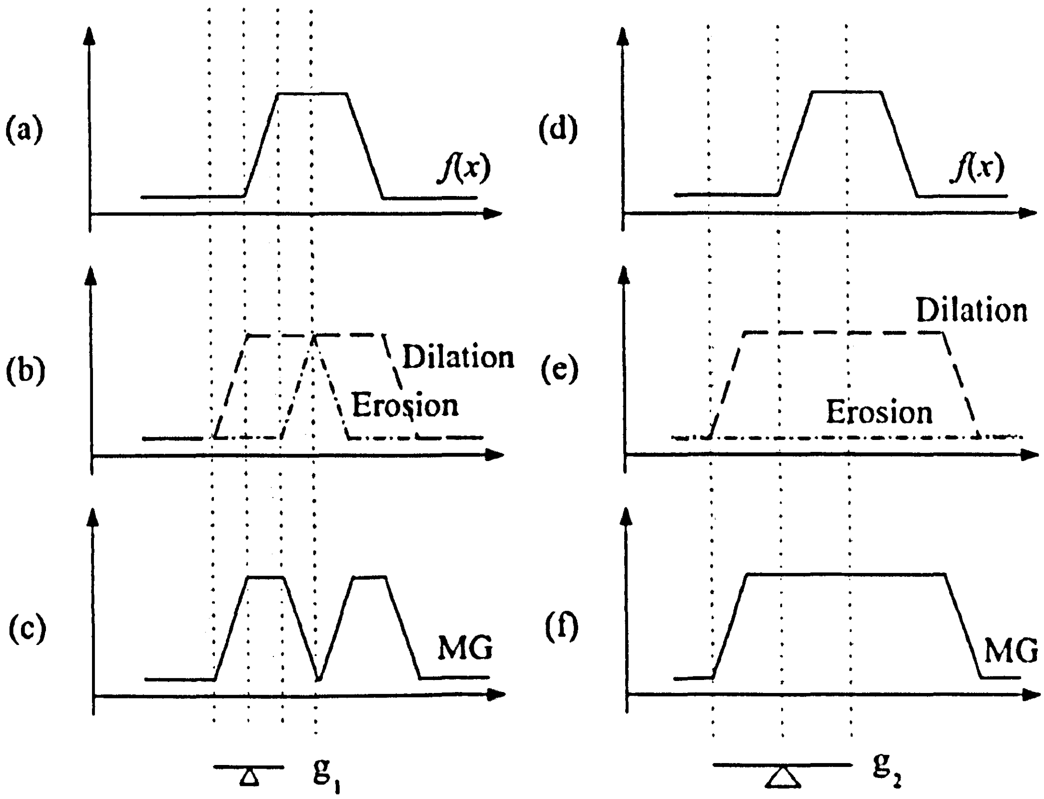

Fig. 4.9: The calculation and effect of morphological gradient. (a) and (d) illustrate signal $f(x)$; (b) and (e) illustrate the results of dilation and erosion with SE g_1 and g_2 respectively; (c) and (f) illustrate the results of MG with g_1 and g_2 respectively.

this problem, the scalable flat line SE bears not only variable lengths, but also different origins, which are defined as:

$$g^+ = \{g_1, g_2, \ldots, g_{l-1}, \underline{g_l}\}, \tag{4.4.1}$$

$$g^- = \{\underline{g_1}, g_2, \ldots, g_{l-1}, g_l\}, \tag{4.4.2}$$

where g^+ is the SE used for extracting the ascending edges and g^- is for the descending edges. The underlined samples, $\underline{g}$, in g^+ and g^- show their origins. It is easy to find that:

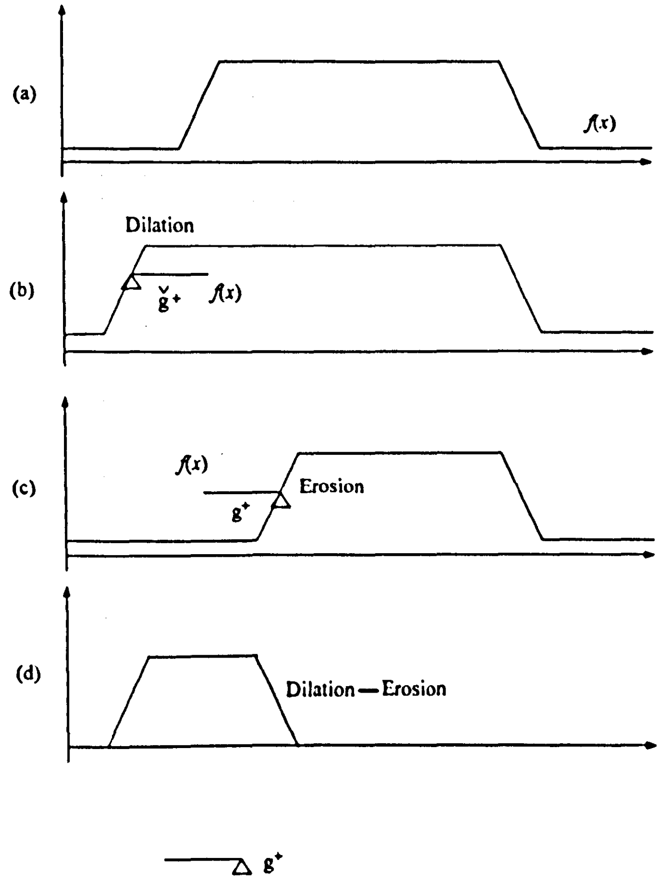

(a)signal $f(x)$ (b)dilation (c) erosion (d)gradient

Fig. 4.10: Morphological gradient by a flat SE with the origin at its rightmost.

$$g^- = \check{g}^+, \tag{4.4.3}$$
$$g^+ = \check{g}^-, \tag{4.4.4}$$

where $\check{g}$ is the reflection of g around its origin.

Based on the definition of MG, the scalable flat SE in equation (4.3.2) and the scalable flat SE in equations (4.4.1) and (4.4.2), the analysis operator of MMG $\psi_j^\uparrow$ is defined as:

$$\psi_j^\uparrow = \rho_{g_j^+}(x_j) - \rho_{g_j^-}(x_j), \tag{4.4.5}$$

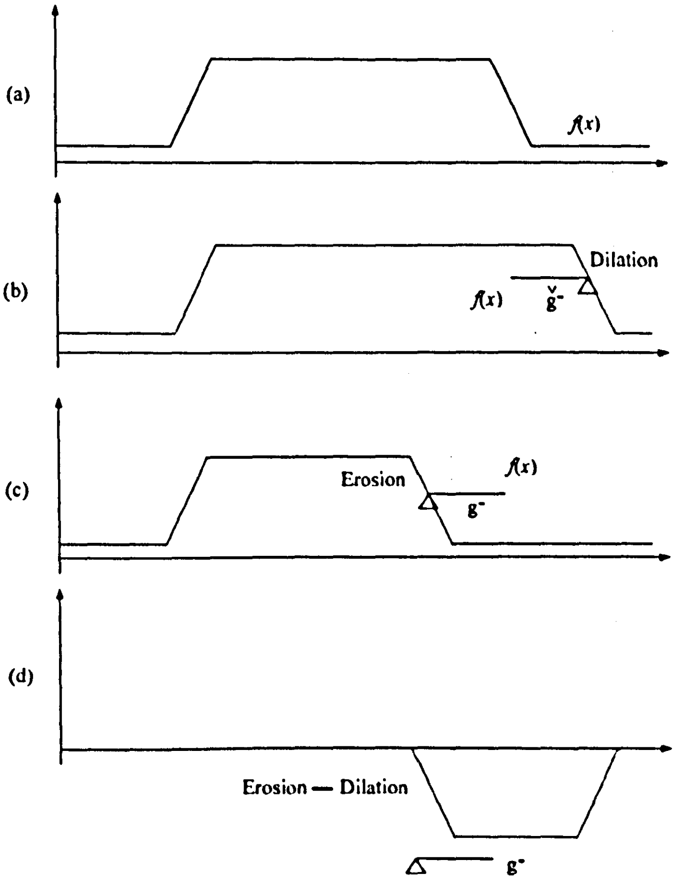

(a)signal $f(x)$ (b)dilation (c) erosion (d)gradient

Fig. 4.11: Morphological gradient by a flat SE with the origin at its leftmost.

where g_j^+ is a flat line SE with the origin at its rightmost and the origin of g_j^- is at leftmost; the length of g_j^+ denoted as $l_{g_j^+}$ and that of g_j^- denoted as $l_{g_j^-}$ satisfy $l_{g_{j+1}^+} = \frac{1}{2} l_{g_j^+}$ and $l_{g_{j+1}^-} = \frac{1}{2} l_{g_j^-}$ respectively.

The explanations of $\rho_{g_j^+}$ at level 1 is geometrically illustrated in Fig. 4.10. The solid lines in Fig. 4.10 (b) and (c) are the result of dilation and erosion in comparison with the input signal depicted in dashed lines. It is clear that the flat SE with the origin at the rightmost, indicated by symbol Δ in Fig. 4.10, only affects the ascending edges by both dilating and eroding operations, because the origin of the flat SE should fall in the umbra of the input signal.

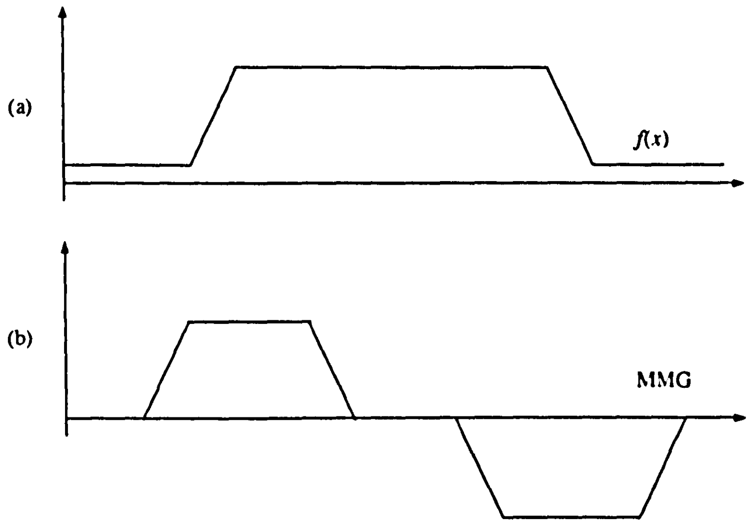

(a)signal $f(x)$ (b)MMG

Fig. 4.12: A signal and its MMG at first level.

Due to the geometrical symmetry of $\rho_{g_j^+}$ defined as the difference between the dilation and the erosion depicted in Fig. 4.10 (d), there is no position shifting introduced in MMG of detected signal waveform changes. Likewise, a process of computing descending edges of the signal waveform by MMG at level 1 with the origin at the flat SE's leftmost, defined as $-\rho_{g_j^-}$, is geometrically demonstrated in Fig. 4.11.

From Figs. 4.12, it is shown that the MMG scheme is able to detect not only the exact location of waveform changes but also their polarities (changing directions).

The third factor that affects the efficiency of the MMG scheme is the decomposition levels. In Fig. 4.13, a waveform with sharp peak and valley is analyzed using MMG. The length of the Base SE is 10 sampling points, the input signal is processed by the MMG in three levels as shown in Fig. 4.13 (b), (c) and (d). In Fig. 4.13 (b), it is shown that the analysis operator in the first level $\psi_1^{\uparrow}$ cannot depress the steady state components completely and in 4.13 (d) the analysis operator in the third level $\psi_3^{\uparrow}$ reduces the amplitude of the signal too hard to be explored in practice, so the result of $\psi_2^{\uparrow}$ is chosen

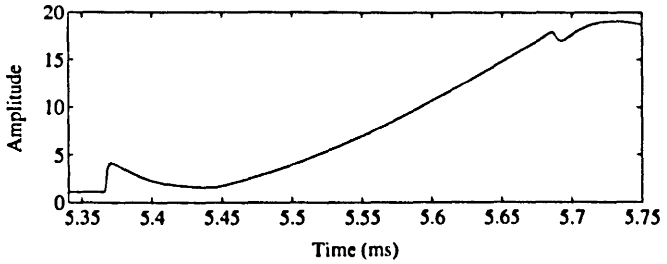

(a)Input signal

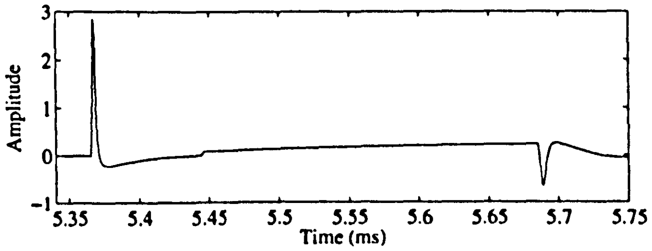

(b)The output of $\psi_1^{\uparrow}$

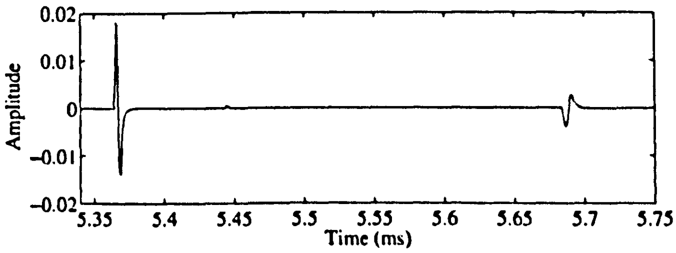

(c)The output of $\psi_2^{\uparrow}$

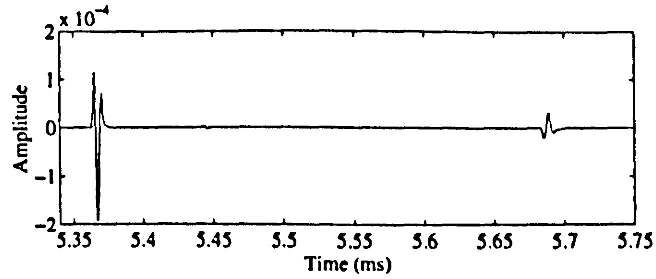

(d)The output of $\psi_3^{\uparrow}$

Fig. 4.13: The sharp peak and valley extraction using the MMG.

as the output named quadratic MMG scheme, which is employed in extracting the fault generated transient features in the power system protection.

4.4.3 Transient features extraction using MMG

In the thesis, the MMG scheme is applied to extract the fault generated transient wavefronts in the application of power system protection. The application aims at characterizing and recognizing the unique features involved in the transient signals, which is manifested by a series of sudden changes with sharp peaks and valleys on the waveform.

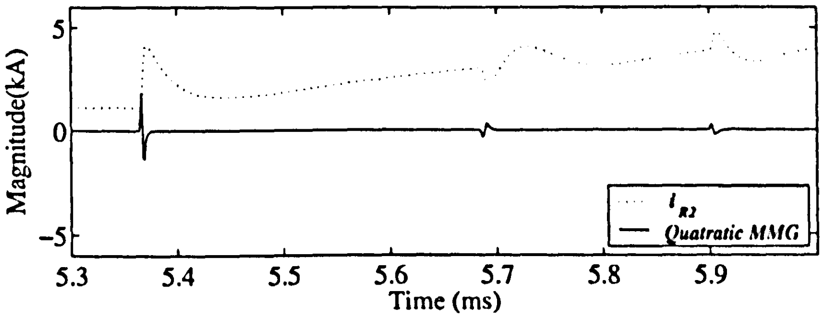

Fig. 4.14: The performance of quadratic MMG in the transient features extraction.

The performance of the quadratic MMG by choosing a flat line segment with the length of 25ms as the Base SE is illustrated in Fig. 4.14. In comparison with general methods and the method based on wavelet transform which is introduced in [68], the advantages of the MMG scheme consist in the following aspects:

Accurately pinpointing the transient wavefronts: Firstly, its computation is carried out in the complete time-domain without involving any transformation algorithm such as Fourier or Wavelet transform, which reflect the integral value over a given interval. Secondly, it introduces very little time delay in the MMG due to its short shifting data-window.

Explicitly indicating the polarities of transient waves: The changing directions of the transient wavefronts can be identified by the positive or negative pulses in the MMG at level 1, and by the positive pulse leading or legging its negative pulse in the MMG at level 2.

Easy recognition: Its processing result exhibits a fairly regular and explicit shape, which is easy to be recognized in terms of its maxima and polarity.

A multi-resolution method: Comparing the MMG in level 1,2 and 3, shown in Figs. 4.13(b), (c) and (d) respectively, reveals that the higher the level is processed, the more details about changes are revealed.

A fast algorithm implementation: Its implementation is very simply and just requires addition and comparison operations without requiring any multiplication operation. This merit makes it very suitable for ultrahigh-speed protection with 11s sampling period.

In transient feature extraction, the proposed MMG technique also has its limitation:

Lack of quantitively analytical methods: Firstly, the MM technique is lack of quantitively analytical methods, due to the non-linearity of the set operations. It means that the exact magnitude and argument of the specified signal component can not be obtained through the MM technique. How to accurately calculate the magnitude and argument of the measurand is usually to be the departure point of designing conventional protection for power engineers, who are familiar with the linear transform methods such as Fourier analysis. In order to solve this problem, in Chapter 3 of this thesis, the author attempts to build a determinate relationship between MM operators and the classical analysis methods such as frequency analysis. In Chapter 3 some of the MM operators are transformed to general transfer functions in the frequency domain, although the restrictions are very strict.

Easily affected by noise: the MMG decomposition scheme is sensitive to the transient features as well as to the noise which is analyzed in details in Chapter 7. In order to improve the MMG scheme to be noise tolerant, a novel decomposition scheme is constructed which is introduced in the next section.

4.5 Multi-resolution Noise Tolerant Morphological Gradient Decomposition Scheme

In order to improve the MMG scheme to be noise tolerant, Multi-resolution Noise Tolerant Morphological Gradient decomposition scheme (MNTMG) is constructed. The signal analysis operator of MNTMG $\psi_j^{\uparrow}$ equals $\frac{1}{2}(\delta\gamma - \varepsilon\phi + \delta - \varepsilon)$; detail analysis operator $\omega_j^{\uparrow}$ equals $\mathrm{id} - \frac{1}{2}(\delta\gamma - \varepsilon\phi + \delta - \varepsilon)$ and synthesis operator $\Psi_j^{\downarrow}$ equals $V_{j+1} + W_{j+1}$. It is shown that:

$$\begin{aligned} x_{j+1} = \psi_j^{\uparrow}(x_j) &= \frac{1}{2}(\delta\gamma - \varepsilon\phi + \delta - \varepsilon)(x_j); \\ y_{j+1} = \omega_j^{\uparrow}(x_j) &= [\mathrm{id} - \frac{1}{2}(\delta\gamma - \varepsilon\phi + \delta - \varepsilon)](x_j); \\ \psi_j^{\uparrow}(\Psi_j^{\downarrow}(x_{j+1}, y_{j+1})) &= \psi_j^{\uparrow}(\mathrm{id}(x_j)) = x_{j+1}. \end{aligned} \tag{4.5.1}$$

And it is easy to obtain $\omega_j^{\uparrow}(\Psi_j^{\downarrow}(x_{j+1}, y_{j+1})) = y_{j+1}$, while $x_j \in V_j$, $x_{j+1} \in V_{j+1}$ and $y_{j+1} \in W_{j+1}$. So the analysis operators and synthesis operator of MNTMG decomposition scheme are satisfied equation (4.2.7).

Furthermore,

$$\begin{aligned} \Psi_j^{\downarrow}(\psi_j^{\uparrow}(x_j), \omega_j^{\uparrow}(x_j)) &= \frac{1}{2}(\delta\gamma - \varepsilon\phi + \delta - \varepsilon)(x_j) + \\ &\quad [\mathrm{id} - \frac{1}{2}(\delta\gamma - \varepsilon\phi + \delta - \varepsilon)](x_j), \\ &= x_j, \end{aligned}$$

which shows that equation(4.2.8) is proved to be satisfied. It is not difficult to be proved that equations (4.2.9)-(4.2.11) are also satisfied. So the MNTMG decomposition scheme composed of $\psi_j^{\uparrow}(x_j) = [\frac{1}{2}(\delta\gamma - \varepsilon\phi + \delta - \varepsilon)](x_j)$ as the analysis operator, $\omega_j^{\uparrow}(x_j) = [\mathrm{id} - \frac{1}{2}(\delta\gamma - \varepsilon\phi + \delta - \varepsilon)](x_j)$ as the detail analysis operator and $\Psi_j^{\downarrow}(x_{j+1}, y_{j+1}) = x_{j+1} + y_{j+1}$ as the synthesis operator is a coupled wavelet scheme, where $x_j \in \mathrm{V}_j$, $x_{j+1} \in \mathrm{V}_{j+1}$ and $y_{j+1} \in \mathrm{W}_{j+1}$.

According to equations (2.4.3) and (2.4.4), the signal analysis operator of MNTMG decomposition scheme can be transformed to

$$\begin{aligned} & \frac{1}{2}(\delta\delta\varepsilon - \varepsilon\varepsilon\delta + \delta\varepsilon\delta - \varepsilon\delta\varepsilon) \\ = & \frac{1}{2}[(\delta - \varepsilon)\delta\varepsilon + (\delta - \varepsilon)\varepsilon\delta] \\ = & \frac{1}{2}(\delta\varepsilon + \varepsilon\delta)(\delta - \varepsilon). \end{aligned} \tag{4.5.2}$$

Equation(4.5.2) shows that the signal analysis operator is composed of two parts: $\frac{1}{2}(\delta\varepsilon + \varepsilon\delta)$ and $(\delta - \varepsilon)$. The latter one is morphological gradient operator which plays an important role in the quadratic MMG scheme, while the operator $\frac{1}{2}(\delta\varepsilon + \varepsilon\delta)$ is to depress noise and its performance is shown in Fig. 4.15 (b); the length of SE is 5ms. Compared with the performance of the quadratic MMG to a signal i_{R2} with $SNR = 30.30$dB as shown in Fig. 4.15 (c), by applying noise reduction operator $\frac{1}{2}(\delta\varepsilon + \varepsilon\delta)$ interactively, the MNTMG scheme can effectively extract transient features from a noise imposed signal as shown in Fig. 4.15 (d).

4.6 Conclusion

This chapter has briefly introduced the basic principles of morphological pyramid and morphological wavelet. Based on the elementary MM operators and the basic multi-resolution morphological decomposition theories, three morphological decomposition schemes have been developed, which are MMTH aiming at analyzing symmetrical properties of the signal, MMG aiming at extracting sudden changes on the waveform of the signals and MNTMG aiming at extracting sharp of peaks and valleys on the waveform of a noise imposed signal.

The desirable properties demonstrated in the analysis of these three techniques, manifest the morphological multi-resolution decomposition schemes as

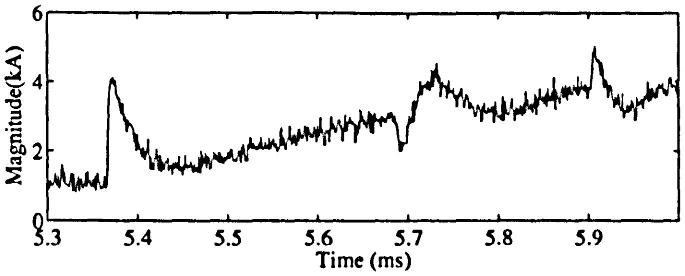

(a) The input signal i_{R2} with $SNR = 30.30dB$.

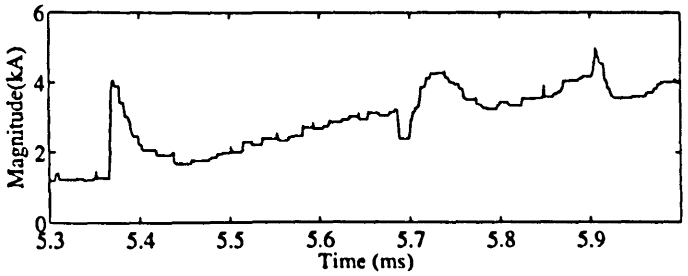

(b) The performance of the operator $\frac{1}{2}(\delta\varepsilon + \varepsilon\delta)$ in the first level of the MNTMG.

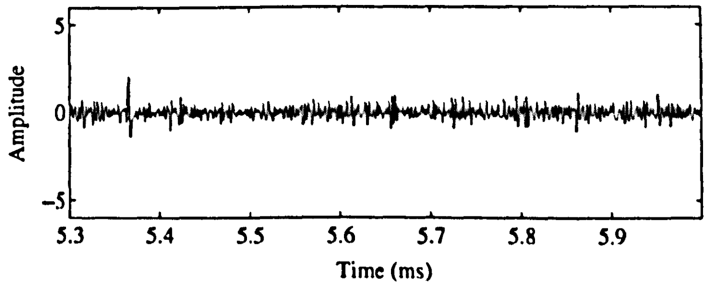

(c) The performance of the quadratic MMG to the input signal i_{R2}.

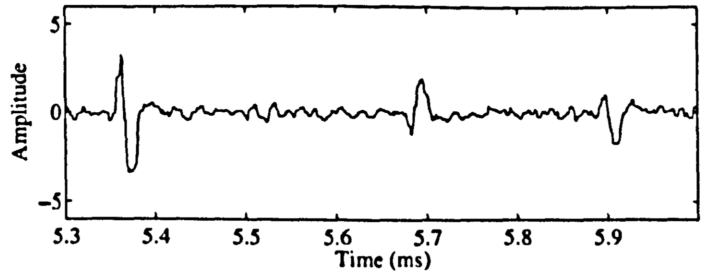

(d) The performance of the quadratic MNTMG to the input signal i_{R2}.

Fig. 4.15: Comparison between the MMG scheme and the MNTMG scheme.

promising method in signal processing. In Chapter 5, the MMTH scheme is employed in the application of distinguishing magnetizing inrush currents from internal faults. In Chapter 6, by applying the MMG filtering technique, the fault-generated transient features in the voltage and current signals will be extracted and recognized by MMGs' maxima and polarities. In Chapter 7, the MMG scheme and the MNTMG scheme are used in exactly locating the transient wavefronts under the conditions of non-noise disturbance and noise disturbance respectively. Further discussion about these three schemes will be presented in the following chapters.

Chapter 5

Identification of Transformer Magnetizing Inrush Current Using Morphological Multi-resolution Top-Hat Scheme

5.1 Introduction

The continuity of power transformer operation has been recognized as being of vital importance in maintaining the reliability of electric power system, where the protection of large power transformers still remains one of the most challenging problems in the area of power system relaying.

Differential protection has been applied so far as the primary protection for large power transformers. It detects every type of internal fault while blocking trip signals caused by inrush, over-excitation and external faults. Magnetizing inrush currents in power transformers result from any abrupt change of the magnetizing voltage. Usually, its waveform displays a large and long lasting DC component, is rich in harmonics, assumes large peak values at the beginning and decays substantially after a few tenths of a second, but its full decay occurs only after several seconds. Previous studies have shown the harmonics components contained in the inrush currents [69]. Because of its dominance, the second harmonic has been utilized by most conventional relays to block the trip signal triggered by inrush current. By incorporating a harmonic constraint of the input signal over time, the second harmonic is then used as the characteristic component of the asymmetrical magnetization peculiar to the inrush. Gap detection is another widely used method [70]. The principle of gap detection is by measuring the intermittent angle in the waveform, which is a dominant and essential feature of the inrush current, to discriminate the inrush and internal fault condition. Alternatively there are also applications utilizing Wavelet transform, [71] frequency transient detection [72] and artificial neural network [73] [74].

However, security problems may arise with the extension of EHV transmission lines, increment of SVC capacity and improvement of silicon steel techniques. The minimum content of the second harmonic depends mainly on the knee-point of the magnetizing characteristic of the core. The lower the saturation flux density, the higher the amount of the second harmonic. Modern transformers built with improved magnetic materials have high knee-points, and therefore, their inrush currents display a comparatively low amount of the second harmonic which could be only 7% [75]. In contrary to this, in high voltage power systems with series capacitor compensation, the second harmonic content of fault current may be more than 15% [76]. Since the second harmonic is the only restraining criterion for stabilizing differential relays during inrush conditions, certain difficulties arise when protecting such modern transformers.

The successful application of the gap detection based method is subject to the assumption on the existence of an explicit gap, in every cycle, in which the shape of the gap is both flat and close to zero no less than 1/4 of a cycle. However, the CTs may saturate during inrush conditions, which is very likely due to the DC component in the current. In such conditions, the distorted waveform within the gaps may result in a false tripping. Moreover, during severe internal faults, when the CTs saturate, their secondary currents may also show periods of low and flat values resulting the relay missing operations. Therefore, the gap principle has been limited to the application of differential protection.

Research on improving the performance of the harmonics constraint based inrush current identification algorithms continues. However, most of these studies are either based on the transformer equivalent circuit model or require some transformer data, and this may become susceptible to parameter variations. Compared to traditional Fourier transform based harmonics analysis in frequency domain, the MMTH scheme can localize features in both time and frequency domains. By MMTH decomposing the signal, the asymmetrical features of the inrush waveform are exposed, where as other irrelevant components are attenuated. With a set of simple criteria, a much better signal characterization and a more reliable discrimination can be obtained.

5.2 The Basic Principles of Magnetizing Inrush Current

5.2.1 Introduction to magnetizing inrush current

It is well-known that the differential protection is undoubtedly important for the main power system equipment. It has the properties of flexibility and selectivity and been successfully applied for protection of generators, reactors, motors, busbars and transformers, etc. The scheme of differential protection system depends entirely on the Kirchoff principle that the sum of the currents flowing into a conducting network is zero. However, with respect to the transformer protection relay, the protected object includes not only electric circuits but magnetic circuits as shown in Fig. 5.1. and its mathematical expression is shown as equation (5.2.1). Therefore the unbalance current is introduced because of the existence of magnetizing current [77].

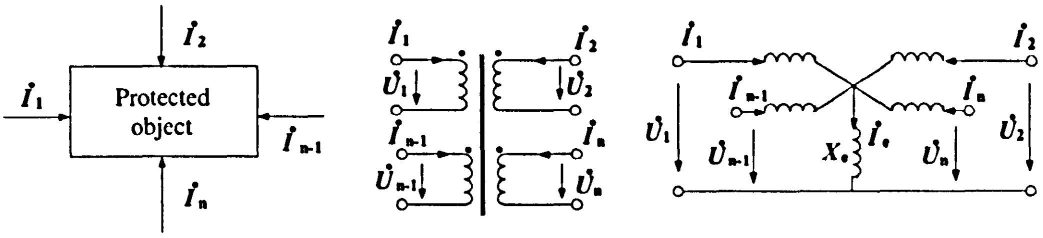

Fig. 5.1: The n windings transformer and its equivalent circuit.

$$\sum_{i=1}^{n} \dot{I}_i = I_e \neq 0, \qquad (5.2.1)$$

where $\dot{I}_i$ is the nth current of protected object, I_e is magnetizing current.

in the normal operation condition, $I_e < 1\% I_m$ (I_m is the rated current of the transformer), does not affect the performance of transformer differential protection. When an external fault occurs, the voltage drops sharply, I_e is much smaller and it is always omitted. But when the flux Φ in transformer air-core is close to the saturation flux Φ_S as shown in Fig. 5.2, along with the magnetizing impedance X_e sharply decreasing, the magnetizing current I_e will rise to a very high value. Especially, when the transformer switches in the no-load condition, the I_e may exceed I_{th} by 10 times. In this case, the "magnetizing inrush current" presents. With such a high unbalanced current, it is difficult to avoid maloperation of differential protection.

The unbalanced current can be caused in two cases: steady state and transient state. In the steady state case, it may be caused due to transformer tap change variation and CT mismatch, which can be overcome by setting the restraint current. In the transient state case, the magnetizing inrush current is most adverse, which is also further distorted by CT's saturation. The transformer differential protection has been suffering from the problem of magnetizing inrush current all the time. Up to now, the major challenge of designing transformer differential protection is how to identify the magnetizing inrush current.

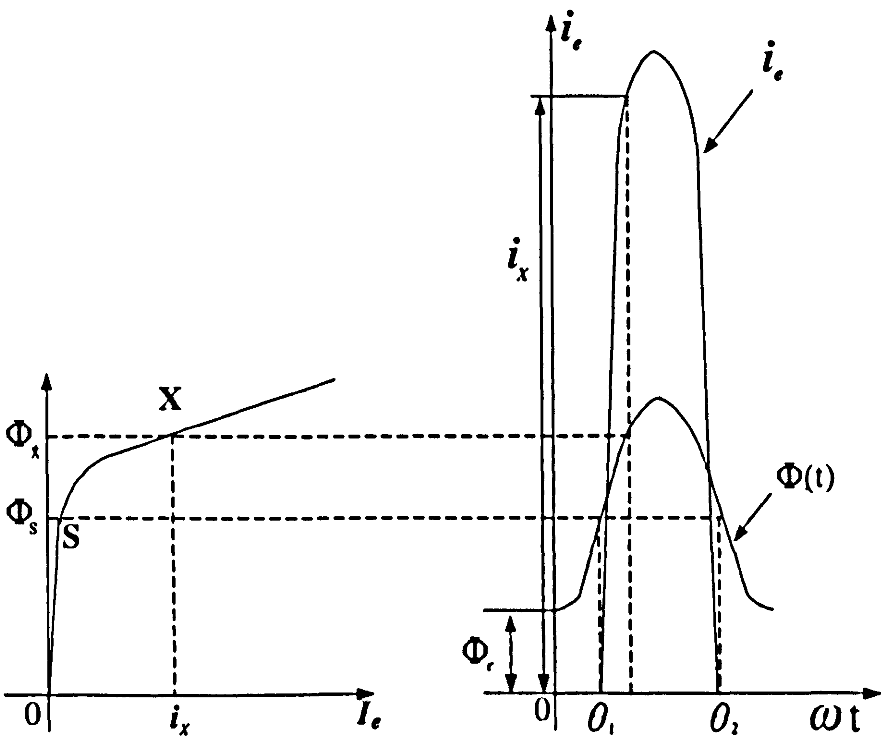

Fig. 5.2: magnetizing characteristic

In order to illustrate the magnetizing inrush current clearly, the slope of saturation curve SX in the magnetizing characteristic as shown in Fig. 5.2 is somewhat exaggerated. In fact, it is much more even. It is assumed that saturation curve SX is linear, which crosses with vertical axis at S. Therefore, Φ_S is defined as saturation flux. When $\Phi < \Phi_S$, $i_e \approx 0$, whereas when $\Phi > \Phi_S$, i_e is sharply increasing in directly proportion to Φ corresponding to the extreme saturation. Therefore i_e and Φ_S have a same shape of waveforms.

It is assumed that the transformer switches on at the zero point of the voltage waveform, where the supply voltage is $u = V_m \sin(\omega t + \alpha)$ and inception angles $\alpha = 0$. Noting $\alpha = d\Phi(t)/dt$, the steady flux $\Phi(t)$ in air-core is derived as:

$$\Phi(t) = -\Phi_m \cos(\omega t + \alpha) + \Phi_m \cos(\alpha) + \Phi_r, \tag{5.2.2}$$

where Φ_r is the residual flux left in air-core from last de-energizing of transformer, Φ_m is the magnitude of the steady flux, $\Phi_m = U_m/\omega$. At the instant of switching, $t = 0$, the flux can be derived as:

$$\Phi(0) = -\Phi_m \cos(\alpha) + \Phi_m \cos(\alpha) + \Phi_r = \Phi_r. \tag{5.2.3}$$

The above equation shows that the flux in air-core keeps unchanged at the beginning of switching, which equals the residual flux Φ_r. The derivation agrees with the physical concept of transformer.

In equation (5.2.2), $-\Phi_m \cos(\omega t+\alpha)$ is the steady (compulsory) flux, $\Phi_m \cos(\alpha)$ is the transient flux which is caused in order to keep flux unchanged at $t = 0$ and Φ_r is the residual flux.

With reference to the magnetizing characteristic curve as shown in Fig. 5.2, the magnetizing inrush current $i_e(t)$ can be obtained from $\Phi(t)$. Because voltage $u(t)$ is sinusoidal and the saturation curve SX is assumed to be linear, $\Phi(t)$ and $i_e(t)$ are also sinusoidal. Furthermore, because $\Phi < \Phi_s$, $i_e \approx 0$, as shown in Fig. 5.2, where $i_e \approx 0$ within two sections of the waveform if $i_e(t)$: $\omega t = 0 \sim \theta_1$ and $\omega t = \theta_2 \sim 2\pi$. This means that there exist breaks in the waveform of $i_e(t)$ within one cycle. The angle gap, resulted from the waveform breaks, is denoted by θ_g, which is expressed as:

$$\theta_g = \theta_1 + (2\pi - \theta_2). \tag{5.2.4}$$

From Fig. 5.2, it can be seen that the value of gap θ_g is related to the following factors:

1. The amplitude of source voltage U_m or the amplitude of steady flux Φ_m.

2. The residual flux Φ_r.

3. The saturation flux Φ_s.

4. The inception angle α of transformer switching.

When $\alpha = 0$, the steady flux is $-\Phi_m$, the transient flux is $+\Phi_m$, and residual flux is $+0.8\Phi_m$. In this case, the maximum flux can be obtained at the time instant where $\omega t = \pi$.

$$\Phi(\pi) = 2\Phi_m + 0.8\Phi_m = 2.8\Phi_m$$

in the same condition, if $\Phi_s = 1.4\Phi_m$, the minimum gap and the 2nd-order harmonics (fundamental component is 100% can be obtained respectively as follows [77]:

$$\theta_{g\,\mathrm{min}} = 120^\circ \qquad \text{and} \qquad I_{2\,\mathrm{min}} = 17.1\%.$$

5.2.2 Magnetizing inrush current with CT saturation

The signal waveform of the magnetizing inrush current will be further distorted by the built-in instrumental current transducer (CT) of the transformer protection relay. Particularly to the most adverse conditions, the gap will disappear. This phenomenon caused by the CT saturation raises more difficulties for identification of magnetizing inrush current.

For simplicity of analysis, the magnetizing characteristic of transformer, as shown in Fig. 5.2, is represented as two linear segments, i.e. SX and OS. Considering the most serious condition, small impedance of power supply and feeder is assumed. This implies that the transformer switches into a power system with the infinite power supply. The magnetizing inrush current, I_p, which flows into the CT primary winding, can be expressed as: $i_p = 0$, when non-saturation in the transformer air core and

$$i_p = \frac{V_m}{X_l'}[\cos(\alpha) - \cos(\omega t + \alpha) - \frac{\Phi_s - \Phi_r}{\Phi_m}], \tag{5.2.5}$$

when saturation in the transformer air core. In equation (5.2.5), X_l' is the saturated reactance of air core. Fig. 5.3 shows the magnetizing inrush current waveform flowing into CT primary winding. In Fig. 5.3, between t_1 and t_2, the transformer air core is saturated, the magnetizing inrush current is produced.

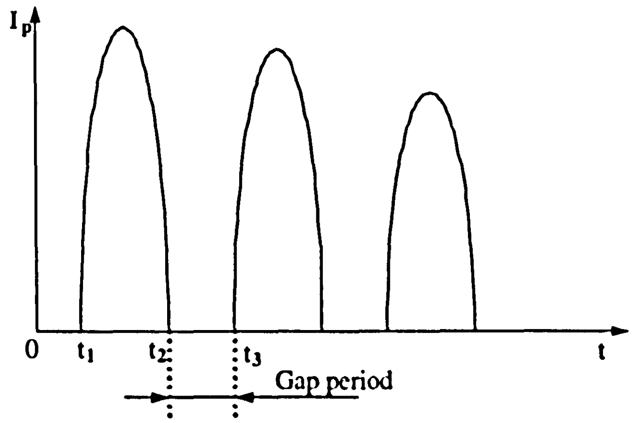

Fig. 5.3: The waveform of magnetizing inrush current flowing into CT primary winding.

Between t_2 and t_3, the air core is non-saturated, the magnetizing current is nearly zero. This section represents the gap of the waveform.

Because the current signals used by the protection relay are obtained from the secondary side of CT, the influence of CT saturation must be taken into account. In order to obtain the basic characteristics of CT saturation, the CT is simplified as an equivalent circuit consisting of the magnetizing reactance L_μ and the secondary load resistance R_2, as shown in Fig. 5.4, where i_1, i_2 and i_μ represent as the primary, secondary and magnetizing current respectively.

With reference to equation (5.2.5), the secondary current of CT i_2 can be expressed as [78]:

$$i_2 = I_{p\max}[A - \frac{\cos\omega t + \omega T_2 \sin(\omega t)}{1 + (\omega T_2)^2}] + Ce^{-t/T_2}, \tag{5.2.6}$$

where

$$\begin{aligned} I_{p\max} &= \frac{V_m}{X_l'}; \\ A &= \cos(\alpha) - \frac{\Phi_s - \Phi_r}{\Phi_m}; \\ T_2 &= \frac{L_\mu}{R_2}; \end{aligned}$$

and C is a constant.

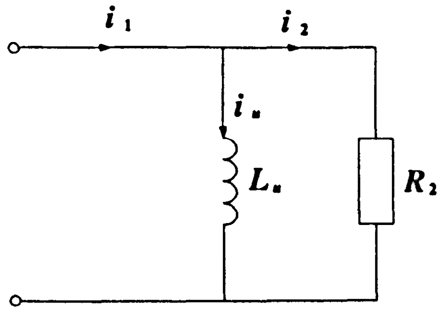

Fig. 5.4: The equivalent circuit diagram of CT.

As shown in Fig. 5.3, between t_1 and t_2, when the magnetizing inrush current i_p flows into the CT primary winding, the magnetizing flux is formed within CT (storing energy), which makes the CT saturated; L_μ is dramatically decreasing to the saturated reactance, $i_\mu \neq 0$ at the time instant t_2. Between t_2 and t_3, $i_\mu \approx 0$, i_μ is circulated through the secondary load resistance R_2 decaying at the time instant T_2. Therefore, the voltage in opposite direction is produced across R_2. When $t = t_3$, $i_\mu \neq 0$, the decaying procedure is over. The value of i_μ at the time instants t_2 and t_3 can be determined as:

$$\begin{aligned} i_\mu|_{t=t_2} &= D; \\ i_\mu|_{t=t_3} &= B; \end{aligned}$$

where

$$\begin{aligned} B &= \frac{I_{p\max}\sin(\delta)}{1-e^{-2\pi/\omega T_2}}[\sin(\omega t_1+\delta)+\sin(\omega t_1-\delta)e^{-2(\pi-\omega t_1)/\omega T_2}]e^{-2t_1/T_2}; \\ C &= Be^{t_1/T_2}+I_{p\max}\sin(\delta)\sin(\omega t_1-\delta)e^{t_1/T_2}; \\ D &= Be^{2t_1/T_2}; \\ \delta &= \arctan(\omega T_2); \end{aligned}$$

With CT saturated, the current flowing in the CT secondary winding is shown in Fig. 5.5. Obviously, the gap disappears and the opposite peak value D, which is also related to the stored energy, is dependent on the amplitude of the magnetizing inrush current, the CT saturated reactance L_μ and the secondary load resistance R_2.

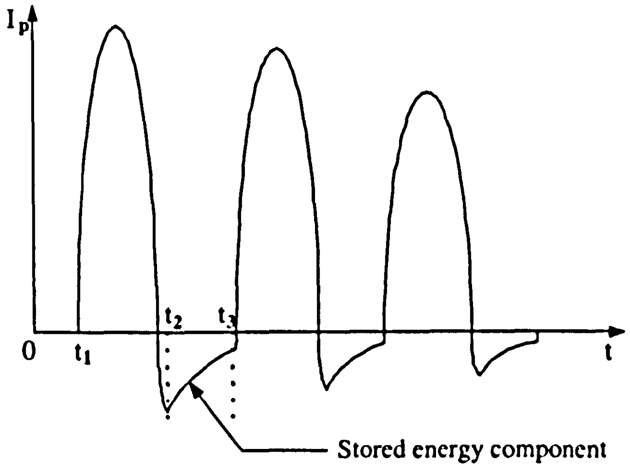

Fig. 5.5: The waveform of magnetizing inrush current flowing in the CT secondary winding with CT saturation

5.2.3 The existing methods and problems of identifying magnetizing inrush current

With the understanding of magnetizing inrush waveform, there have been a couple of inrush-identification schemes. For example, the methods developed based on the principles of fast saturation of non-periodic component, 2nd or even-order harmonic and gap are more commonly used. Whereas, it is shown in [77] that in the modern power systems, due to extension of EHV transmission lines, increment of SVC capacity and improvement of silicon steel techniques and magnetizing characteristic, the content of the 2nd-order harmonic consisted in magnetizing inrush current is no more than 7% of the fundamental frequency component in the some operating conditions of large capacity transformers. Moreover the content of the 2nd-order harmonic involved in fault current is more that 15% in the situation of high voltage transmission lines with series capacitor compensation. Therefore, this will bring up a challenge to the

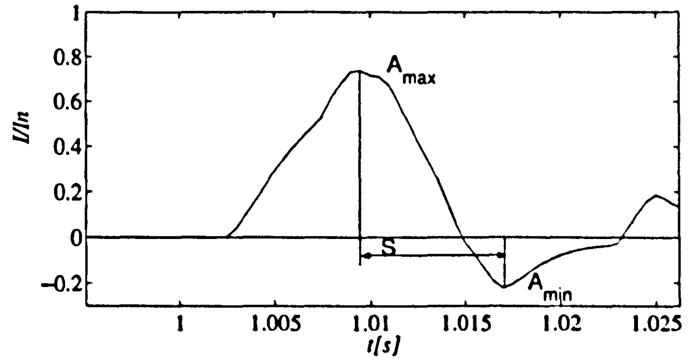

Fig. 5.6: A typical inrush current waveform

approaches to identifying magnetizing inrush using the 2nd-order harmonics. The gap is a characteristic of the waveform of magnetizing inrush current and the gap identification is based on accurate measurement of intermittent angle of inrush waveform. However, due to the effect of CT's saturation, this principle has the limit in the application in differential protection of transformers. MMTH brings a new way to solve this problem

5.3 Identification of Inrush Current using MMTH

Consider a typical cycle of the inrush current, as illustrated in Fig. 5.6, where the 50Hz current signal I is normalized as I/In. It is clear that the asymmetries of the waveform exhibit in both amplitude and duration of the positive and negative segments. If the signal is decomposed to have the peak around A_{max} and the valley around A_{min} separated from other components, both with a given length of flat base, then the difference in the amplitude of A_{max} and A_{min}, as well as the interval, S, between them, as shown in Fig. 5.6, can be quantified and compared with those in the internal fault current and normal power system operation conditions.

Compared with the inrush current, the waveform of internal fault current, as shown in Fig. 5.7, is a regular periodical signal with an exponentially decaying DC offset. If the effect of DC offset is removed, the waveform becomes a

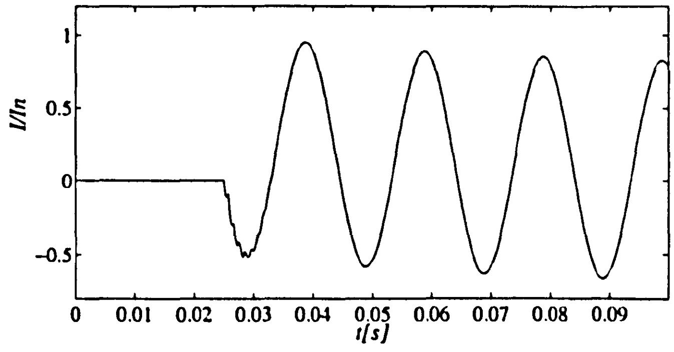

(a) Internal fault current waveform

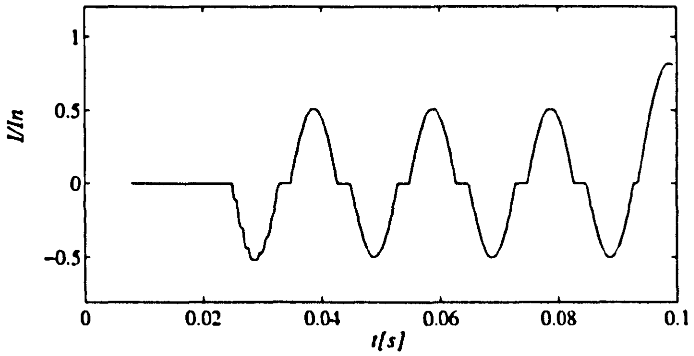

(b) Quadratic MMTH output of internal fault with the BSE is 9ms.

Fig. 5.7: Internal fault current and its quadratic MMTH output

normal sinusoid. When the same decomposition as above mentioned applied, the extracted peaks and valleys should have similar amplitudes, with intervals approximately equal to half of the power system cycle.

To perform such decomposition for extracting the peaks and valleys of the transformer current signals, the MMTH scheme is applied as illustrated in Fig. 5.8.

The input current waveform is firstly transformed to obtain two signal f and f', defined as

$$\begin{aligned} f &= I + I_0 \\ f' &= -I + I_0, \end{aligned}$$

where I_0 is a pre-determined constant. I_0 is necessary since the MMTH scheme

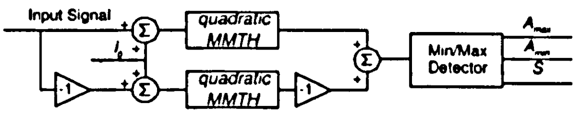

Fig. 5.8: Block diagram of the proposed method

requires the input signal f satisfies $(f \ominus G_j)(t) \geq 0$, where $j = 0, 1, \cdots$ and G_0 is the BSE. The value of I_0 is not important as long as it results in both f and f' being positive. Since the current signal contains both peaks and valleys, due to the erosion operation in the decomposition procedure can only extract peaks of a signal, the inverted input signal, f' is decomposed separately and then inverted again to obtain the valleys of the signal. The BSE involved for decomposition is a simple zero-valued flat line with 9ms length, with its origin at the center.

When the signal is decomposed to the given level, simple criteria can be employed to quantify the asymmetry in a signal, as follows:

$$\begin{aligned} \delta_I &= \frac{|A_{\max} - |A_{\min}||}{A_{\max} + |A_{\min}|} \\ \delta_t &= \frac{|S - 0.01|}{0.01}. \end{aligned}$$

where δ_I represents the amplitude asymmetry between the extracted peaks and valleys, where as δ_t is the peak-to-valley interval asymmetry normalized by half of the power system cycle, which is 0.01 second in case of 50Hz. The higher δ_I and δ_t are, the stronger asymmetry exist in the signal. Therefore, if both δ_I and δ_t exceed a predefined threshold, an inrush current can be identified. Based on our practical experiment, we use 10% and 20% as the threshold for δ_I and δ_t, respectively.

5.4 Results and Discussion

The proposed algorithm was tested with PSCAD simulated internal fault current shown in Fig. 5.7, as well as inrush signals, as shown in Fig. 5.9 and

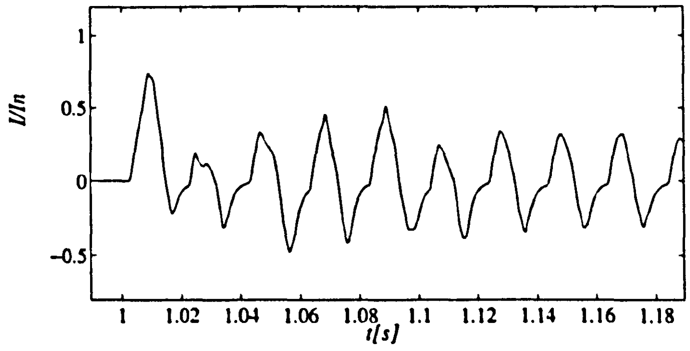

(a) Inrush signal 1

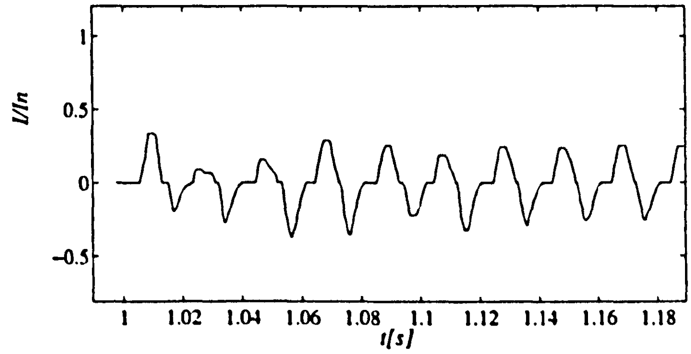

(b) Quadratic MMTH output of inrush with the BSE is $9ms$.

Fig. 5.9: Inrush signal 1 and its quadratic MMTH output

Fig. 5.10. The inrush signals, both with their second harmonic contents less than 10% and the effect of CT saturation, were measured from a physically simulated power system laboratory. As illustrated in the waveforms, only the peaks and valleys of the original signal with 8ms intervals exist in the output signal, in which the singularities of the inrush current are clearly enhanced; where as shown in Fig. 5.7(b), the quadratic MMTH output of Fig. 5.7(a) remains fairly symmetrical.

Fig. 5.11 and Fig. 5.12 present the cycle by cycle evaluation of the waveform asymmetries for the quadratic MMTH output of signals. It is clear that in the first cycle, both δ_l and δ_t of the fault current are far below the 10% threshold, where as for the fault currents, they are mostly well above 20% and may be as

Table 5.1: δ_I of the inrush and internal fault currents

Signal	1st period	2nd period	3rd period
inrush1	27%	50.51%	41.1%
inrush2	73.11%	48.38%	4.19%
internal fault	4.05%	0.2%	1.17%

high as 73%.

One may notice that in certain cycle, as the the δ_I of inrush 2 at the third cycle listed in Table 5.1, is only 4.19%. However, since the identification of inrush current is solely by means of the asymmetry exhibits in the first cycle, such value should not cause any problem.

For off-line simulations where computation time is not critical, the structuring element may be adjusted, or adaptive to achieve a better accuracy at the expense of computing time. For real-time implementation, in case of an inrush occurs at zero phase, the 9ms length BSE is applied and 2nd level is chosen as output, the identification requires one power system cycle for obtaining the A_{max} and A_{min}, plus 6ms for the operations involved in MMTH for decomposition.

5.5 Conclusion

This chapter describes our works on applying morphological filtering techniques to power system protection relays, to identify inrush current with consideration of the CT saturation condition. The work described in this chapter was undertaken in collaboration with colleagues [33]. The technique is fundamentally different from the conventional methods, as it decomposes the signal based on time domain features instead of in the frequency domain. Since it works directly upon the geometric characteristics of the input, there is no need for abstract transform techniques such as Fourier, Laplace, and Hilbert transforms, nor is there a requirement for transform-world concepts such as frequency, convolution, effective bandwidth and ripple.

As shown by the results obtained, the advantages of the proposed scheme are:

- Reliable identification of inrush in cases when inrush current contains less than 10% of the second harmonic component.
- Reliable operation of protection when the CTs saturate.
- Reduced computational complexity by using nonlinear morphological operations with only addition/subtraction and finding local maxima/minima in calculation [44], which is much less than the harmonics based methods.
- The classification scheme is an simple yet effective way of assigning an observed signal to a particular group.
- it provides flexibility in the choice of structuring function which can be adjusted by modifying its shape.

Further improvement on the identification performance may be achieved by optimizing the structuring function to obtain a more effective decomposition. Nevertheless, as in-depth analytical and experimental studies on this MM based waveform identification method are being carried out, the efficiency of the proposed method will be fully appreciated after it has been extensively applied and verified in more comprehensive circumstances.

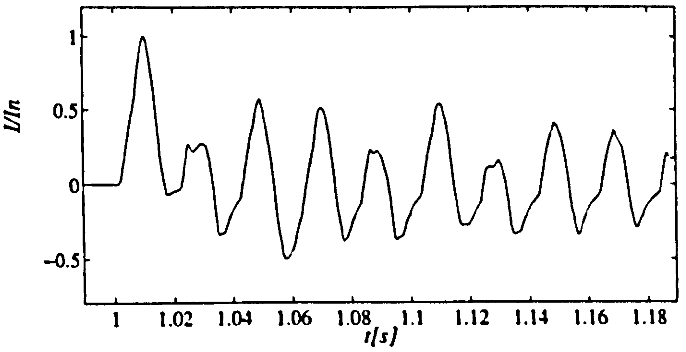

(a) Inrush signal 2

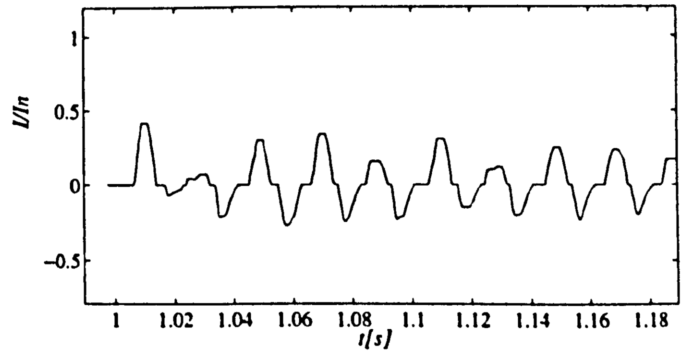

(b) Quadratic MMTH output of inrush with the BSE is $9ms$.

Fig. 5.10: Inrush signal 2 and its quadratic MMTH output

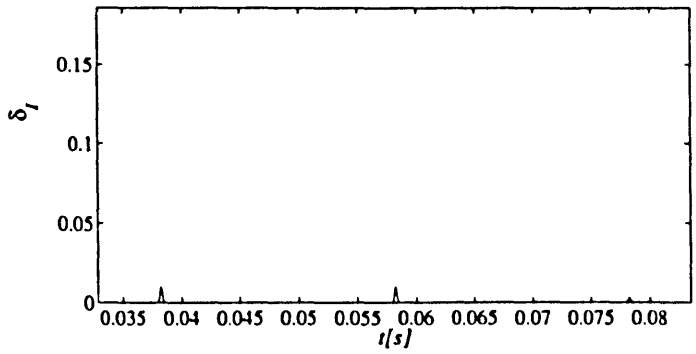

(a) Internal fault

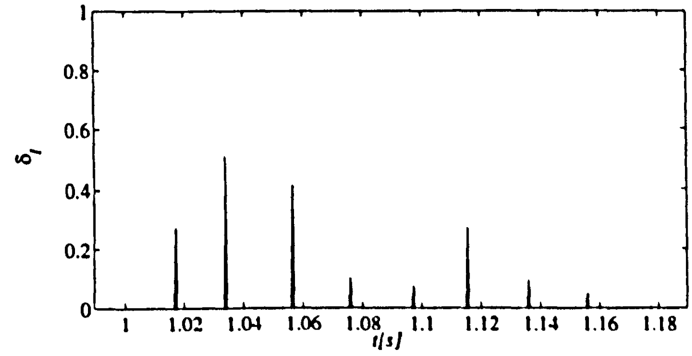

(b) Inrush 1

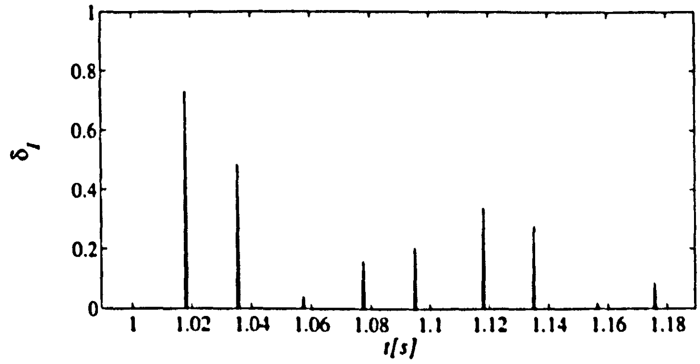

(c) Inrush 2

Fig. 5.11: The asymmetries on peak and valley amplitudes

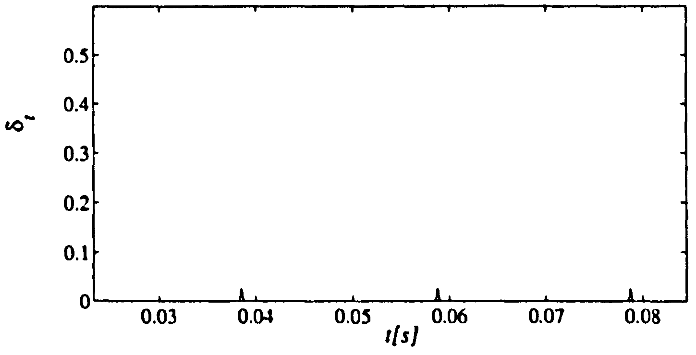

(a) Internal fault

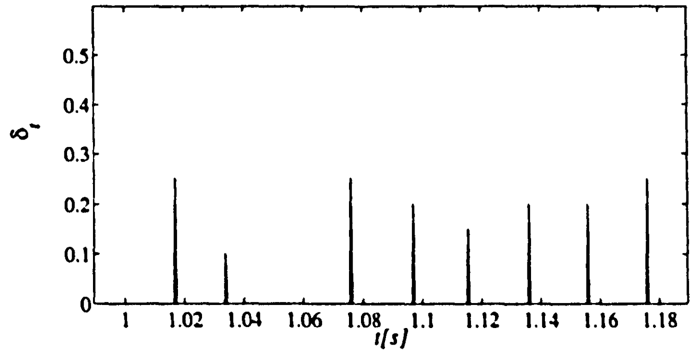

(b) Inrush 1

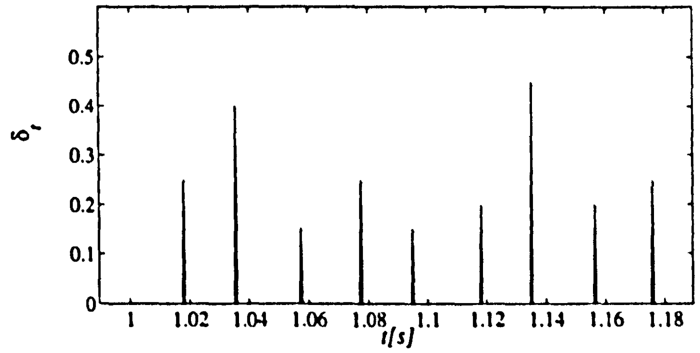

(c) Inrush 2

Fig. 5.12: The asymmetries on peak-to-valley intervals

Chapter 6

Applying Multi-resolution Morphological Gradient in Ultra-High-Speed Directional Protective Relaying

6.1 Introduction

The method of ultra-high-speed fault clearance has been recognized for a long time as an effective way of improving transient stability of power systems. A considerable amount of effect has been dedicated to its research, especially during the 1970s and 80s. Great contributions ascribed to the development and establishment of travelling wave based protection techniques have been made, which include various basic principles, field tests and implementations [79][80]. Compared with the conventional protection techniques developed based on measurements of fundamental components, this technique has the advantages of fast response and immunity to the influences caused by power swing, CT saturation and series compensation capacitor. In the recent years, the transient based protection technique has been drawing growing attention as it fully utilizes the fault-generated high frequency wave components to generate fast relaying signals. This technique instinctively leads to overcoming a drawback caused at a low inception fault angle [81],[82]. Fundamentally, both the techniques are developed upon the relationship between transient current, voltage, time and distance, which is fully described by the travelling wave equations [83]. Therefore, they essentially rely on exactly extracting the characteristics of the transient components that comprise superimposed quantities and noises generated by a fault and its concomitant arcing respectively. However, the application of these ultra-high-speed protection techniques suffers relatively low reliability and feasibility by its limitations such as lack of effective signal processing tools. The advent of the Wavelet Transform (WT) method, which possesses capabilities of both time and frequency domain localizations, gives a great impetus to investigating the possibility of improving ultra-high-speed protection.

The basic principle of power system relay design and operation has not been changed for more than half a century, even after the microprocessor-based relay was introduced in the early 1980s. Almost all the algorithms of protection relays are based on the sinusoidal signals and sequence components that have been familiar to power system engineers. For any distortion of the voltage or current signals, which are caused by the system disturbances, unbalanced operation and influence of power electronics devices, harmonics analysis is applied. The concept of harmonics stems from the mathematical integral transform, such as Fourier Transform and Wavelet analysis. However, this transform is calculated using the sampling data of the signal which covers a certain period of time to reveal the periodic characteristics of the signal. Therefore, the extraction of the main components has to be accomplished based on a reasonable data window of waveforms of voltage and current. If harmonics need to be considered during the transient process or in the circumstance of waveform distortion, faster sampling is required to ensure the accuracy of the extracted information. Obviously the integral transform based schemes are difficult to be applied for ultra-high-speed protection which requires a fast action, based on the transient features of fault voltage and current.

In contrast with Fourier transform and Wavelet analysis, Mathematical Morphology (MM) is developed from set theory and integral geometry [4], and is concerned with the shape of a signal waveform in the complete time domain rather than the domain frequency. MM is a nonlinear approach [5] and has been widely used in the areas of image processing, machine vision and pattern recognition, due to its robustness in preserving the shape while suppressing noise [44],[84]. The mathematical calculation involved in MM includes only addition, substraction, maximum and minimum operations without any multiplication and division. When acting upon complex shapes of signal, MM operations are capable of decomposing a signal into meaningful parts and separating them from the background, as well as preserving the main shape characteristics. The application of the MM technique to power system protection problems has been attempted for identification of transformer inrush current [33].

In this chapter, the MM technique is applied for design of an ultra-high-speed directional protection relay. Firstly, a process of deriving the direction discriminants of a fault taking place on transmission lines is given, based on travelling wave analysis. Then a Multi-resolution Morphological Gradient (MMG) method is presented to extract the transient features directly from fault-generated transient signals. Finally a typical $400kV$ EHV transmission model is set up to verify the proposed ultra-high-speed directional protection scheme under various fault conditions, in comparison with the WT method.

6.2 Principle of Ultra-high-speed Directional Relaying

The basic principle of the proposed directional protection scheme is addressed with reference to a 400kV transmission lines system as shown in Fig. 6.1. A directional protection relay is situated at the end of section P near busbar S. The forward direction is defined at the relaying point as current flowing from busbar S into the protected section P.

The relaying signals adopted in this scheme, initially introduced in [81],[85],

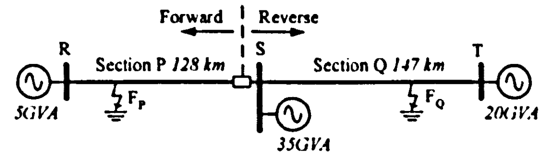

Fig. 6.1: Single-line diagram of 400kV power transmission lines system.

are given as:

$$S_{1S} = \Delta v_S(t) - R_0 \Delta i_S(t), \tag{6.2.1}$$

$$S_{2S} = \Delta v_S(t) + R_0 \Delta i_S(t), \tag{6.2.2}$$

where R_0 is a surge replica resistance and its value is arranged as to match a line surge impedance Z_0 closely. $\Delta v_S(t)$ and $\Delta i_S(t)$ observed at the relaying point S are the transient voltage and current signals generated by the fault. In order to explicitly illustrate the proposed directional discrimination to fault, the transient relaying signals are derived in detail as follows.

6.2.1 Fault in forward direction

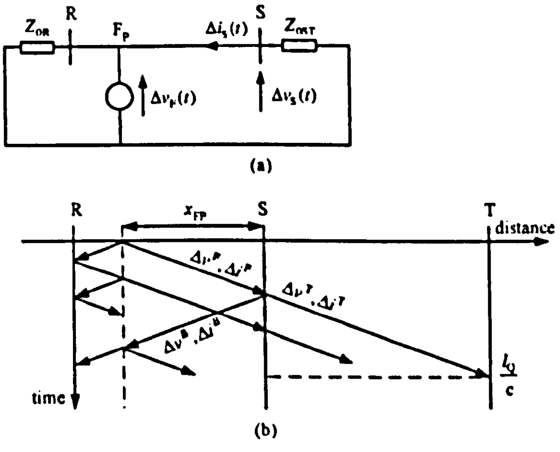

Fig. 6.2: Equivalent superimposed circuit under a fault in forward direction (a) and its Bewley-lattice diagram (b).

Figure 6.2 depicts an equivalent superimposed circuit with a fault occurring in forward direction at a distance of x_{FP} from busbar S and with the propagation of the fault-generated transient waves along a single-phase lossless transmission line. The superimposed voltage $\Delta v_{\mathrm{FP}}(t)$ and associated current $-\Delta i_{\mathrm{FP}}(t)/Z_{0\mathrm{P}}$ at the fault point $\mathrm{F_P}$, caused by the injection of an equivalent fictitious source, travel at a speed c towards the line terminals. The transient relaying signals observed at the relaying point can be derived by applying the travelling wave equations, described in [81],[83], as follows:

$$\begin{aligned}\Delta v_{\mathrm{S}}(t) &= \Delta v_{\mathrm{S}}^{\mathrm{F}}(t) + \Delta v_{\mathrm{S}}^{\mathrm{B}}(t) \\ &= \Delta v_{\mathrm{FP}}(t - x_{\mathrm{FP}}/c) + K_{\mathrm{R}}^{\mathrm{F}}\Delta v_{\mathrm{FP}}(t - x_{\mathrm{FP}}/c) \\ &= (1 + K_{\mathrm{R}}^{\mathrm{F}})\Delta v_{\mathrm{FP}}(t - x_{\mathrm{FP}}/c), \qquad (6.2.3)\end{aligned}$$

$$\begin{aligned}\Delta i_{\mathrm{S}}(t) &= (-\Delta v_{\mathrm{S}}^{\mathrm{F}}(t) + \Delta v_{\mathrm{S}}^{\mathrm{B}}(t))/Z_{0\mathrm{P}} \\ &= (-1 + K_{\mathrm{R}}^{\mathrm{F}})\Delta v_{\mathrm{FP}}(t - x_{\mathrm{FP}}/c)/Z_{0\mathrm{P}}, \qquad (6.2.4)\end{aligned}$$

$$\begin{aligned}S_{1\mathrm{S}} &= 2\Delta v_{\mathrm{FP}}(t - x_{\mathrm{FP}}/c), \qquad (6.2.5) \\ S_{2\mathrm{S}} &= 2K_{\mathrm{R}}^{\mathrm{F}}\Delta v_{\mathrm{FP}}(t - x_{\mathrm{FP}}/c), \qquad (6.2.6)\end{aligned}$$

where the superscripts F, B and T indicate a incident (forward), a reflected (backward) and a transmitted wave respectively, $Z_{0\mathrm{P}}$ is the line surge impedance of section P. In this case, the refection coefficient $K_{\mathrm{R}}^{\mathrm{F}} = (Z_{0\mathrm{ST}} - Z_{0\mathrm{P}})/(Z_{0\mathrm{ST}} + Z_{0\mathrm{P}})$, where the $Z_{0\mathrm{ST}}$ is the equivalent surge impedance viewed from point S outwards.

6.2.2 Fault in reverse direction

For a fault occurring at point $\mathrm{F_Q}$ in a distance of x_{FQ} from busbar S on section Q in reverse direction as indicated in Fig. 6.3, only the transmitted transient waves can be observed at the relaying point and their travelling direction is forward. The relaying signals are derived similarly as follows:

$$\Delta v_{\mathrm{S}}(t) = \Delta v_{\mathrm{S}}^{\mathrm{T}}(t)$$

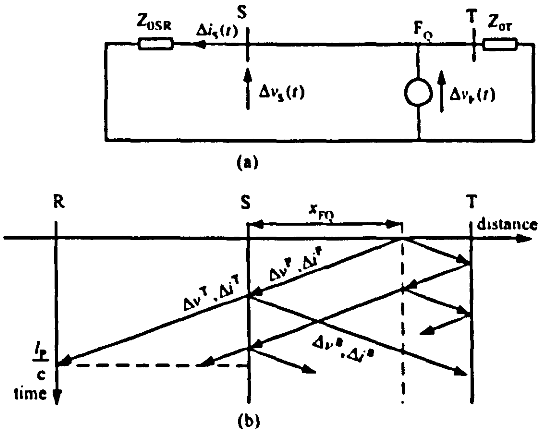

Fig. 6.3: Equivalent superimposed circuit under a fault in reverse direction (a) and its Bewley-lattice diagram (b).

$$= K_T^B \Delta v_{FQ}(t - x_{FQ}/c), \tag{6.2.7}$$

$$\begin{aligned} \Delta i_S(t) &= \Delta v_S^T(t)/Z_{0Q} \\ &= K_T^B \Delta v_{FQ}(t - x_{FQ}/c)/Z_{0Q}, \end{aligned} \tag{6.2.8}$$

$$S_{1S} = 0, \tag{6.2.9}$$

$$S_{2S} = 2K_T^B \Delta v_{FQ}(t - x_{FQ}/c), \tag{6.2.10}$$

where the refraction coefficient $K_T^B = 2Z_{0SR}/(Z_{0SR} + Z_{0Q})$, similarly Z_{0Q} is the line surge impedance of section Q and Z_{0SR} is the equivalent terminating surge impedance.

From the foregoing analysis, the following summarization can be given:

- The direction discriminability to a fault with reference to the relaying point can be determined by comparing the magnitudes of the transient relaying signals S_{1S} and S_{2S}.
- Equations (6.2.5) and (6.2.6) representing the relaying signals for a forward fault and (6.2.9) and (6.2.10) for a reverse fault will be satisfied for a period which is twice that of the line transit time, until arrival of

a transient wave reflected from the adjacent point of discontinuities, i.e. $2l_{\mathrm{P}}/c$ or $2l_{\mathrm{Q}}/c$. They are indicated in Figs. 6.2 and 6.3, where l_{P} and l_{Q} are line lengthes of section P and Q respectively.

- Taking the stray capacitance of the busbar into account, in practice, the terminating equivalent surge impedance is not equal to the line surge impedance [86], i.e. $K_{\mathrm{R}}^{\mathrm{F}} \neq 0$ and $K_{\mathrm{T}}^{\mathrm{B}} \neq 0$.
- With extension to 3-phase transmission system, the phase variations of currents and voltages are decomposed into modal components using the Clack modal transformation [79]. An aerial mode is utilized in this scheme.

6.3 Simulation Study and Results Analysis

The PSCAD/EMTDC is employed to simulate a power transmission system based on a frequency-dependant transmission line model [87]. All parameters are given with reference to a 400kV EHV vertical constructed line [88], which is typically used in the UK SupreGrid system as indicated in Fig. 6.1. The proposed directional relay is installed on section P near busbar S to protect line section P. When a fault is detected in forward direction, a tripping signal will be issued via a communication channel, otherwise, a blocking signal will be issued instead within a preset confirmation time period started from the first detected transient wavefront.

A variety of fault scenarios have been simulated to evaluate the validity of the proposed directional protection scheme. The input signals were processed using the quadratic MMG based on the sampling rate 1MHz and a $8\mu s$ shifting data window. The observed voltage and current signals at busbar S are firstly transformed into aerial mode (mode 2) current and voltage signals. The replica surge impedance is taken as the real part of the actual aerial mode surge impedance $R_0 = 253.76\Omega$, which has been derived from the transmission line parameters in this case. The aerial mode current and voltage signals are then processed by the technique of quadratic MMG (level $a = 2$) with 8 sampling points length of a flat line SE ($L_Q = 8$). Finally, the quadratic MMG of the aerial mode signals, presenting the transient features, ρ_v^2 and ρ_i^2, are used, substituting Δv_S and Δi_S in (6.2.1) and (6.2.2), to determine the directional protection relaying.

6.3.1 A solid fault in forward direction

Under the condition of a solid phase-A-earth fault with nearly 90° of fault inception angle in a distance of 48km from busbar S on section P, the aerial mode current and voltage, i_{S2} and v_{S2}, as well as their associated quadratic MMGs, ρ_i^2 and ρ_v^2, are shown in Figs. 6.4(a) and 6.4(b) respectively. It is noted that the distinct characteristics of transient components of faulted current and voltage signals are well presented with their locations and polarities by the quadratic MMGs, whereas the steady state components are depressed sufficiently. Examining the relaying signals S_{1S} and S_{2S} in Fig. 6.4(c), it can be concluded that firstly there is a fault occurring somewhere along transmission system with confirmation of spikes representing transient disturbances; secondly a forward direction to fault is determined and a tripping signal is issued as $S_{1S} \neq 0$ and $S_{2S} \neq 0$.

6.3.2 A high-resistance earth fault in forward direction

In the same fault condition, as described previously except raising the fault path resistance to 200Ω, the quadratic MMGs of faulted aerial mode current and voltage and the relaying signals are shown in Fig. 6.5. The results indicate that the magnitudes of quadratic MMG are diminished as the increase of fault path resistance, however, the transient features presented by quadratic MMG still remain sufficient.

6.3.3 A fault with low inception angle in reverse direction

Figures 6.6(a) and 6.6(b) illustrate the quadratic MMGs of the transient aerial mode current and voltage at busbar S to a phase-A-earth fault with fault inception angle 0° in a distance of 47km from busbar S on section Q. While the magnitudes and rates of the transient wave travelling away from the fault point reduce as the point on voltage wave approaches a zero crossing, the high-frequency transient signals generated by fault arcing are still attainable to be detected [89],[90]. As a result, relaying signals, $S_{1S} = 0$ and $S_{1S} \neq 0$ are shown in Fig. 6.6(c), and therefore a reverse direction to fault is determined and a blocking signal is issued.

6.3.4 A solid fault at the busbar in reverse direction

When a phase-A-earth fault takes place at busbar S, immediately behind the relaying point, the quadratic MMGs of the transient aerial mode current and voltage are shown in Figs. 6.7(a) and 6.7(b). It should be noted that in Fig. 6.7(c), a disturbance occurs on relaying signal S_{1S} at the time of around 0.025ms. This phenomena is caused by the superimposition of reflected transient waves from the remote busbar R, which appears as the incident wave at busbar S. On this limiting condition, a preset confirmation time period can be determined as aforementioned. Hence, within this time period, $S_{1S} = 0$ and $S_{2S} \neq 0$, a reverse direction to fault is detected.

6.3.5 Comparison between the MM and WT methods

The comparison between the proposed MM technique and WT method has been undertaken. A Morlet Wavelet with a 100μs data window and 40kHz center frequency is employed to process the input signals. The best data window and center frequency were determined by trial and error. With a solid fault condition shown in Fig. 6.4(a), the comparison result is given in Fig. 6.8, where C_{WT} denotes the WT coefficient. It can be seen that the transient features extracted by the quadratic MMG are superior over those obtained using WT analysis, in terms of sharpness of responses. On the other hand, it can be easily observed from Fig. 6.8 that the WT method has a delay of $100\mu s$ in response to the waveform changes, which is caused by the large data window required to cover the period of the Morlet Wavelet. However the MM technique can provide a rapid response simultaneously to the signal changes, since it requires a much shorter data window for calculation. Furthermore, the simple computation of the MMG technique is a most preferable merit for the ultra-high-speed protection relay. Due to the space limitation of the paper, more details of the comparison are not reported here, but the WT method can be referred to in reference.

6.4 Conclusion

A novel morphological protection technique has been presented in this chapter, which was undertaken in collaboration with colleagues [34]. The proposed technique possesses the following advantages:

- A short data window with 8 sample points covering a period of $8\mu s$ at a sampling rate of 1MHz is required in this case.
- Fast calculation can be undertaken with only addition, subtraction and comparison operations involved, in contrast with the integral transform methods, e.g. Fourier and Wavelet transform, which require more complex computation;
- The MMG technique provides the excellent capability of extracting the transient features of fault waveforms as well as their polarities exactly and indicating sudden changes of the waveform accurately.

The simulation results have shown that the MM technique is capable of accurately extracting the transient features of fault voltage and current, as a promising means for ultra-high-speed protection relaying. Using the quadratic MMG, the relaying signals are able to provide correct directional response to a transmission line fault under different fault types, positions, path resistances and inception angles.

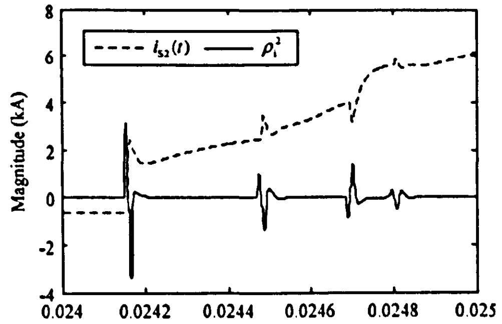

(a) The aerial mode current and its quadratic MMG

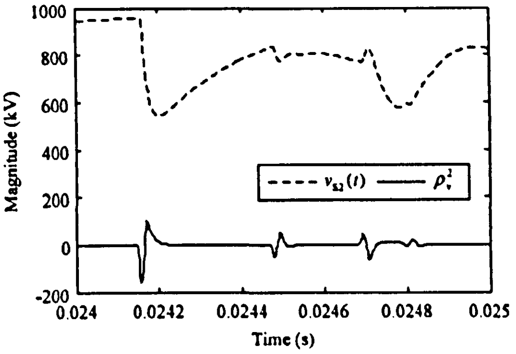

(b) The aerial mode voltage and its quadratic MMG

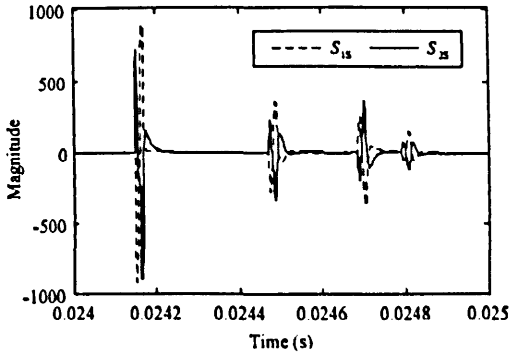

(c) Relaying signals

Fig. 6.4: Forward direction discrimination to a solid phase-A-earth fault at 48km from busbar S on section P

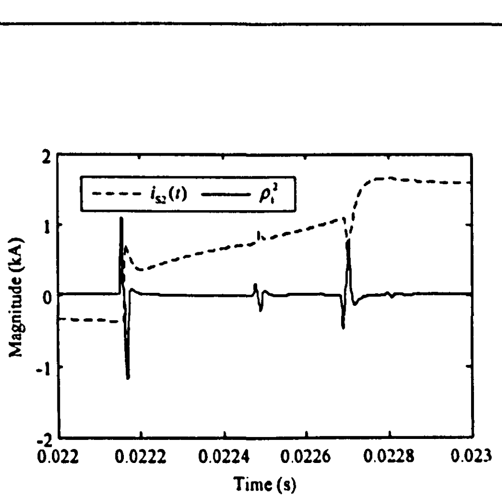

(a) The aerial mode current and its quadratic MMG

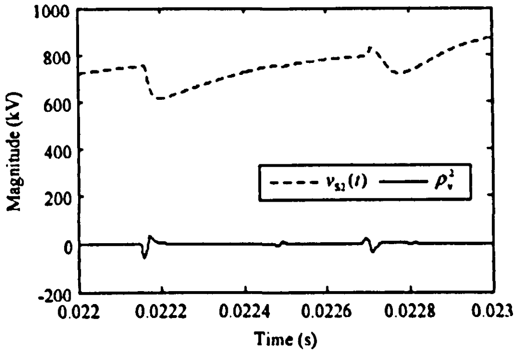

(b) The aerial mode voltage and its quadratic MMG

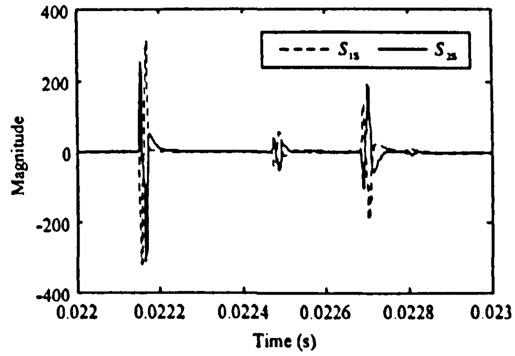

(c) Relaying signals

Fig. 6.5: Forward direction discrimination to a phase-A-earth fault with fault path resistance 200Ω at 48km from busbar S on section P

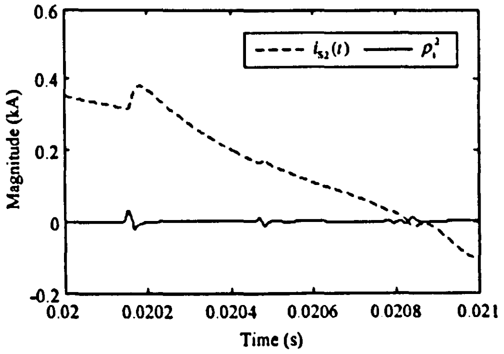

(a) The aerial mode current and its quadratic MMG

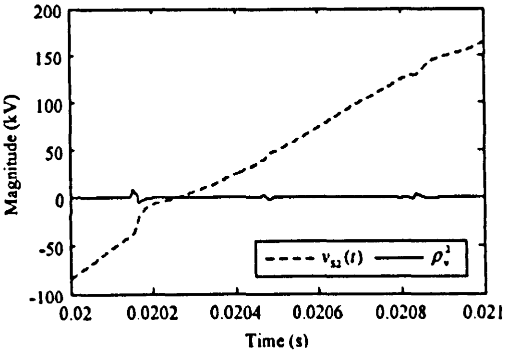

(b) The aerial mode voltage and its quadratic MMG

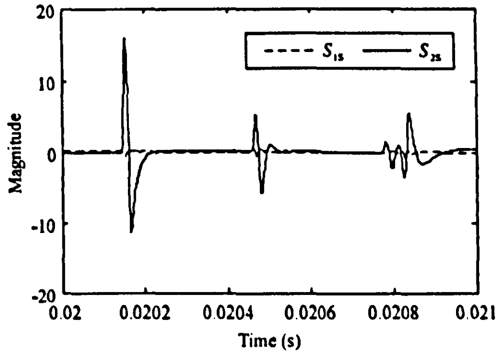

(c) Relaying signals

Fig. 6.6: Reverse direction discrimination to a phase-A-earth fault with fault inception angle 0° at 47*km* from busbar S on section Q

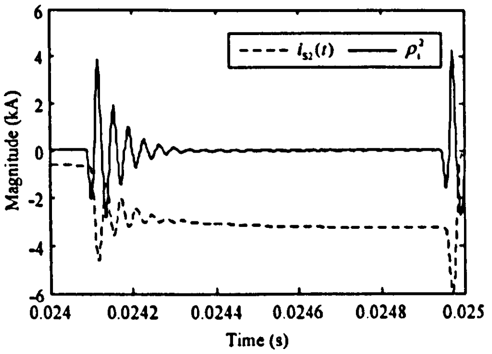

(a) The aerial mode current and its quadratic MMG

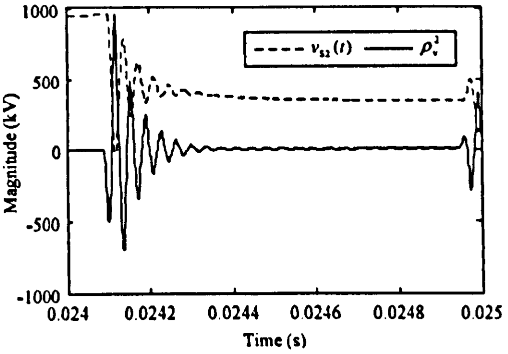

(b) The aerial mode voltage and its quadratic MMG

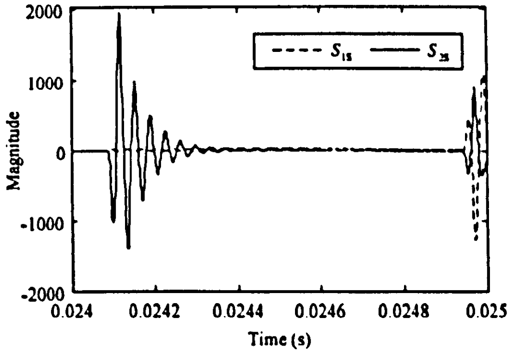

(c) Relaying signals

Fig. 6.7: Reverse direction discrimination to a solid phase-A-earth fault at busbar S

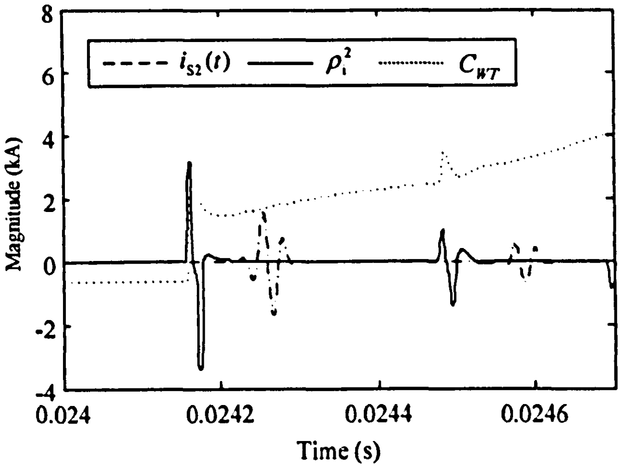

Fig. 6.8: Comparison between the results of quadratic MMG and WT analysis.

Chapter 7

Accurate Fault Location Based On Fault Transient Extraction Using MMG and MNTMG technique

7.1 Introduction

In recent years, the travelling wave based fault location technique has been recognized as a preferred tool in electric utilities [91]. Its outstanding advantage is the absence of restrictions or limitations on fault conditions, such as arcing and fault resistance, etc. and of power network configurations. such as double-source lines and series compensated lines, etc. Most existing travelling wave based fault locators use a double-ended technique, measuring the time difference between the first fault-generated transient wavefronts at opposite ends of the line. GPS synchronizing is used to achieve the required degree of that measurement accuracy. However, the single-ended fault location technique is desirable, since it can operate at one end of the line and would not require a communication link. It would therefore be less expensive and this may allow its use for distribution systems [92]. However, in comparison with the double-ended fault locators, the single-ended technique is more sophisticated, as it needs to accurately measure the time difference between the first and subsequent transient wavefronts and recognize their polarity. On the other hand, in the conventional fault locators, the calculation of travelling wave propagation speed is required, which depends on the knowledge of network parameters. A little inaccuracy of the speed value will result in a large deviation of distances of fault locations.

The Mathematical Morphology (MM) technique has been applied for an ultra-high-speed directional protection relay by applying the Multi-resolution Morphology Gradient (MMG) operator to extract transient features from fault-generated voltage and current wave signals propagating along transmission lines during a post-fault period. The simulation results show that although the performance of MMG is satisfactory under various fault conditions, it will inevitably deteriorate when various disturbances are imposed on the transient current signal. These disturbances can be considered as noise. Therefore, in order to improve the accuracy of fault location, MNTMG decomposition scheme is proposed to effectively reduce the noise and extract transient features. Compared with MMG scheme, MNTMG decomposition scheme is improved to be noise tolerant.

In this chapter, firstly, the application of the MMG scheme in the fault location is presented. The performance of MMG is discussed and its insufficient are analyzed. Secondly, a process of deriving the direction discriminants of a fault taking place on transmission lines is given. Then the MNTMG decomposition scheme is used to extract the transient features directly from fault-generated transient signals with noise contamination. Finally a comparison study is undertaken where the combination of a low-pass filter and MMG scheme is presented.

7.2 Analysis of Fault Location Principle

7.2.1 Type A: a passive method single-ended fault locator

A fault at the second half of the line

Figure 7.1 shows a double-source transmission line system under a fault condition, which happened at the second half of line RS and its Bewley-lattice diagram. The transient current and voltage waves generated by a fault at point F travel away from the fault point at speed v. They arrive some time later at busbars R and S where part of the wave passes into the adjacent sections and the rest is reflected backwards. This process continues until the transient wavefronts become indistinct due to the their multi-reflection and attenuation. The operating principle of a Type A fault locator is developed on the successive identification of the travelling, high frequency, transients arriving at the measurement point. Reference to the first and subsequently captured transients, including their polarities, allow the distance to the fault from each end of the line to be obtained from Fig. 7.1 using the following formula:

$$L_{\mathrm{R}} = L - (T_{\mathrm{R2}} - T_{\mathrm{R1}})v/2, \tag{7.2.1}$$

$$L_{\mathrm{S}} = (T_{\mathrm{S2}} - T_{\mathrm{S1}})v/2, \tag{7.2.2}$$

where L_{R} and L_{S} indicate the measured distance between the fault and busbar R, T_{R1}, T_{R2} and T_{S1}, T_{S2} are times at which the captured transient sequences are observed, v is the propagation speed on the transmission line and L is the full length of transmission line.

In order to eliminate errors arising from the use of a theoretical speed value, an alternative calculation using the first three transient sequences is proposed as follows, which allows the speed v to be eliminated from (7.2.1) and (7.2.2) to give the formulae:

$$L_{\mathrm{R}} = (T_{\mathrm{R3}} - T_{\mathrm{R1}})L/((T_{\mathrm{R2}} - T_{\mathrm{r1}}) + (T_{\mathrm{R3}} - T_{\mathrm{R1}})), \tag{7.2.3}$$

$$L_{\mathrm{S}} = (T_{\mathrm{S3}} - T_{\mathrm{S1}})L/((T_{\mathrm{S2}} - T_{\mathrm{s1}}) + (T_{\mathrm{S3}} - T_{\mathrm{S1}})) \tag{7.2.4}$$

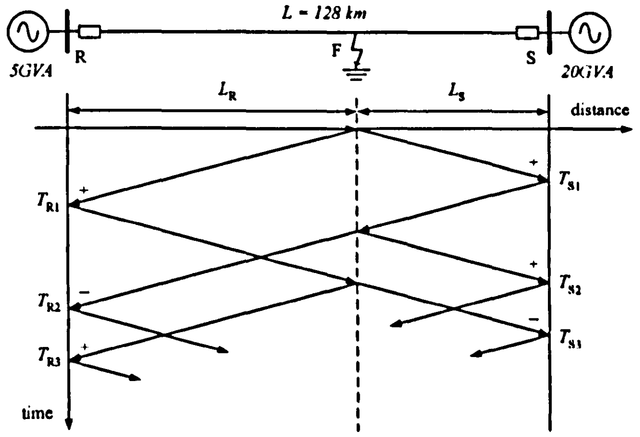

Fig. 7.1: Single-line diagram of $400kV$ power transmission lines system and its Bewley-lattice diagram under fault condition.

The validity of the above formulae hinges mainly on the recognition of the first two for formulae (7.2.1) and (7.2.2) or three for formulae (7.2.3) and (7.2.4) fault-generated transient wavefronts in terms of their maxima and polarities. This is why the single-ended fault locator requires an effective signal processing technique to enable an explicit discrimination of transient wavefront. For conventional methods, it is difficult to achieve due to the features of the fault-generated transient wavefronts changing in a very short time of period, furthermore, their shapes are affected by the attenuation, multi-reflection and the different fault conditions.

A fault at the first half of the line

When a fault happens at the first half the line, formulae ((7.2.1) and (7.2.2), (7.2.3) and (7.2.4) should be exchanged. Determining the fault position depends on the polarities of the second and third transient wavefronts, i.e polarity +, +, − and +, −, + for the fault at the first and second half of the line at each measurement point respectively, where the positive and negative polarity can be pre-defined with reference to the polarity of the first captured transient wavefront. The following simulation section will demonstrate how to define the reference polarity.

7.2.2 Type D: a passive method double-ended fault locator

A type D fault locator operates with the first transient waves observed at each end of the line. The advantage of this method lies in avoiding the need to identify multi-reflecting transient waves. However, an accurate time reference system like GPS is necessary to synchronize the time-tagging at each end of the line. The distance to the fault is calculated according to the time difference between TR1 and TS1 as indicated in Fig. 7.1 and is given as:

$$
\begin{aligned}
L_R &= (L + (T_{R1} - T_{S1})v)/2, && (7.2.5)\\
L_S &= (L + (T_{S1} - T_{R1})v)/2. && (7.2.6)
\end{aligned}
$$

7.2.3 Type E: a active method single-ended fault locator

An active method referred to as Type E is proposed by Gale et al [91], the technique is similar to Type A, but takes advantage of line energizing transients generated by the reclosure of a circuit breaker (CB) when a permanent fault occurs. When a CB re-closes with a permanent fault existing on the transmission line, the transient current and voltage waves are generated at the point at which the power source is injected to re-energize the line. Assuming the CT is installed behind the CB near the busbar R, the first and subsequent transients observed at the measurement point are reflected either from the fault point if the fault exists, or the opposite end of the line, which could be either an open circuit if the opposite CB has opened, or the busbar. The propagation of the travelling wave for the case of a permanent fault and opposite CB open is illustrated in Fig. 7.2. In such a situation, the incident transient wave is completely reflected with the same polarity at end S. Formulae (7.2.1) and (7.2.3) also apply to a Type E fault locator to calculate the fault distance. Therefore, for a permanent fault, the Type E fault locator can be used to reaffirm the fault distance in support of Type A.

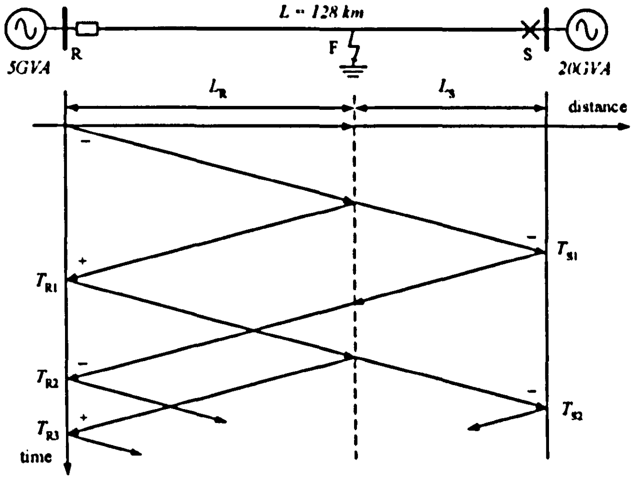

Fig. 7.2: Single-line diagram of $400kV$ power transmission lines system and its Bewley-lattice diagram under re-closing in a permanent fault condition.

7.3 Applying MMG in Accurate Fault Location and Its Insufficient

With the objective of effective feature recognition of the transient wave, a variety of fault scenarios have been simulated to evaluate the validity of the MMG analysis applied to different type fault locators. The voltage and current signals observed at each end of the line are firstly transformed into aerial mode (mode 2) current and voltage signals by the Clark modal transformation. Then a quadratic MMG (level $a = 2$) technique with 5 sampling points along the length of a flat line SE ($l_g = 5$) is utilized to process the modal signals in order to extract and locate the transient sequences. Finally, with reference to the maxima and their polarities derived from the quadratic MMG of the aerial modal signals, the distance to the fault can be obtained from the formulae given before with respect to the Type A, D and E.

The PSCAD/EMTDC software was employed to simulate a double-source transmission system based on the frequency-dependant transmission line model. All parameters are given with reference to a 400kV EHV line, and as that used in the UK SuperGrid system. The sampling rate of signals is 1MHz, i.e. $1\mu s$

per sample. With this order of time resolution, the fault locations can be confined to an accuracy of ±300m irrespective of the errors introduced by speed and line length.

7.3.1 Fault location analysis using MMG

Fault location with a general case

In Fig. 7.1, a solid phase-A-earth fault occurs at a distance of 80km from busbar R, the aerial mode current signals observed at busbar R, i_{R2}, and its associated quadratic MMG, ρ_i^2 are shown in Fig. 7.3. The arrow marks indicate the transient sequences recognized by the maxima of quadratic MMG. Adopting the definition of a positive transient being the positive pulse leading its negative pulse, the polarities of transient sequences are indicated by the direction of arrow marks.

The determination of the transient sequences is achieved by means of the maxima and polarities of the quadratic MMG. Equations (7.2.1) and (7.2.3) are then applied to calculate the fault distance according to Type A fault locator. The results are shown in Table 7.1. Note that due to the elimination of the speed variable from the formulae, the Type A fault locator using formulae (7.2.3) is much more accurate.

Table 7.1: Results of fault location analysis with a phase-A-earth fault at 80km from busbar R

Locator	Formula	Error (m)
Type A	(7.2.1)	+385.9
Improved Type A	(7.2.3)	−74.4

Fault location with a fault close to busbar

Generally, it is difficult to accurately detect the short distance to a fault that takes place very close to a busbar, because of the multi-reflection and

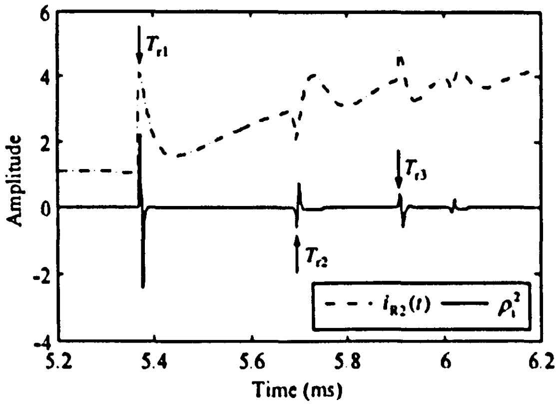

Fig. 7.3: Fault location analysis with a phase-A-earth fault at 80km from busbar R using quadratic MMG

the high propagating speed of transient waves. However, the quadratic MMG can provide a satisfactory performance as shown in Fig. 7.4, due to its short data-window and edge-shape detecting capability. The results attained for a fault location with a phase-A-earth fault at $2km$ from busbar R are listed in Table 7.2. In this case, the sampling rate largely dominates the accuracy of the results, instead of the wave propagation speed. Theoretically, at the level 2 of MMG with 5 point samples length of SE, a fault distance could be detected as close as up to 1km to the busbar. However, it should be mentioned that the Wavelet analysis method cannot be applied as the transient waveform has been distorted by the high frequency components and its processing requires a large data window which makes the wavefronts overlapped.

Table 7.2: Results of fault location analysis with a phase-A-earth fault at 2km from busbar R

Locator	Formula	Error (m)
Type A	(7.2.1)	+63.8
Improved Type A	(7.2.3)	+88.6

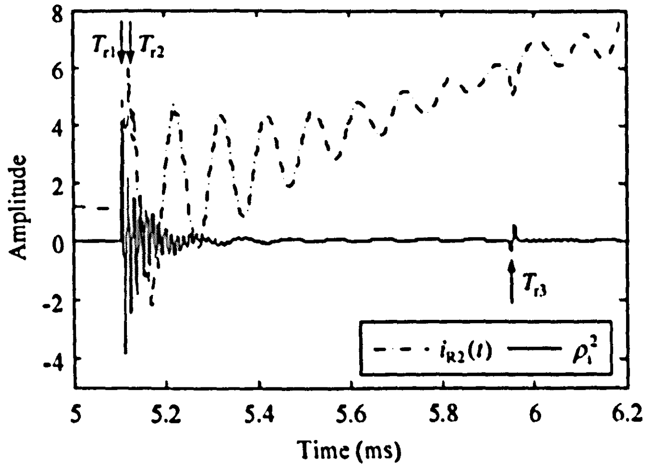

Fig. 7.4: Fault location analysis with a phase-A-earth fault at 2km from busbar R

Fault location utilizing switching-in transients

When energizing a transmission line with an existing permanent fault, the basic operating principle of Type E fault locator is the same as that of Type A except that the first transient observed at busbar R is a reflection from the fault point rather than originated from it. Figure 7.5 shows the modal current observed at busbar R and the results of the transient extraction. The results shown in Table 7.3 are found to be identical with those obtained in Type A for the same fault position (Table 7.1).

Table 7.3: Results of fault location analysis with a Type E locator for a permanent phase-A-earth fault at 80km from busbar R

Locator	Formula	Error (m)
Type E	(7.2.1)	+385.9
Improved Type E	(7.2.3)	−74.4

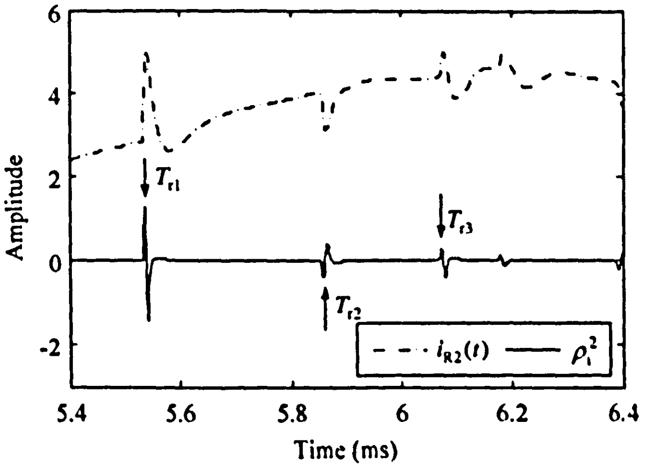

Fig. 7.5: Fault location analysis for a Type E locator with a permanent phase-A-earth fault at 80km from busbar R

7.3.2 The MMG technique for fault transient extraction in noisy environments

In order to extract the transient waves, the MMG filtering technique was developed [34] [49]. A quadratic MMG technique with a SE of 5 sampling points along a flat line is utilized to process the transient current signal in order to extract the transient sequences. The transient features can be extracted accurately as shown in Fig. 7.6. It must be mentioned that in this case, disturbances, which can be considered as noise, are not included in the simulation study, and the influence of noise cannot be ignored.

In order to evaluate the performance of the MMG scheme for noise tolerance, transient signals with different Signal-to-Noise Ratios ($SNRs$) are used in the simulation study. In Fig. 7.7, the input signal, taken as the current signal observed at busbar R of the line transformed into aerial mode (mode 2) current signal, i_{R2}, is disturbed with Gaussian white noise. From Fig. 7.7, it can be seen that with decreasing SNR, the wavefronts will be more difficult to detect and the accuracy of the MMG scheme drops rapidly. The detection errors are listed in Table 7.4.

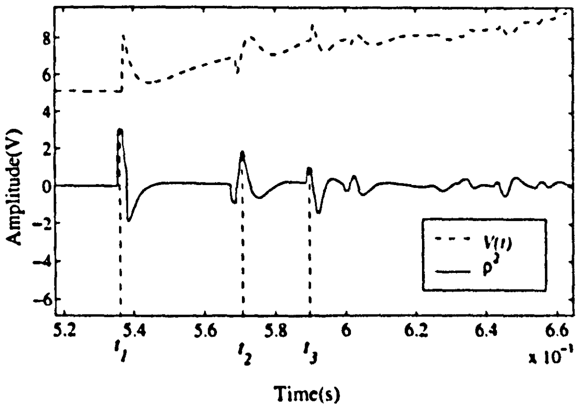

Fig. 7.6: The performance of the MMG scheme without noise disturbance.

Table 7.4: The errors in fault location with a phase-A-earth fault at 80km from busbar R, using the MMG scheme with different *SNRs*

SNR (dB)	Error (m)
45.81	−223
39.79	−2008
30.20	−3423
25.90	−69689

Based on the previous analysis, it can be seen that the fault locations cannot be found accurately by the MMG scheme when the *SNR* does not equal 0. Therefore a method which can achieve transient features extraction as well as noise reduction needs to be employed. The MNTMG decomposition scheme is selected to solve these issues.

7.4 Applying MNTMG for Fault Transient Extraction

The PSCAD/EMTDC software was employed to simulate a double-source transmission system based on the frequency-dependant transmission line model

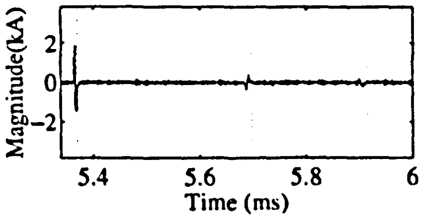

(a) SNR= 45.85dB

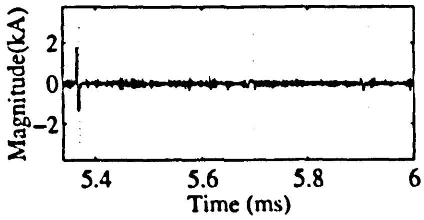

(b) SNR= 39.79dB

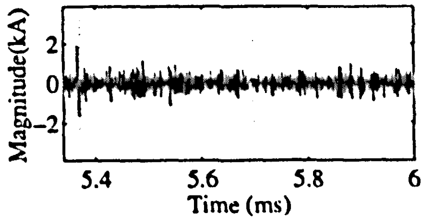

(c) SNR= 30.22dB

Fig. 7.7: The performance of MMG scheme with noise disturbances. The dotted lines illustrate the positions of time-tags T_{R1}, T_{R2} and T_{R3} when no noise is imposed in the signal.

[49]. All parameters are given with reference to a 400kV EHV line, as used in the UK SuperGrid system. The voltage and current signals observed, at each end of the line, are transformed into aerial mode (mode 2) current and voltage signals by the Clark modal transformation. Further information about the simulation study of the power transmission lines can be found in [34].

7.4.1 Different levels of the MNTMG scheme for fault transient extraction

Based on the expression of the analysis operator of the MNTMG scheme MNTMG decomposition (4.2) and its construction, which is shown in Fig. 4.2, the output of each level can be expressed as:

$$r_n = \frac{1}{2^n}(\delta\varepsilon + \varepsilon\delta)^n(\delta - \varepsilon)^n[i_{R2}(t)], \qquad (7.4.1)$$

where r_n denotes the nth level output. Defining $\psi_n^{\uparrow} = \frac{1}{2^n}(\delta\varepsilon + \varepsilon\delta)^n(\delta - \varepsilon)^n$, then when $n = 2$,

$$r_2 = \frac{1}{4}(\delta\varepsilon + \varepsilon\delta)^2(\delta - \varepsilon)^2[i_{R2}(t)].$$

The operator $(\delta - \varepsilon)^2$ is the quadratic morphological gradient.

The second level of the MNTMG scheme is chosen as output ($\psi_2^{\uparrow}$) with 5 sampling points along the length of a flat line, SE ($l_g = 5$) was utilized to process the modal signals in order to extract and locate the transient sequences from the voltage and/or current signal. Finally, with reference to the maxima derived from the $\psi_2^{\uparrow}$ of the aerial modal signals, the distance to the fault can be obtained by (7.2.3) and (7.2.4) with respect to a Type A fault locator.

Figure 7.8 illustrates the outputs of $\psi_2^{\uparrow}$, $\psi_4^{\uparrow}$ and $\psi_5^{\uparrow}$, when $SNR = 0$. It is shown that with increasing n, the extracted transient features are badly deformed. When $n = 4$ or $n = 5$, the polarity of the transient features cannot be determined. Not only are the polarity of the transient features effected by the extraction, but also the accuracy of the determinations of the transient features. In Table 7.5, the errors of different levels of the MNTMG scheme are shown. Based on the analysis above, and the effects of quadratic morphological gradient in transient feature extraction, the second level of MNTMG, $\psi_2^{\uparrow}$, was chosen as the operator to fulfill the task of transient feature extraction and noise reduction.

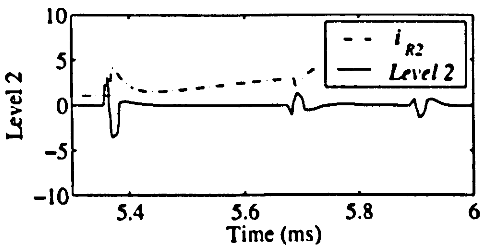

(a) The second level output of MNTMG scheme

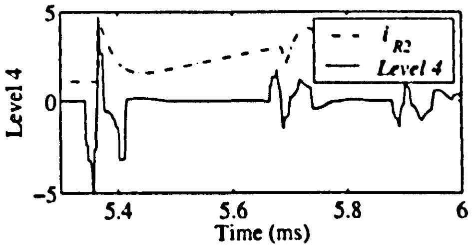

(b) The forth level output of MNTMG scheme

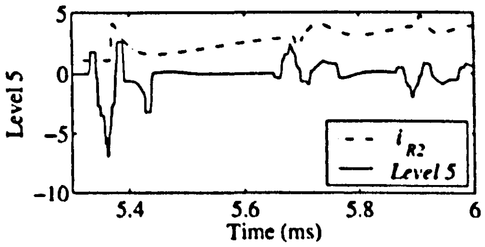

(c) The fifth level output of MNTMG scheme

Fig. 7.8: Different level outputs of MNTMG scheme

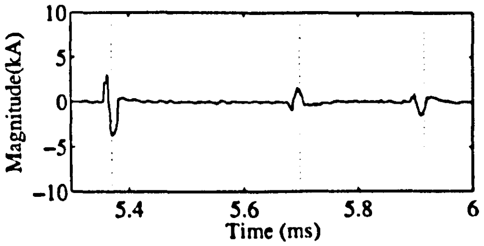

(a) SNR=39.82dB

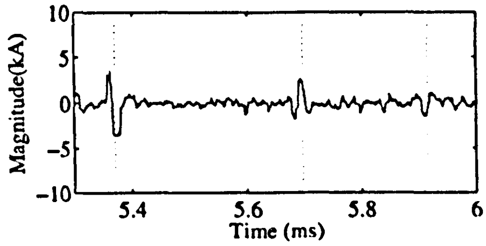

(b) SNR=25.80dB

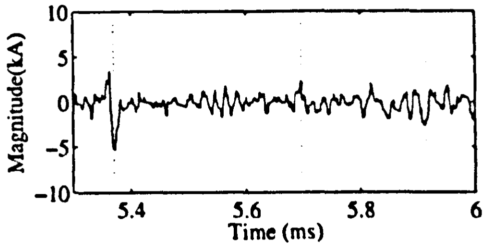

(c) SNR=20.73dB

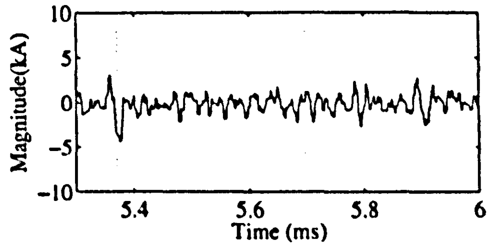

(d) SNR=19.01dB

Fig. 7.9: The performance of the MNTMG scheme with different noise disturbance. The dotted lines in the figures illustrate the positions of time-tags T_{R1}, T_{R2} and T_{R3} when no noise is imposed on the signal.

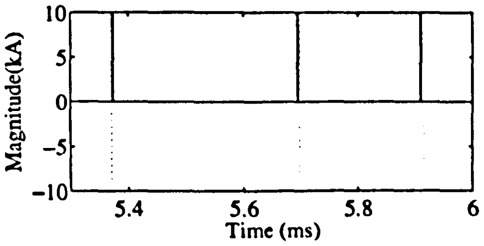

(a) SNR=39.82dB

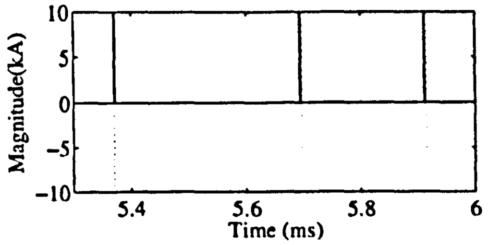

(b) SNR=25.80dB

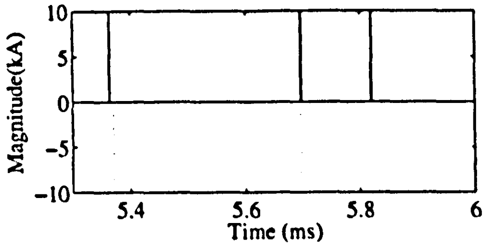

(c) SNR=20.73dB

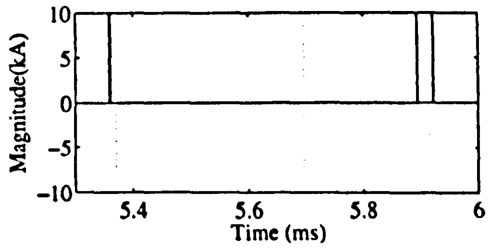

(c) SNR=19.01dB

Fig. 7.10: The determination of the transient features after the MNTMG scheme extraction with noise disturbance. The dotted lines illustrate the positions of time-tags T_{R1}, T_{R2} and T_{R3} when no noise is imposed on the signal.

Table 7.5: The errors in fault location with a phase-A-earth fault at 80km from busbar R, using the MNTMG scheme without noise.

Level	Error (m)
$\psi_2^{\uparrow}$	+56
$\psi_3^{\uparrow}$	−1358
$\psi_4^{\uparrow}$	+1150
$\psi_5^{\uparrow}$	−5030

7.4.2 The performance of the MNTMG scheme for fault transient extraction

A variety of $SNRs$ have been simulated to evaluate the validity of the MNTMG scheme. Figures 7.9 and 7.10 illustrate the performance of the MNTMG scheme with noise disturbance and the determination of the transients features respectively. Table 7.6 shows the errors in fault location with a phase-A-earth fault at 80km from busbar R, when the SNR varies from 45.77dB to 19.01dB. It is shown that the first time-tag T_{R1} can be extracted in almost all the circumstances when the SNR varies from 45.77dB to 19.01dB. The second time-tag T_{R2} and T_{R3} can only be extracted when the SNR is larger than 20.73dB. From Table 7.6, it is apparent that the limitation of the MNTMG scheme is a SNR of 25.80dB. If the SNR is less than 25.80dB, the accuracy of the MNTMG scheme cannot be confirmed and the scheme becomes useless. Furthermore as shown in Table 7.6, the error in the case of $SNR = 30.28$dB reaches 299m. Although it is even larger than the error when $SNR = 25.80$dB, it is still within the requirement of the system which is ±300m [49].

Table 7.6: The errors in fault location with a phase-A-earth fault at 80km from busbar R, using the MNTMG scheme. The SNR varies from 45.77dB to 19.01dB.

SNR (dB)	Error (m)
45.77	+56
39.82	+74
30.28	+299
25.80	+93
22.94	−1200
20.73	−6091
19.01	−14360

7.4.3 Comparison between the MNTMG scheme and the MMG scheme with a Butterworth low-pass filter

A comparison between the proposed MNTMG scheme and the MMG scheme with a Low-Pass Butterworth filter (MMGLP) has been undertaken. The later employs a 9th-order low-pass Butterworth filter before the signal $i_{R2}(t)$ is fed into the MMG filter. Varies frequencies have been tested and 30kHz is chosen as the cutoff frequency of the low-pass filter, which shows better representation than the other frequencies'. The frequency response of the filter is show in Fig. 7.11.

The comparison between the MNTMG scheme and the MMGLP filter is shown in Fig. 7.12. Figure 7.12 (a) illustrates the sharpness of the waveform changes. It is shown that the low-pass filter not only reduces the high frequency noise, but also smooths the waveform changes, which brings difficulties to the determination of transient features. The performance of MMGLP filter with a variety of $SNRs$ is shown in Table 7.7.

In Fig. 7.12 (b) a comparison between the MNTMG scheme and the MMGLP filter, in response to the waveform changes is shown. It can be seen

Table 7.7: The errors in fault location with a phase-A-earth fault at 80km from busbar R using the MMGLP filter. The SNR varies from 45.85dB to 18.98dB.

SNR (dB)	Error (m)
45.85	+94
39.82	+94
30.32	+187
25.86	+1774
22.94	+2024
20.73	+1482
18.98	−14418

that the transient features extracted by the MNTMG scheme are superior over those obtained using the MMGLP filter, in terms of sharpness of responses. It can be observed from Fig. 7.12 (b) that the MMGLP filter has a delay of $35\mu s$ in response to the waveform changes, which is caused by the large data window. However the MNTMG scheme can provide a rapid response simultaneously to the signal changes, since it requires a much shorter data window for calculation. Furthermore, the mathematical calculations involved in the MNTMG operators includes only addition, substraction, and sorting operations without any multiplication and division, which are used in other mathematical tools including the Wavelet Transform. When acting upon signals of complex shapes, morphological filters are fast and easy to implement. The simple computation requirements of MM based schemes allow them to be applied to many applications.

7.5 Conclusion

In this chapter, the works of accurate fault location using MMG which was undertaken in collaboration with colleagues was firstly introduced [49]. The proposed MMG scheme is satisfactory under various fault conditions. However

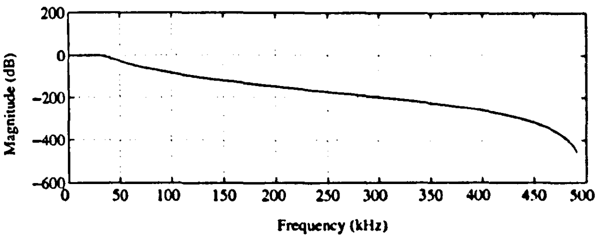

Fig. 7.11: The magnitude/frequency response of the low-pass filter with a cutoff frequency of 30kHz used with the MMG scheme.

it will inevitably deteriorate under noise disturbance. Thus, another mathematical morphology based MNTMG decomposition scheme has been proposed to effectively reduce noise in the transient signals on transmission lines and significantly improve the performance of fault location. The construction of its analysis operator has been discussed in detail and different levels of the scheme have also been investigated. The results show that the second level performs better in noise reduction compared with the other levels. The efficiency of the MNTMG decomposition scheme noise reduction has been evaluated in simulation studies. Compared with the MMG scheme, the results show that the MNTMG decomposition scheme performs satisfactorily and is able to extract the features of transient signals accurately in noisy environments.

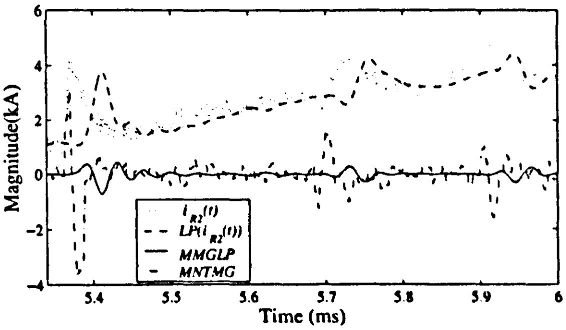

(a) Results comparison between the MNTMG scheme and MMGLP filter in the sharpness to the waveform changes. SNR=30.25dB

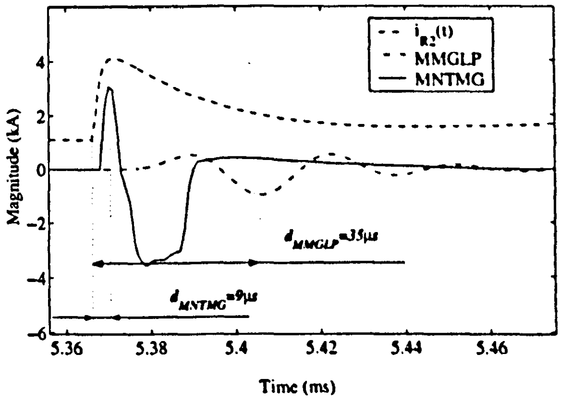

(b) Results comparison between the MNTMG scheme and MMGLP filter in the response to the waveform changes. SNR=0dB

Fig. 7.12: Accurate location of the transient wavefront represented by maxima of the MNTMG scheme compared with the result of the MMGLP filter with a phase-A-earth fault at 80km from busbar R.

Chapter 8

Conclusions

8.1 Introduction

This chapter concludes the dissertation. It summarizes the major results of the presented research work and indicates directions for further investigations based on this work.

8.2 Summary of the Thesis

The research contributions of this thesis mainly lies in two aspects: exploring the effect of morphological operator in the frequency domain and using morphological operators to extract 1-D signals geometrical properties in applications. They are set out in Chapters 3, 4, 5, 6 and 7. Their contents will be subsequently summarized.

Chapter 3 introduced the process of finding the transform of weighted morphological dilation in the frequency domain under the preconditions. In the deduction, it is also found that when the parameter of ED filer k varies from 1 to M, the sum of these sequences is the convolution of the signal and the structuring element.

Chapter 4 presented three morphological undecimated wavelet decomposition schemes. They are the Multi-resolution Morphological Top-Hat scheme

(MMTP), the Multi-resolution Morphological Gradient scheme (MMG) and the Multi-resolution Noise Tolerant Morphological Gradient scheme (MNTMG). All of them are based on the theory of morphological wavelet. The proposed three schemes inherit the multi-dimension and multi-level analysis of traditional wavelet and pyramid, whilst they ignore the time-frequency domain analysis of wavelet and extends the original wavelet and pyramid from the linear domain to the nonlinear domain.

Chapter 5 presented the application of the MMTP scheme for discriminating magnetizing inrush from internal fault in transformer protection. In the application, the MMTP scheme shows its effect in distinguishing symmetrical features from asymmetrical features on the waveform.

Chapter 6 presented the application of the MMG scheme in the ultra-high-speed directional transmission line protection. The MMG scheme provids a short data window with 8 sample points covering a period of $8\mu s$ at a sampling rate of $1MHz$ which is required in this case. It also contains a fast calculation with only addition, subtraction and comparison operations involved, in contrast with the integral transforms, which require more complex computation.

Chapter 7 introduced the application of the MNTMG to detect fault locations with noise disturbance in the transmission line systems. A comparison between the MNTMG scheme and the combination of Low-Pass filter and MMG scheme (MMGLP) is undertaken. The simulation results have proven that the accuracy and reliability of the MNTMG scheme is more accurate and reliable than MMGLP.

8.3 Limitations of the Approach

One of the major limitations using mathematical morphology was the lack of analytical methods, especially in 1-D signal processing.

The next drawback was about the analysis of weighted morphological operators in the frequency domain. In this part, (3.4.1) plays an important role for the further deduction in that chapter. As we reckoned, it is still tenable when

$f(n)$ and $g(m)$ are arbitrary, but it still cannot be proved. Furthermore, in this chapter, only weighted dilation is given a transform in the frequency domain, the other basic morphological operator: erosion was not mentioned. As we reckoned, besides the two preconditions, if the structure element is symmetric with respect to its origin, the transform of weighted erosion in the frequency domain can be also found.

8.4 Recommendations for Future Work

With an understanding of the presented methods and schemes, the following aspects would be worthy of further investigations:

- The attempt of describing the frequency properties of weighted dilation has made a breakthrough, but the assumptions are still very strict and only one weighted morphological operator is . It is worth investigating the effects of the morphological operations to arbitrary signals in the frequency domain.
- The theory of the morphological wavelet and pyramid provides a theoretical basis for the construction of morphological multi-resolution decomposition schemes. Some applications have adopted it successfully. It is worth applying the theory in more fields. On the other hand, compared with the theory of wavelet, the theory of the morphological wavelet is not rigorous enough. Complete lattice based theoretical improvements are required.

References

[1] D. Schonfeld, "Morphological processing of medical images: An introduction," in *Proceedings of IEEE International Symposium on Circuits and Systems*, vol. 1, pp. 746–749, 1991.

[2] J. Serra and P. Soille, *Mathematical morphology and its applications to image processing.* The Netherlands: Kluwer Academic Publishers, 1994.

[3] G. Birkhoff, *Lattice theory.* Rhode Island: American Mathematics Society, 1979.

[4] G. Matheron, *Random Sets and Integral Geometry.* New York: John Wiley & Sons, 1975.

[5] J. Serra, *Image Analysis and Mathematical Morphology.* London: Academic Press, 1982.

[6] J. Serra, *Image Analysis and Mathematical Morphology. II: Theoretical Advances.* London: Academic Press, 1988.

[7] H. Minkovski, "Volumen und oberflache," *Math. Annalen*, vol. 57, pp. 447–495, 1903.

[8] H. Hadwiger, *Vorlesungen uber inhalt, oberflache und isoperimetrie.* Berlin: Springer–Verlag, 1957.

[9] P. Maragos, "A representation theory for morphological image and signal processing," *IEEE Transactions on Pattern Analysis and Machine Intelligence*, vol. 11, pp. 586–599, 1989.

[10] J. Serra, "Introduction to mathematical morphology," *Computer Vision, Graphics and Image Processing*, vol. 35, pp. 283-305, 1986.

[11] H. J. A. M. Heijmans, *Morphological Image Operators.* Boston: Academic Press, 1994.

[12] J. Serra, "Mathematical morphology and CMM : a historical overview," tech. rep., Center of Mathematical Morphology, 2000.

[13] R. M. H. S. R. Sternberg and X. Zhuang, "Image analysis using mathematical morphology," *IEEE Transactions on Pattern Analysis and Machine Intelligence*, vol. 9, pp. 532–550, 1987.

[14] D. Graham and P. Norgren, "The Diff3 analyzer: A parallel/serial Golay image processor," in *Real Time Medical Image Processing* (M. Onoe, K. Preston, and A. Rosenfeld, eds.), pp. 163–182, London: Plenum Press, 1980.

[15] F. Gerritsen and L. G. Aardema, "Design and use of DIP-1: A fast flexible and dynamically microprogrammable image processor," *Pattern Recognition*, vol. 14, pp. 319–330, 1981.

[16] A. J. Baddeley and H. J. A. M. Heijmans, "Incidence and lattice calculus with applications to stochastic geometry and image analysis," *Applicable Analysis in Engineering, Communication, and Computing*, vol. 3, pp. 129-146, 1995.

[17] F. Meyer, "From connected operators to levelings," in *Mathematical Morphology and its Applications to Image and Signal Processing* (H. J. A. M. Heimans and J. Roedink, eds.), pp. 191–199, Kluwer Academic Publishers, 1998.

[18] B. S, "Interpolation of sets, of partitions and of functions," in *Mathematical Morphology and its Applications to Image and Signal Processing* (H. J. A. M. Heimans and J. Roedink, eds.), Kluwer Academic Publishers, 1998.

[19] H. Heijmans and P. Maragos, "Lattice calculus of the morphological slope transform," Report BS-R9531, Centrum voor Wiskunde en Informatica, 1995.

[20] P. Maragos, "Differential morphology and image processing," *IEEE Transactions on Image Processing*, vol. 5, pp. 922–937, 1996.

[21] J. Goutsias and H. J. A. M. Heijmans, "Nonlinear multiresolution signal decomposition schemespart I: Morphological pyramids," *IEEE Transactions on Image Processing*, vol. 9, pp. 1862–1876, 2000.

[22] P. Maragos and R. W. Schafer, "Morphological systems for multidimensional signal processing," *Proceedings of the IEEE*, vol. 78, no. 4, pp. 690–710, 1990.

[23] O. I. Camps, T. Kanungo, and R. M. Haralick, "Gray-scale structuring element decomposition," *IEEE Transactions on Image Processing*, vol. 5, pp. 111–120, 1996.

[24] C. Gu, *Multivalued morphology and segmentation-based coding*. PhD thesis, École Polytechnique Fédérale De Lausanne, 1995.

[25] H. J. A. M. Heijmans and J. Goutsias, "Nonlinear multiresolution signal decomposition schemespart II: Morphological wavelets," *IEEE Transactions on Image Processing*, vol. 9, pp. 1897–1913, 2000.

[26] F. L. R. Leonardi and A. Signoroni, "High-performance embedded morphological wavelet coding," vol. 10, pp. 293–295, 2003.

[27] P. F. M. Nacken, *Image analysis methods based on hierarchies of graphs and multi-scale mathematical morphology*. PhD thesis, University of Amsterdam, 1994.

[28] A. Zarandy, A. Stoffels, T. Roska, and L. O. Chua, "Implementation of binary and gray-scale mathematical morphology on the CNN universal machine," *IEEE Transactions on Circuits and Systems: Fundamental Theory and Applications*, vol. 45 (2), pp. 163-168, 1998.

[29] R. van den Boomgaard, *Mathematical Morphology: Extensions towards computer vision.* PhD thesis, University of Amsterdam, 1992.

[30] M. H. Sedaaghi, "Direct implementation of open-closing in morphological filtering," *Electronics Letters*, vol. 33, no. 3, pp. 198–199, 1997.

[31] M. H. Sedaaghi and Q. H. Wu, "Weighted morphological fillter," *Electronics Letters*, vol. 34, pp. 1566–1567, 1998.

[32] Q. Li, Z. Ji, and Q. H. Wu, "An improved mathematical morphology filter for fault location in power transmission lines," *Proceedings of UKACC Control 2004*, vol. University of Bath, 2004.

[33] P. Sun, J. F. Zhang, D. J. Zhang, and Q. H. Wu, "Morphological identification of transformer magnetising inrush current," *IEE Electronics Letters*, vol. 38, pp. 437–438, 2002.

[34] Q. H. Wu, J. F. Zhang, and D. J. Zhang, "Ultra-high-speed directional protection of transmission lines using mathematical morphology," *IEEE Transactions on Power Delivery*, vol. 18, no. 4, pp. 1127–1133, 2003.

[35] J. F. Zhang, J. S. Smith, and Q. H. Wu, "Morphological undercimated wavelet decomposition for fault location on power transmission lines," *IEEE Transactions on Circuits and Systems I: Regular Paper*, vol. 53, pp. 1395–1402, 2006.

[36] J. Serra, "Morphological filtering: an overview," *Signal Processing*, vol. 38, pp. 3–11, 1994.

[37] J. Song and E. J. Delp, "A study of the generalized morphological filter," *Circuits Systems and Signal Processing*, vol. 11, no. 1, pp. 229-252, 1992.

[38] G. Matheron, *Random sets and integrated geometry.* New York: John Wiley&Sons, 1975.

[39] P.Maragos and R.W.Schafer, "Morphological filters-part 1: their set-theoretic analysis and relations to linear shift-invariant filters," *IEEE*

Transactions on Acoustics, Speech and Signal Processing, vol. 35, no. 8, pp. 1153–1169, 1987.

[40] P. Maragos and R. W. Schafer, "Morphological filters-part 2: their relations to median, order-statistic, and stack filters," *IEEE Transactions on Acoustics, Speech and Signal Processing*, vol. 36, no. 8, pp. 1153–1184, 1987.

[41] S. J. Ko, A. Morales, and K. H. Lee, "Fast recursive algorithms for morphological operators based on the basis matrix representation," *IEEE Transactions on Image Processing*, vol. 5, no. 6, pp. 1073–1077, 1987.

[42] M. Khosravi and R. W. Schafer, "Implementation of linear digital filters based on morphological representation theory," *IEEE Transactions on Acoustics, Speech and Signal Processing*, vol. 42, no. 9, pp. 2264–2275, 1994.

[43] H. Heijmans, "Mathematical morphology: basic principles," in *Summer School on Morphological Image and Signal Processing*, (Zakopane, Poland), 1995.

[44] M. Sedaaghi and Q. H. Wu, "Real-time implementation of grey-scale morphological operators," *IEE Electronics Letters*, vol. 33, pp. 1761–1763, 1997.

[45] J. Serra, "Morphological filtering: An overview," *Signal Processing*, vol. 38, pp. 3–11, 1994.

[46] P. T. Jackway, *Morphological scale-space with application to 3d object recognition*. PhD thesis, Queensland University of Technology, 1994.

[47] R. G. Baraniuk, "Beyond time-frequency analysis: Energy densities in one and many dimensions," in *Proceedings of 1994 International Conference on Acoustic, Speech and Signal Processing (Los Alamitos, CA, Adelaide, Australia), IEEE Signal Processing Society*, vol. 3, pp. 357–360, 1994.

[48] Q. H. Wu, P. Sun, D. J. Zhang, and J. F. Zhang, "Identification of transformer inrush current using morphological signal decomposition," *Automation of Electric Power Systems*, pp. 67–78, 2002.

[49] D. J. Zhang, Q. H. Wu, J. F. Zhang, and K. I. Nuttall, "Accurate fault location based on transients extraction using mathematical morphology," *Electronics Letters*, vol. 38, no. 24, pp. 1583-1585, 2002.

[50] D. J. Zhang, Q. Li, J. F. Zhang, Q. H. Wu, and D. R. Turner, "Improving the accuracy of single-ended transient fault locators using mathematical morphology," in *IEEE/CSEE International Conference on Power System Technology*, vol. 2, (Kunming, China), pp. 788–792, 2002.

[51] J. Serra and L. Vincent, "An overview of morphological filtering," *Circuits Systems and Signal Processing*, vol. 11, pp. 47–108, 1992.

[52] C.Ronse, "Why mathematical morphology needs complete lattices," *Signal Processing*, vol. 21, pp. 126–154, 1990.

[53] R. Kresch, *Morphological image representation for coding applications.* PhD thesis, Israel Institute of Tech., 1995.

[54] M. H. Sedaaghi, *Morphological Filtering in Signal/Image Processing.* PhD thesis, University of Liverpool, 1998.

[55] R. M. Haralick, S. R. Sternberg, and X.Zhuang, "Image analysis using mathematical morphology," *IEEE Transactions on Pattern Analysis and Machine Intelligence*, vol. 4, pp. 532-550, 1987.

[56] P. Soille, *Morphological Image Analysis: Principles and Applications.* London: Springer-Verlag, 1999.

[57] S. R. Sternberg, "Grayscale morphology," *Computer Vision, Graphics and Image Processing*, vol. 35, pp. 333-355, 1986.

[58] D. Wang and D. C. He, "A fast implementation of 1-d grayscale morphological filters," *IEEE Transactions on Circuits, Systems and Signal Processing*, vol. 41, no. 9, pp. 634–636, 1994.

[59] M. H. Sedaaghi and Q. H. Wu, "Morphological filtering and convolution," in *Control '98. UKACC International Conference*, vol. 1, (University of Wales, Swansea, UK), pp. 235–240, 1998.

[60] A. V. Oppenhein and A. S. Willsky, *Signal & System (Second Edition)*. Prentice-Hall International, Inc., 1997.

[61] L. Alvarez and J. M. Morel, "Morphological approach to multiscale analysis: From principles to equations," in *Geometry-Driven Diffusion in Computer Vision* (B. M. ter Haar Romeny, ed.), Dordrecht: Kluwer Academic Publishers, 1994.

[62] J. A. Bangham, T. Campbell, and R. Aldridge, "Multiscale median and morphological filters for 2D pattern recognition," *Signal Processing*, vol. 38, pp. 387–415, 1994.

[63] A. C. Kamath and I. K. Fodor, "Undecimated wavelet transforms for image de-noising," technical report, Lawrence Livermore National Laboratory (LLNL), 2002.

[64] G. Anelli, A. Broggi, and G. Destri, "Decomposition of arbitrarily shaped binary morphological structuring elements using genetic algorithms," *IEEE Transactions on Pattern Analysis and Machine Intelligence*, vol. 20, no. 2, pp. 217–224, 1998.

[65] J. A. Bangham, P. Chardaire, C. J. Pye, and P. D. Ling, "Multiscale nonlinear decomposition: the sieve decomposition theorem," *IEEE Transactions on Pattern Analysis and Machine Intelligence*, vol. 18, no. 5, pp. 529-539, 1996.

[66] C. V. Robert, "A spatially variant, locally adaptive, background normalization operator," in *Mathematical morphology and its applications to im-*

age processing (J. Serra and P. Soille, eds.), pp. 45–52, Kluwer Academic Publishers, 1994.

[67] S. Mallat, *A Wavelet Tour of Signal Processing.* San Diego: CA: Academic, 1998.

[68] D. J. Zhang, Q. H. Wu, and Z. Q. Bo, "Transient positional protection of transmission lines based on complex wavelets analysis," *Proc. of CIGRE International Conference on Power Systems*, pp. 489–492, 2001.

[69] Waldron, J. E., Zocholl, and S. E., "Design considera- tions for a new solid state transformer differential relay with harmonic restraint," *Western Protective Relay Conference*, 1978.

[70] "Service manual type mbch biased differential relay," *ALSTOM T&D Control Ltd.*

[71] G.-M. M. and N. D.W., "A wavelet-based differential transformer protection," *IEEE Transactions on Power Delivery*, vol. 14, pp. 1351–1358, 1999.

[72] B. Z. Q., W. G, and L. T, "A new technique for transformer protection based on transient detection," *IEEE Transactions on Power Delivery*, vol. 15, pp. 870–875, 2000.

[73] M. Z., V. D. N., and S. S.P., "Ann-based protection scheme for power transformer," *Electric Machines and Power Systems*, vol. 28, 1999.

[74] P. J., G. B., and D. D., "Improved operation of power transformer protection using artifical neural network," *IEEE Transactions on Power Delivery*, vol. 12, pp. 1128 – 1136, 1997.

[75] K. Karsai, K. D., and L. Kiss, *Large Power Transformers.* New York: Elsevier, 1987.

[76] L. P., M. O. P., C. C., H. G. S., and G. Y., "Improved operation of differential protection of power transformers for internal faults," *IEEE Transactions on Power Delivery*, vol. 7, pp. 1912–1919, 1992.

[77] W. J. Wang, *Protective rinciple and operation of main electric equipment.* Beijing: China electric power press, 1996.

[78] W. J. Wang and B. X. Hou, *Elementary protective principle of main electric equipment.* Beijing: China electric power press, 1989.

[79] H. Dommel and J. Michels, "High speed relaying using travelling wave transient analysis," *IEEE PES Winter Meeting*, pp. 214–219, 1978.

[80] M. Yee and J. Esztergalyos, "Ultra high speed relay for ehv/uhv transmission lines-installation fault tests and operational experience," *IEEE Transactions on Power Systems*, vol. 97, pp. 1814–1825, 1978.

[81] A. Johns, "New ultra-high-speed directional comparison technique for the protection of e.h.v. transmission lines," *IEE Proc. Part C*, vol. 127, pp. 228–239, 1980.

[82] Z. Bo, "A new non-communication protection technique for transimmision lines," *IEEE Transactions on Power Delivery*, vol. 13, pp. 1073-1078, 1998.

[83] L. V. Bewley, *Travelling waves on transmission systems.* New York: Wiley & Sons, 1951.

[84] T. Chen and Q. H. Wu, "A pseudo top-hat mathematical morphological approach to edge detection in dark regions," *Pattern Recognition*, vol. 35, pp. 199–210, 2002.

[85] M. Vitins, "A fundamental concept for high speed relaying," *IEEE Transactions on Power Systems*, vol. 100, pp. 163–168, 1981.

[86] J. Bickford and M. Abdel-Rahman, "Application of travelling-wave methods to the calculation of transient-fault currents and voltages in power-system networks," *IEE Proc. Part C*, vol. 127, pp. 153–168, 1980.

[87] J. Marti, "Accurate modelling of frequency-dependent transmission lines in electromagnetic transient simulations," *IEEE Transactions on Power Systems*, vol. 101, pp. 147–155, 1982.

[88] A. Johns and R. Aggarwal, "Digital simulation of faulted e.h.v transmission lines with particular reference to very-high-speed protection," *IEE Proc. Part C*, vol. 123, pp. 353–359, 1976.

[89] A. Johns, R. Aggarwal, and Y. Song, "Improved techniques for modelling fault arcs on faulted ehv transmission systems," *IEE Proc. Generation, Transmission & Distribution*, vol. 141, pp. 148–154, 1994.

[90] A. T. Johns, R. K. Aggarwal, and Z. Q. Bo, "Non-unit protection technique for ehv transmission systems based on fault-generated noise, part 1: Signal measurement," *IEE Proc. Generation, Transmission & Distribution*, vol. 141, pp. 133–140, 1994.

[91] P. Gale, P. Taylor, P. Naidoo, C. Hitchin, and D. Clowes, "Travelling wave fault locator experience on eskom's transmission network," *IEE Seventh International Conference on Developments in Power System Protection*, pp. 327–330, 2001.

[92] M. Aurangzeb, P. Crossley, and P. Gale, "Fault location using the high frequency travelling waves measured at a single location on a transmission line," *IEE Seventh International Conference on Developments in Power System Protection*, pp. 403–406, 2001.